Characterization, production and modification of carboxymethylated cellulose fiber films

By Yiwei Jiang

A thesis submitted to McGill University in partial fulfillment of the requirements of

the degree of Doctor of Philosophy

Department of Chemistry

McGill University

Montreal, Quebec

Winter 2025

Abstract

In the last few decades, plastics have become the predominant materials in packaging and membrane applications. However, synthetic polymers present significant environmental challenges, particularly in marine and terrestrial ecosystems. Much effort has been made to replace synthesized polymers with natural ones. Cellulose, present in high abundance, and due to the ease with which it can be multifunctionalized, its biodegradability, and its worldwide availability, is emerging as a promising alternative of plastics, and has attracted much attention worldwide. Many researchers have been working on cellulose-based films for packaging applications. Nonetheless, the strong hydrogen bonding between cellulose chains hinders the dissolution of cellulose, thereby hindering the production of cellulose film.

In this thesis, we modify the hydrophilicity of cellulose by performing a mild carboxylation on pulp, resulting in carboxymethylated cellulose fiber (CMF). Dopes of CMF contain cellulose polymers, hairy cellulose nanocrystals, and salts. We employ acoustics to characterize the components of the dope. We first examine the contribution of salt to the speed of sound. Based on the simplified Wood equation, the speed of sound is proportional to the volume fraction of ions at low concentrations. We introduce the concept of intrinsic sound speed to quantify the contribution of anions and cations. Our findings indicate that anions negatively contribute to the speed of sound, while cations have a positive effect. The contribution of anions is less pronounced than that of cations due to the relatively smaller hydration layers associated with anions. We further analyze the size distribution, speed of sound, and attenuation of CMF, carboxymethyl cellulose (CMC), and crystal nanocellulose (CNC), revealing that salts enhance the speed of sound and lower the acoustic attenuation compared to cellulose.

Previous research in our lab has demonstrated the production of CMF films by dissolving CMF in sodium hydroxide solution, followed by regeneration in an acid bath. Here, we propose a continuous flow casting approach allowing us to regenerate CMF film continuously, which involves the extrusion of cellulose suspension through a narrow slit onto a conveyor belt followed by immersion in a regeneration bath. The speed of the conveyor belt can be adjusted. Our results indicate that the tensile strength of the films is significantly greater in the belt direction (BD) compared to the cross direction (CD), confirming the anisotropic nature of the films, with cellulose chains preferentially aligned along the belt direction. The calculated jet-to-belt velocity decreased with higher speed of a conveyor belt.

In a subsequent study, we aimed to enhance the water resistance of CMF films to replace plastics in food packaging applications. Applying silanization with methyltrichlorosilane and tetraethyl orthosilicate, results in SCMF 1 and SCMF 2 with improved hydrophobicity. The water contact angle confirmed the enhanced hydrophobic properties. The anti-condensation characteristics were evaluated by assessing the freshness of French fries covered with SCMF 1 and SCMF 2. Our findings demonstrate that the fries retained their freshness and crispness for 20 minutes under these films, outperforming both traditional plastic and unmodified CMF films. The silanized CMF films show significant potential for use in the packaging of perishable foods that are sensitive to moisture.

Résumé

Au cours des dernières décennies, les plastiques sont devenus les matériaux prédominants dans les applications d'emballage et de membranes. Cependant, les polymères synthétiques posent d'importants défis environnementaux, notamment dans les écosystèmes marins et terrestres. De nombreux efforts ont été déployés pour remplacer les polymères synthétiques par des polymères naturels. La cellulose, présente en grande abondance, et possédant des caractéristiques de multifonctionnalité, de biodégradabilité et de disponibilité mondiale, émerge comme une alternative prometteuse aux plastiques et a attiré une attention considérable à l'échelle mondiale. De nombreux chercheurs travaillent sur des films à base de cellulose pour des applications d'emballage. Néanmoins, les fortes liaisons hydrogène entre les chaînes de cellulose entravent la dissolution de la cellulose, ce qui limite la production de films à base de cellulose.

Dans cette thèse, nous modifions l'hydrophilicité de la cellulose en effectuant une carboxylation modérée de la pâte, aboutissant à la fibre de cellulose carboxyméthylée (CMF). Les dopes de CMF contiennent des polymères de cellulose, des nanocristaux poilus de cellulose et des sels. Nous utilisons l'acoustique pour caractériser les composants du dope. Nous examinons d'abord la contribution du sel à la vitesse du son. Selon l'équation simplifiée de Wood, la vitesse du son est proportionnelle à la fraction volumique des ions à faibles concentrations. Nous introduisons le concept de vitesse du son intrinsèque pour quantifier la contribution des anions et des cations. Nos résultats montrent que les anions contribuent négativement à la vitesse du son, tandis que les cations ont un effet positif. La contribution des anions est moins prononcée que celle des cations en raison des couches d'hydratation relativement plus petites associées aux anions. Nous analysons ensuite la distribution de taille, la vitesse du son et l'atténuation des CMF, de la cellulose

carboxyméthylée (CMC) et des nanocristaux de cellulose (CNC), révélant que les sels augmentent la vitesse du son et dimunuent l'atténuation acoustique par rapport à la cellulose.

Les recherches précédentes dans notre laboratoire ont démontré la production de films de CMF en dissolvant le CMF dans une solution de soude, suivie d'une régénération dans un bain acide. Ici, nous proposons une approche de coulée en flux continu permettant de régénérer les films de CMF de manière continue, ce qui implique l'extrusion de la suspension de cellulose à travers une fente étroite sur un tapis roulant, suivie d'une immersion dans un bain de régénération. La vitesse du tapis roulant peut être ajustée. Nos résultats indiquent que la résistance à la traction des films est significativement plus grande dans la direction du tapis (BD) par rapport à la direction transversale (CD), confirmant la nature anisotrope des films, les chaînes de cellulose étant préférentiellement alignées dans la direction du tapis. Le rapport vitesse du jet/tapis roulant diminue avec l'augmentation de la vitesse de la bande transporteuse.

Dans une étude ultérieure, nous avons cherché à améliorer la résistance à l'eau des films de CMF pour remplacer les plastiques dans les applications d'emballage alimentaire. En appliquant une silanisation avec du méthyltrichlorosilane et du tétraéthylorthosilicate, nous avons obtenu les films SCMF 1 et SCMF 2 avec une hydrophobicité améliorée. L'angle de contact avec l'eau a confirmé les propriétés hydrophobes accrues. Les caractéristiques anti-condensation ont été évaluées en examinant la fraîcheur des frites recouvertes de SCMF 1 et SCMF 2. Nos résultats montrent que les frites ont conservé leur fraîcheur et leur croquant pendant 20 minutes sous ces films, surpassant à la fois les plastiques traditionnels et les films de CMF non modifiés. Les films de CMF silanisés montrent un potentiel significatif pour être utilisés dans l'emballage des aliments périssables sensibles à l'humidité.

Acknowledgement

I would like to begin by expressing my sincere gratitude to my supervisor, Professor Theo van de Ven, for his exceptional guidance and steadfast support throughout the course of my research. Professor van de Ven's profound expertise in chemistry, combined with his visionary outlook and passion for scientific inquiry, has been a significant influence on my academic and professional growth. His ability to balance deep theoretical knowledge with practical insights has greatly enriched my understanding of the field. Beyond his technical expertise, I have also benefited immensely from his patience, kindness, and generosity in sharing his time. I will always remember our thought-provoking discussions at his office round table, where his insightful perspectives helped me navigate complex scientific challenges. His guidance and influence will continue to motivate and shape my career in the years to come.

I would like to express my sincere gratitude to my research committee members, Professor Ashok Kakkar and Professor Mark Andrews, for their valuable contributions to my work. I deeply appreciate the constructive feedback and insightful suggestions they provided during our review meetings, which significantly enhanced the quality and direction of my research.

I am also thankful to Mrs. Chantal Marotte, Chelsea Briand-Pitts and Rachel D'Ermo for their administrative support and assistance throughout my studies. Their help has been instrumental in ensuring the smooth progression of my work, and I greatly appreciate their kindness and efficiency.

I would like to extend my sincere thanks to the following individuals for their invaluable assistance throughout my research. Dr. Kelly Sears and Dr. David Liu provided essential support in developing my skills in Transmission Electron Microscopy (TEM) and Scanning Electron

Microscopy (SEM). I also wish to thank Mohini Ramkaran, Levin, Kirill, Hatem Titi, Petr Fiurasek, Robin Stein for their training on analysis equipment. I am grateful to Dr. Shang for her assistance with X-ray Photoelectron Spectroscopy (XPS).

I would like to sincerely thank all the members of Professor Theo van de Ven's research group for their encouragement, collaboration, and support throughout my studies. I am particularly grateful to Dr. Nur Alam, Dr. Alvaro Tejado, Dr. Amir Sheikhi, and Mr. Louis Godbout for their invaluable assistance and insightful discussions, which significantly contributed to the development of my research.

The van de Ven lab has been home to many exceptional scientists over the years, each of whom has made a meaningful impact on my research. I would like to particularly acknowledge Mohammadhadi Moradian, who was instrumental in teaching and training me patiently in the use of the experimental tools in the lab. I would also like to extend my heartfelt thanks to Seyed Mohammad Amin Ojagh, Martin Chewe Sichinga, Roya Koshani, Hannah Wiebe, Jane Ebosetale, Md Shahidul Islam, Kayrel Edwards, Sierra Crammer-Smith, and Mandana Tavakolian. Your assistance, research guidance, and thoughtful contributions during group meetings were invaluable. More importantly, your camaraderie and positive attitudes made the van de Ven lab a truly enjoyable and collaborative place to work. I am deeply grateful for all of your support.

I would like to express my deepest gratitude to my mother for her unwavering support and her continued confidence in me, even across the physical distance that separates us.

Finally, I would like to extend a special thank you to my boyfriend, Peiyou. Without his unwavering support and patience, I would not have come this far. His presence has been a constant source of comfort, especially during difficult times. Whenever I faced challenges, he not only

provided emotional support but also offered valuable and insightful advice, despite his expertise being outside my research field. Peiyou's belief in me and his encouragement have helped me to persevere and believe in myself. For all of this, I am profoundly grateful.

List of tables

List of figures

List of schemes

List of abbreviations

AgNPs	silver nanoparticles
AGU	anhydroglucose unit
[Amim][Cl]	1-Allyl-3-methylimidazolium chloride
ANCC	aminated nanocrystalline cellulose
APTES	1-aminopropyltriethoxysilane
ATRP	atom transfer radical polymerization
BC-PPy-ZnO	polypyrrole-Zinc oxide nanocomposite
BD	belt direction
BIBB	2-bromoisobutyryl bromide
BNNSs	boron nitride nanosheets
[C4mim]Cl	1-butyl-3-methylimidazolium chloride
CCF	carboxymethylated cellulose films
CD	cross direction
CED	cupriethylenediamine
CI	crystallinity index
CMC	carboxymethyl cellulose
CMF	carboxymethylated cellulose fiber
CNC	crystal nanocellulose

CVI	colloid vibration current
DCF	diclofenac
DES	Deep eutectic solvents
DI water	deionized water
DMAEMA	2-(dimethylamino) ethyl methacrylate
DMF	dimethylformamide
DMAc	dimethylacetamide (DMAc)
DMSO	dimethyl sulfoxide
DP	degree of polymerization
ENCC	electrosterically stabilized nanocrystalline cellulose
FE-SEM	field emission scanning electron microscopy
FTIR	Fourier transform infrared
GP	graphite powder
HCl	hydrochloric acid
HDPE	high density polyethylene
HPAMAM	hyperbranched polyamide-amine
IC	inclusion complex
LDPE	low density polyethylene
MA	Moisture Absorption
MCA	sodium chloroacetate

MCC	microcrystalline cellulose
MTCS	methyltrichlorosilane
MTMS	methyltrimethoxysilane
NCC	nanocrystalline cellulose
NMMO	N-methylmorpholine-N-oxide
NMR	Nuclear Magnetic Resonance
PA	poly(lactic acid)
PDTS	1H,1H,2H,2H-perfluorooctyltriethoxysilane
PET	Polyethylene terephthalate
PL	beta-propiolactone
PP	polypropylene
PPy	polypyrrole
PS	polystyrene
PSD	particle size distribution
PUA	polyurethane acrylate
PVA	polyvinyl alcohol
PVC	polyvinyl chloride
PVDC	polyvinylidene chloride
Py	pyrrole
RB	rose Bengal

RMS	root mean square
ROS	reactive oxygen species
SEM	Scanning Electron Microscopy
TEM	Transmission Electron Microscopy
TEOS	tetraethylorthosilicate
THF	tetrahydrofuran
WA	Water absorption
WAXD	wide-angle X-ray diffraction
WCA	Water Contact Angle
WVP	Water Vapor Permeation
WVTR	water vapor transmission rate
XPS	X-ray Photoelectron Spectroscopy
XRD	X-ray diffraction
ζ potential	zeta potential

Thesis Outline and Objectives and Author Contribution

This thesis addresses two distinct areas of investigation. The first part systematically examines the influence of cations and anions on the speed of sound in aqueous solutions, introducing the concept of intrinsic sound speed as a quantitative framework for assessing the individual contributions of ions, thereby resolving previously unexplained discrepancies in the literature. This is part of the characterization of the dope (concentrated alkaline cellulose solution) from which cellulose-based films are extruded. The second part focuses on the continuous production of cellulose-based films from the cellulose dope, using a flow-casting method and investigating the enhancement of their water resistance and anti-condensation properties through silanization. This work demonstrates the potential of these modified cellulose films as sustainable alternatives to conventional petroleum-based plastics, with particular relevance to food packaging applications.

Chapter 2 introduces the concept of intrinsic sound speed to quantify the contributions of individual ions to the speed of sound in aqueous solutions, revealing that cations increase, and anions decrease the sound speed, with hydration layers playing a crucial role. The proposed method provides a quantitative framework that explains previously unexplained data and is applicable to various systems containing low concentrations of ions, molecules, or particles.

Chapter 3 presents a method for the continuous production of robust and flexible cellulose-based films using a flow-casting technique, which enhances their mechanical properties by aligning cellulose crystals at higher extrusion speeds. The films exhibit increased tensile strength and anisotropic behavior, but their inherent hydrophilicity poses a challenge for widespread application, which is addressed through silanization to improve water resistance and enhance their potential as eco-friendly alternatives to petroleum-based plastics in food packaging.

Chapter 4 explores the enhancement of water resistance in carboxymethylated cellulose fiber (CMF) films through silanization with methyltrichlorosilane (SCMF1) and tetraethylorthosilicate (SCMF2), achieving significant improvements in hydrophobicity, as confirmed by Fourier-transform infrared spectroscopy, X-ray photoelectron spectroscopy, and nuclear magnetic resonance. The modified films, with increased porosity and superior anti-condensation properties, demonstrated extended freshness and crispness for French fries compared to polyethylene, highlighting their potential as eco-friendly alternatives in both food and non-food packaging applications.

Author contributions

This is a manuscript-based thesis and consists of the following 3 manuscripts: two of which published, and one of which was submitted in June 2024 (and for which publication is delayed, as the reviewers requested additional experiments)

Chapter 2: Yiwei Jiang conducted all laboratory work, data analysis, and wrote the manuscript. Dr. Theo G. M. van de Ven supervised the project and contributed to the manuscript editing.

Jiang, Y., & van de Ven, T. G. M. (2024). Cations and anions affect the speed of sound in water oppositely. *The Journal of Physical Chemistry Letters*, *15*(15), 4125-4129.

Chapter 3: Yiwei Jiang conducted all laboratory data analysis, wrote the manuscript, and supervised Oana Nutu during her undergraduate research. Seyed Mohammad Amin Ojagh performed some of the experiments, while Mohammadhadi Moradian designed the conveyor belt.

Both Mohammadhadi Moradian and Theo G. M. van de Ven provided project supervision and contributed to manuscript editing.

Jiang, Y., Moradian, M., Nutu, O. M., Ojagh, S. M. A., & van de Ven, T. G. M. (2024). Continuous Production of Resolidified Cellulose-Based Films. *Industrial & Engineering Chemistry Research* 63(45), 19537-19545, (2024).

Chapter 4: Yiwei Jiang conducted all experimental work and wrote the manuscript. The experiments, data analysis, and manuscript writing were carried out under the supervision and guidance of Dr. Mohammadhadi Moradian and Dr. Theo van de Ven. This work is submitted under the title:“ Hydrophobization and anti-condensation of cellulose-based films by silanization” and is under review by the *International Journal of Biological Macromolecules*.

Table of Contents

Chapter 1. Introduction

1. 1 Cellulose

Cellulose is one of the most plentiful natural polymers, with an estimated global production of approximately 1.5×10^{12} tons per year, making it a virtually inexhaustible raw material [1, 2]. Cellulose was first described by the French chemist Amselme Payen, when he discovered a resilient fibrous material that remained from the treatment of the plant fibers with acids and ammonia [3]. The molecular formula ($C_6H_{10}O_5$) was subsequently established, and the term "cellulose" was officially introduced by the French Academy in 1839 [4]. Cellulose comprises repetitive units of β-D-glucose monomers, and constitutes most of the cell wall structure typical of most plants, some animals, and bacteria [2]. Due to its abundance, renewability, and widespread availability, there have been many recent efforts to use cellulose as a sustainable alternative to conventional plastics.

Cellulose is abundantly found in nature, primarily in plant materials such as wood (40-50 wt%), cotton (90 wt%), hemp (75-80 wt%), and flax (70-80 wt%) [5]. Other sources include some fungi and algae. Cellulose constitutes about 40% of the carbon content in plants and is one of the important components contributing to the structural framework of plant cell walls, giving them strength and rigidity.

Figure 1. 1 is a schematic representation of cellulose structure and its topography within the cel [6, 7]. Cellulose is a polymeric compound showing a very complex three-dimensional hierarchical structure, being one of the main components of a plant cell wall. The cell wall can be separated into two structural units: a primary and a secondary wall. In mature cells, the secondary wall is

deposited on the primary wall's inner surface. Typically, it comprises three distinct layers: a thin outer layer (S1), a thick middle layer (S2), and a thin inner, helically wound layer (S3).

Within these layers, cellulose is arranged in coaxial microfibrils. Each microfibril is made from long cellulose polymer chains stacked with a high degree of order, giving rise to alternating crystalline and amorphous regions [6]. The microfibrils pack together in an ordered state, due to hydrogen bonding and van der Waals forces between adjacent microfibrils, as described in Figure 1. 1 [6, 7].

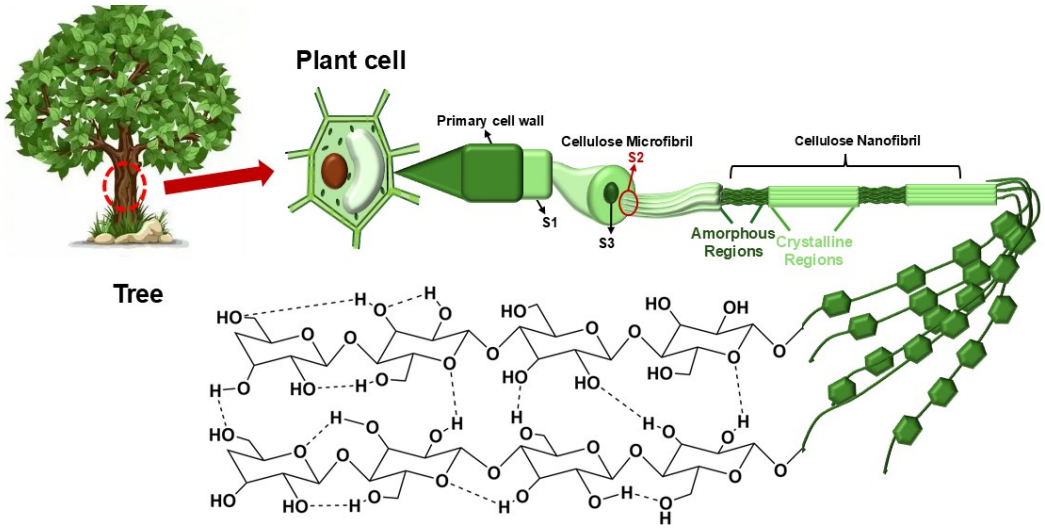

Figure 1. 1 Hierarchical structure of cellulose from plant

Cellulose, regardless of its source, is made of D-glucopyranose ring units arranged in the $^{4}C_{1}$-chair conformation, which is the most energetically stable configuration [8]. These units are linked by β-1,4-glycosidic bonds which impose a 180° rotation in the position of the chain axis compared to the previous unit for sterically stable packing of the chains [9]. Each anhydroglucose unit (AGU) in the cellulose chain carries three hydroxyl groups positioned at C2, C3 and C6. The repeating

unit of cellulose is cellobiose, which measures approximately 1.3 nm in length [10]. The cellulose chain has two distinct ends: one is the non-reducing end, where an anomeric carbon is linked via glycosidic bonds, and the other is the reducing end group with an aldehyde-like D-glucopyranose [7].

The crystalline regions give the cellulose materials high strength and stiffness. The cellulosic chains' degree of polymerization varies widely, with literature values ranging from 10,000 to 15,000 AGUs due to the variability in the source. The crystallinity of cellulose usually lies between 40%-70% [7]. Figure 1. 1 illustrates the crystalline and amorphous regions of cellulose [6, 7]. The amorphous region is formed because of breakage and disorder of hydrogen bonds which differs extensively in different sources of the cellulose chain. The characteristic of cellulose significantly varies because of the different ratios of amorphous and crystalline regions [6, 7]. Specifically, the crystalline regions are denser and more resistant to physical and chemical modifications compared to the amorphous regions [7]. This is also the reason why amorphous regions of cellulose are preferentially modified. [6].

1. 2 Acoustics

Acoustic and electroacoustic spectroscopy are rapidly advancing techniques for characterizing concentrated colloidal systems and provide clear advantages over more conventional techniques like light scattering. Although both techniques are based on well-established scientific principles, they differ in the parameters they measure and the complexity of their respective applications [11].

Acoustic spectroscopy measures sound attenuation of ultrasound in colloidal dispersions as a function of wavelength, from which the particle size distribution (PSD) can be deduced. The speed of sound in a dispersion provides information about what type of material is present in the dispersion [12]. The theory for sound scattering by atmospheric disturbances was first established by Poisson in the 1820s [13]. Other subsequent, major contributions were made by Pellam and Galt [14], Sewell [15], and Epstein and Carhart [16]. Despite its historical relevance and wide-ranging applications [17], the role acoustics play in colloid science has received very little attention. Indeed, the primary advantage acoustics has over light scattering is that it is able to characterize concentrated systems without dilution [18]. Acoustic methods can measure particle sizes in systems with volume fractions up to 40%, but are also applicable in cases where dispersed phase concentrations are low, about 0.1% [18].

One of the major strengths of acoustic spectroscopy is its ability to provide particle size distributions on a weight basis, which is particularly useful for polydisperse systems. Unlike light scattering, which is disproportionately sensitive to large particles and can thus overestimate their size, acoustic methods offer a more reliable representation of particle size distributions. For instance, aggregation phenomena can shift the particle size distribution by replacing smaller particles with larger aggregates, and acoustic spectroscopy can monitor these changes in real-time. Such measurements, previously challenging to perform, have been significantly enhanced by ultrasound-based spectroscopy, which enables the characterization of particle size without disrupting the system.

The ultrasound pulse also perturbs the double layer of the particle, giving rise to an electric current, the colloid vibration current (CVI). An electroacoustic probe measures the CVI from which the zeta potential (ζ potential) of the suspended particles can be determined, which is an indication of

the dispersion's stability. Unlike other techniques, acoustic spectroscopy does not require calibration with a known colloid and, thus, is an absolute measurement technique [18]. Furthermore, it can offer insights into the microstructure of the dispersion, functioning similar as a micro-rheometer by applying stresses at the micron scale, further enhancing its utility in characterizing concentrated colloidal systems.

Figure 1. 2 outlines the fundamental principles of the acoustic measurement technique employed in this study. First, an electrical signal is transformed into an ultrasound pulse of a given frequency (1-100 MHz) and intensity using a piezoelectric transducer. Subsequently, the pulse is sent into the sample, as shown in Figure 1.2. While propagating through the medium, the pulse undergoes a decrease in intensity due to absorption and scattering by particles within the sample. A second piezoelectric transducer detects the attenuated acoustic pulse and reconverts it into an electrical signal. This signal carries information on energy loss and transmission time for each frequency. The data are generally represented by an attenuation coefficient, α, defined as follows:
[19]:

$$\alpha = \frac{10}{f \times L} log \frac{I_{in}}{I_{out}}$$

Where: f: frequency of the ultrasound pulse (MHz)

L: the distance between the transmitter and receiver (cm)

I_{in}: the intensities of the emitted (I_{in}) and received (I_{out}) pulses,

I_{out}: the intensities of received pulses

The system also records the time delay, which is the duration it takes for the pulse to travel from the transmitter to the receiver. Using this time delay, the speed of sound (c) can be calculated using the equation: c = L/t.

Morse and Uno Ingard have derived an expression for the attenuation due to scattering α_{sc} (in neper/cm) [20] valid in the Rayleigh long wavelength limit [21] (valid when diameters of particles are less than 1/6 of the wavelength)

$$\alpha_{sc} = \frac{\varphi\omega^4 a^3}{2c_m^4}\left[\frac{1}{3}\left(1 - \frac{\rho_m c_m^2}{\rho_p c_p^2}\right)^2 + \left(\frac{\rho_p - \rho_m}{2\rho_p + \rho_m}\right)^2\right.$$

Where ρ: density

φ: volume fraction

a: radius

ω: angular frequency of the ultrasound with $\omega = 2\pi f$

c: the speed of sound

The index m and p refer to the liquid medium and particles, respectively.

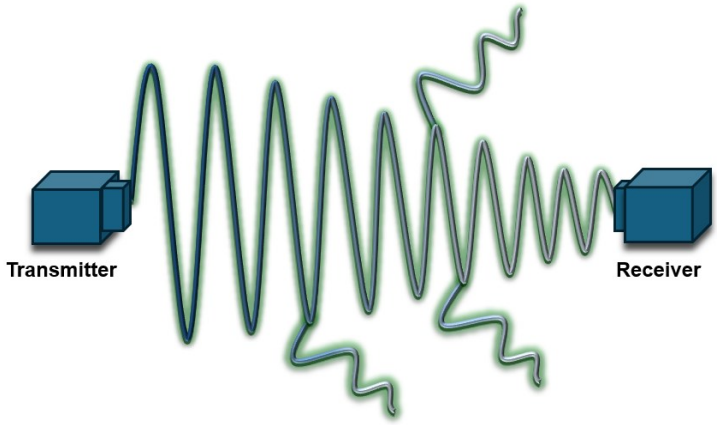

Figure 1. 2 Fundamental principles of acoustic measurement

For suspensions of particles, the theory of ultrasound propagation through heterogeneous systems, developed by numerous researchers in the 20th century, can be applied [22]. According to Wood's theory [23], the speed of sound in such systems is given by the following equation :

$$\frac{c_m^2}{c_s^2} = \frac{\rho_s}{\rho_m}(1 - \varphi + \varphi\frac{\rho_m c_m^2}{\rho_p c_p^2})$$

where

ρ_s: the density of the colloid.

φ: volume fraction

The index s refers to the solution as a whole.

For low volume fraction, this equation simplifies to:

$$\frac{c_s}{c_m} = 1 + (1 - \frac{\rho_p^2 + (\frac{c_m^2}{c_p^2})\rho_m^2}{2\rho_m\rho_p})\varphi$$

This equation shows that at low volume fractions, the overall suspension sound velocity is linearly dependent on the volume fraction. The slope is given by the densities and sound velocity of the particles and the medium and can be either positive or negative.

The concept of the electroacoustic effects was initially introduced by Debye [24], while its application to colloidal systems was proposed a few years later by Hermans [25]. After that, Frenkel developed the first electroacoustic theory of seismoelectric phenomena [26]. Electroacoustics, which applies an electric field for interaction with dispersed particles, is more complicated and can simultaneously measure particle sizes and zeta potentials [18]. While this technique offers valuable information on electrokinetic properties of colloidal systems, it is generally less effective than acoustic spectroscopy for precise particle size determination [27]. On the other hand, electroacoustics is highly suitable for measuring the zeta potential of particles, one of the most important characteristics that allows for explaining the interaction between particles and the stability of colloidal systems.

A multitude of studies have discussed the application of the acoustic and electroacoustic methods for the characterization of many materials. For instance, intravenous fat emulsions have been characterized for particle size and zeta potential [28]. Dukhin et al [19] employed sound speed, attenuation, and electrical charge measurements to characterize proteins and blood cells. Safiri et al [29] employed electrokinetic-sonic-amplitude and acoustic attenuation measurements in the study of NCC and ENCC. Their results are reported to show the colloidal stability of ENCC, whereby it was discussed how changes in pH and ionic strength influence mobility, zeta potential, and the size of the particles. Koshani's study [30] considered longitudinal viscosity and sound velocity for demonstrating the potential for controlling particle size and electrostatic charge.

Moreover, acoustic spectroscopy has also been applied to the size distribution analysis of cellulose nanocrystals [31].

Ultrasound-based techniques provide significant advantages over traditional light-based methods, especially concerning concentrated, opaque dispersions, as they do not require sample dilution. Thus, the potential of this technique is that it does not disturb aggregates and allows more accurate measurements of particle size and zeta potential. Furthermore, these methods are highly robust, precise, and fast; therefore, they allow online characterization and, in particular, real-time monitoring of dynamic systems. The acoustic and electroacoustic methods applied to cellulose-based materials give reliable assessments of such significant properties as particle size distribution, viscosity, and zeta potential; thus, they present important information on current problems encountered in modern nanocellulose technologies. In this respect, these techniques are particularly useful for advancing the understanding of nanocellulose behavior in fields such as water remediation [32] and drug delivery [33], for which particle properties optimization and performance prediction are critical.

1. 3 Cellulose dissolution

For cellulose to be used practically, dissolution is a prerequisite. Due to strong intermolecular and intramolecular hydrogen bonding attributed to the large number of hydroxyl groups along the cellulose polymeric chains, a well-built cellulose fiber is thus insoluble in most common laboratory solvents, including water, dimethylformamide, tetrahydrofuran, and dimethyl sulfoxide [34][35]. Consequently, the traditional viscose process, a multistep and ecologically destructive process, has long held a leading place in the regenerated cellulose industry. In this regard, special solvents that

can complex with the hydrogen bond-forming groups will be discussed. These include solvents such as dimethylacetamide (DMAc) / LiCl, NaOH/urea aqueous solutions, N-methylmorpholine-N-oxide (NMMO) / water, ionic liquids, cupriethylenediamine (CED), tetrabutylammonium fluoride / DMSO, and metal-complex solutions [34]. High polarity solvents prove to be more efficient since they form hydrogen bonds with the cellulose and break its crystalline structure [34].

A significant breakthrough in cellulose dissolution occurred in 2002 when Swatloski et al. [36] proved that the ionic liquid 1-butyl-3-methylimidazolium chloride ([C4mim]Cl) could dissolve cellulose. Since then, ionic liquids have increasingly been used in the dissolution and modification of cellulose-based products.

Ionic liquids are a class of salts remaining liquid at relatively low temperatures and have become one of the most appealing solvents for cellulose fibers [37]. Ionic liquids consist of such cations as imidazolium, N-alkyl pyridine cation, and alkyl quaternary ammonium cation; their anions are, among others, chloride and tetrafluoroborate. The ionic liquids consist of large, asymmetric ions that are characterized by several noticeable advantages, such as low volatility, high ionic conductivity, and tunable properties. The efficient dissolving process relies mainly on the interaction between the ionic liquids with the hydroxyl groups of cellulose, disrupting the hydrogen bond networks within the cellulose crystalline structure. When ionic liquids are combined with cellulose fibers, the cation-anion pairs of the ionic liquid operate as electron donor-acceptor systems. This interaction allows the ions of the ionic liquid to interact with the cellulose molecule's O and H atoms, thereby disrupting the hydrogen bonds that hold the cellulose structure together. (Figure 1. 3). New hydrogen bonds are formed between the ions of the ionic liquid and the cellulose chains, further promoting the cellulose dissolution process and subsequent processing. [39].

Sodium hydroxide (NaOH) solution was found to be capable of dissolving cellulose fibers with a low degree of polymerization (DP < 250) at low temperatures [40]. Recently, adding urea to a NaOH solution resulted in a NaOH/urea/water system in a striking improvement in the solvent's capability of dissolving cellulosic fibers [40].

The proposed mechanism for cellulose dissolution in such a NaOH/urea aqueous solution, analogous to that described for ionic liquids, involves the breaking of the hydrogen bonding network within the cellulosic fibers via NaOH and urea. The resultant peeling away of the cellulose chains from the fiber network culminates in the dissolution of cellulose [41]. Notably, the urea hydrates form an inclusion complex (IC) with the released cellulose chains, preventing their reaggregation upon dissolution. The formation of such an inclusion complex has been confirmed through various techniques including transmission electron microscopy (TEM) and wide-angle X-ray diffraction (WAXD) [42]. Recent studies have demonstrated rapid cellulose dissolution in NaOH/urea aqueous solutions. For instance, Cai et al [43] achieved complete dissolution within 2 minutes at a pre-cooling temperature of -10°C. Kong et al [44] showed that 80% dissolving of bleached softwood sulfite dissolving pulp was achieved in an 8% NaOH/8% urea/6.5% thiourea solution. These results collectively testify to the capability of the NaOH/urea-based systems for dissolving cellulose and prove to be a suitable alternative route for processing cellulose-based materials.

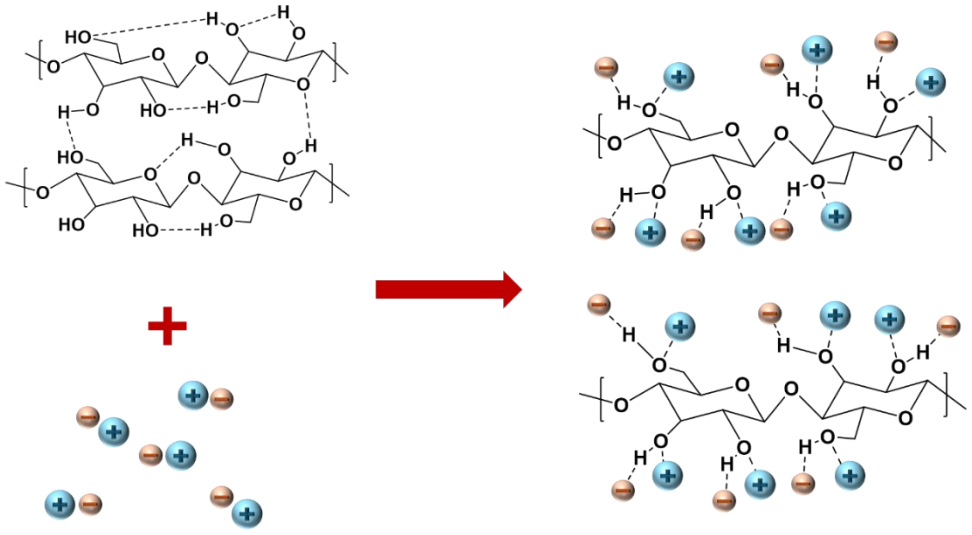

Figure 1. 3 Dissolution mechanism of cellulose in ionic liquids (+ and - represent the cation and anion of ionic liquids)

N-methylmorpholine-N-oxide has proven to be an excellent solvent for cellulose. The N–O bond in NMMO is considered energy-rich, meaning it can be easily cleaved, releasing a significant amount of energy (222 kJ/mol) upon bond rupture [46]. Therefore, it is the reason why NMMO is a strong oxidizing agent, thermally unstable, and easily cleavable. [46]. The strong polarity of the N-O bond helps NMMO to opportunistically form hydrogen bonds with the principal hydroxyl (H-O) groups of the cellulose molecules, ultimately resulting in good solubility of cellulose in the NMMO solvent system.

To be more specific, the dissolution mechanism of cellulose has been presented in Figure 1. 4 [34]. The inter and intra-hydrogen bonds on the cellulose chain prevent cellulose from being dissolved in water [34]. However, the oxygen and nitrogen on NMMO act as electron donors and acceptors, respectively, thereby interacting with the hydrogen and oxygen on cellulose, aiding the dissolution process. Indeed, this interaction promotes the formation of hydrogen bonding between NMMO

and cellulose [34]. In a study by Dogan et al [47], the conventional heating method for dissolving cellulose in an NMMO aqueous solution was replaced by microwave heating at 210 W. This alternative form of heating provides another alternative for high-efficiency cellulose processing with NMMO.

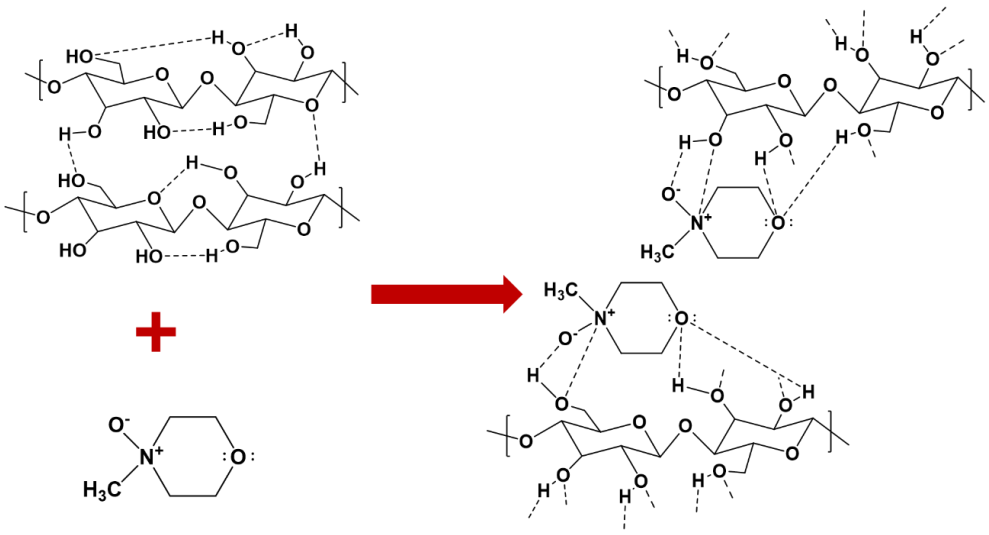

Figure 1. 4 Dissolution mechanism of cellulose with NMMO

Recent studies on cellulose solubility reveal that although cellulose can be dissolved in many solvents, several important limitations exist. For instance, the dissolution of cellulose in ionic liquids typically requires high temperatures, and the process often takes several hours or even days [48]. More importantly, many of these solvents degrade cellulose, causing aggregation and the production of cellulose with surprisingly low molecular weight [49-52]. In other words, the dissolution process damages the integrity of the cellulose structure.

1. 4 Cellulose derivatives

Cellulose is a highly versatile biopolymer, which arises from its unique structure that allows for a wide range of chemical modifications to tailor its properties for specific applications. Long-chain cellulose esters such as cellulose acetate butyrate and cellulose acetate are known to possess water resistance properties and are synthesized from acetic acid or fatty acids [53]. However, for many practical purposes, such as making cellulose films, dissolution in cellulose always comes first. While conventional solvents may be used to dissolve and then regenerate cellulose, enormous interest has also focused on its chemical modification to improve its properties, for example, enhanced hydrophilicity. Cellulose derivatives have been made, such as cellulose carbamate, a hydrophilic derivative, and cellulose xanthate, a cellulose derivative soluble in alkali, to obtain desirable properties in cellulose films. These modified cellulose films possess excellent potential in various applications, including packaging, where biodegradability and functionality are essential [54].

Chemical modification by carboxylation and carboxymethylation, introduces hydrophilic functional groups into cellulose and subsequently enhances its dissolution. Carboxymethyl cellulose, an anionic, water-soluble cellulose derivative, is formed by substituting some −OH groups in the cellulose backbone with carboxymethyl groups (−CH_2COOH), which enhances the anionic character to the polymer. This modification greatly increases the solubility of CMC in water and changes its chemical characteristics, making it suitable for a wide range of applications in different sectors.

Due to its unique surface, mechanical properties, tunable hydrophilicity, and rheological behavior, CMC has been thoroughly investigated. The renewable raw materials for its production, low-cost

synthesis, and wide range of functional applications link CMC with many fields, e.g., food [55, 56], textiles [57], pharmaceuticals [58], biomedical engineering [59], wastewater treatment [60], and energy storage [61]. Extensive research has been conducted on the synthesis, modification, and application of CMC, with particular emphasis on its diverse uses in industrial processes.

Carboxymethylated Cellulose Fiber (CMF) and Carboxymethyl Cellulose (CMC) are both derivatives of cellulose, although they look entirely different concerning their degrees of substitution, solubility, and structure. The CMF has a lower degree of substitution of about 0.1 to 0.3, thus representing a poorly soluble, fiber-like material. On the other side, the DS of CMC is much higher, typically about 0.4 to 1.5, solubilizing this compound such that it could be used wherever gels or thickening is needed [2]. CMF undergoes a mild carboxymethylation process that replaces some hydroxyl groups in the fiber (mainly at position C-2) with carboxyl groups without significantly altering the fiber's overall structure [62]. Contrarily, CMC undergoes an intense carboxylation process, resulting in a much higher substitution level; thus, it is completely soluble. The charge density of CMF may be adjusted depending on the sodium chloroacetate amount used during synthesis [2, 31].

Measurements of acoustic spectroscopy on alkaline CMF dope solutions show that, with a charge density of 2.5 mmol/g and DS = 0.42, CMF can be made into a dope with particles in the size range of 18-208 nm. The dope made from a CMF with a charge density of 1.3 mmol/g shows a PSD in the range of 27-163 nm. The zeta potential for these samples was measured at -5.1 mV for 1.3 mmol/g of carboxyl group density and -17.5 mV for 2.5 mmol/g charge density [31].

Another highly charged cellulose derivative, electrostatically stabilized nanocrystalline cellulose (ENCC), a nanocellulose typical with a density of carboxyl groups of up to 6.6 mmol/g, can be

obtained via a combined periodate and chlorite oxidation process, which also breaks cellulose chains in the amorphous cellulose regions as a site reaction, causing the cellulose fibers to fall apart in nanocellulose particles. [63]. This highly charged cellulose increases the chances of developing modified cellulose for various applications, even in cases where the material needs to exhibit strong features owing to high electrostatic interaction.

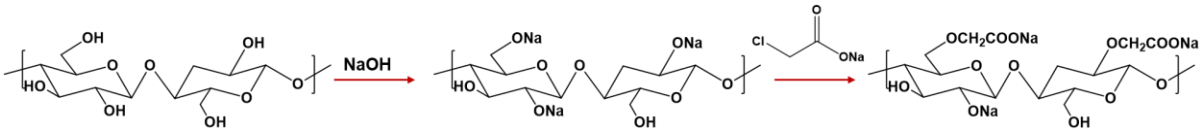

Scheme 1. 1 Synthesis of CMF

Therefore, CMF and other derivatives of modified cellulose may be seen as versatile, water-soluble alternatives toward the realization of films that are to be endowed with specific mechanical, hydrophilic, and functional properties. The fields of application are many and varied; attention is drawn here to the most important areas of packaging, where such films are used as biodegradable and environmentally friendly food packaging alternatives.

1. 5 Cellulose based film

Cellulose films, derived from cellulose, have several advantages which make them genuinely promising for a large number of applications. Apart from being biodegradable, flexible, and multifunctional, they possess no apparent health or environmental impacts. Such characteristics have placed cellulose films in great demand across many applications, including food packaging, waterproofing, drug delivery systems, and cosmetics, to name a few. Besides, cellulose films possess comparatively low thermal expansion and excellent mechanical properties which have garnered significant global attention for their potential applications in various industries [64].

Cellulose acetate membranes have attracted the attention of researchers worldwide due to their relative hydrophilicity, low toxicity, and biodegradability. Cellulose acetate films take an important role in different fields, including filtration, wastewater treatment and medical devices [65].

One of the most commercially available cellulose-based films is cellophane, which is manufactured by a multi-step process involving steeping, aging, xanthation, and regeneration [66]. Cellulose is first treated with sodium hydroxide, creating alkali cellulose, which is then aged to the desired degree of polymerization [67]. The alkali cellulose is then reacted with carbon disulfide (CS_2) at low temperature and pressure to form the intermediate compound, cellulose xanthate. This xanthate is then dissolved in a dilute sodium hydroxide solution to create a viscous solution, referred to as viscose dope. The dope is allowed to ripen so that the xanthate groups distribute evenly within the cellulose matrix [68]. Following this, the solution is filtered and deaerated to remove impurities.

The viscose dope is then extruded through a slit into a coagulation bath containing sulfuric acid and sodium sulfate. Regeneration of the cellulose occurs in the bath, yielding a transparent, flexible film. The regenerated film is subsequently washed, desulfurized, bleached, and dried for final processing [67]. Similarly, the viscose solution can be extruded through small holes in a spinneret into a coagulation bath to generate rayon fibers [69].

Unlike rayon, which retains an amorphous structure, cellophane has regions of crystalline and is highly transparent, with low air permeability and resistance to moisture. Thus, it finds particular application in packaging and moisture barrier films [70, 71].

Other ways to obtain cellulose films are spin coating [72], and Langmuir-Blodgett deposition and regeneration. Spin coating, as illustrated in Figure 1.5a, consists of dropping a polymer solution

onto a spinning plate. The centrifugal force of the high-speed rotation evenly distributes the solution across the surface while simultaneously accelerating the evaporation of the solvent. A thin film is obtained upon drying. This method is straightforward and easily reproducible [72]. The Langmuir-Blodgett method [73] is based on depositing a polymer solution onto an immiscible liquid, in which it spreads rapidly. Upon evaporation, a monolayer of polymer film is formed at the liquid surface. The substrate can then be raised or immersed into the monolayer, transferring the film onto the substrate, depending on the hydrophobicity of the polymer (as shown in Figure 1. 5b). This process can be repeated to build up multilayered films.

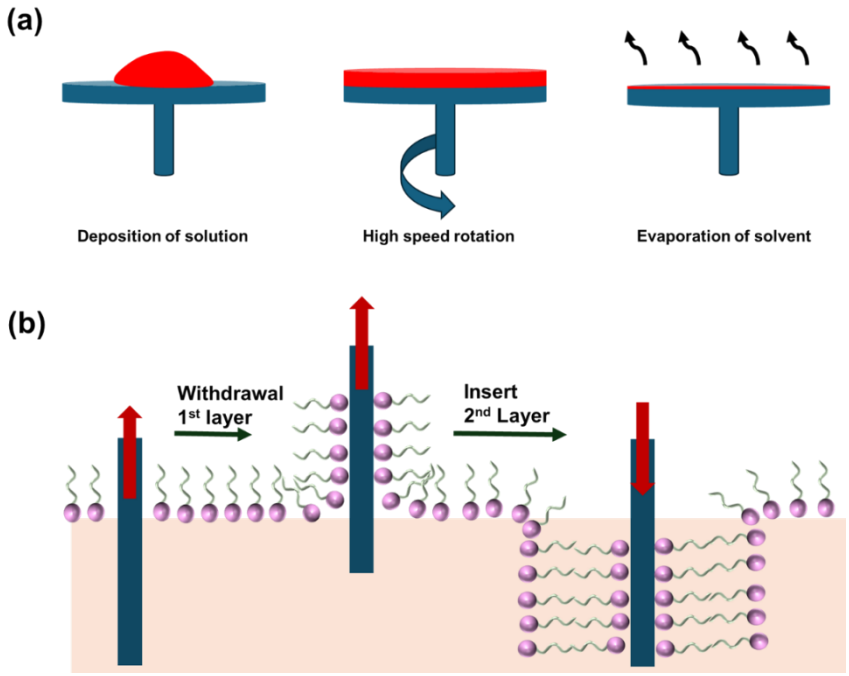

Figure 1. 5 Spin-coating processes of films; Schematic of the Langmuir-Blodgett (LB) technique.

Another commonly used method in the preparation of cellulose films is dissolution and resolidification, where cellulose fiber is dissolved in a suitable solvent, followed by the

regeneration of cellulose from the solution [62]. An example is the preparation of regenerated cellulose films from CMF, as demonstrated by Moradian et al. [2, 62]. In this method, CMF is first dissolved in deionized (DI) water, followed by the addition of sodium hydroxide to enhance solubility. The resulting dopes are degassed by centrifugation at 1000 rpm for 5 minutes to remove any trapped air. The degassed dope is then cast onto a Teflon mold and immersed in a 10% sulfuric acid bath to regenerate the cellulose. Once the film has solidified, it is washed with tap water and air-dried on a glass plate. They prepared transparent CMF films with varying mechanical properties by adding sodium chloroacetate at various concentrations. The authors observed that films with a higher charge density of carboxyl groups exhibited improved resilience, transparency, and enhanced hydrophilicity [3]. Moreover, the CMF films exhibited remarkable stability under hot air conditions and can be readily recycled, hence constituting potential sustainable alternatives for food packaging. Ultrathin and ultra-strong films were prepared by combining CMF with epichlorohydrin [74]. The modified CMF films had a thickness of about 1 μm, and their tensile strength and Young's modulus were 299 MPa and 12.7 GPa, respectively; thus, they could outperform other cellulose-based films in terms of mechanical properties.

Currently, cellulose-based films are gaining widespread attention for their environmental sustainability, versatility, and superior material properties. The various methods used to produce cellulose films, including the traditional viscose process, spin coating, Langmuir-Blodgett deposition, and regeneration of carboxymethylated cellulose, provide multiple avenues for optimizing film characteristics to specific needs in packaging, medical, and cosmetic applications.

1. 6 Application of cellulose based film

Facile and environmentally friendly methods have been developed for the production of cellulose films. Due to their excellent mechanical properties, high transparency, flexibility, biodegradability, and thermal stability, regenerated cellulose films have attracted great attention in the development of novel materials for many areas, especially food packaging. Further modification of the functional groups in cellulose, in turn, opened up the development of specific functional properties, such as increased mechanical strength, oxygen and water vapor permeability, electrical conductivity, and hydrophilicity, which are significant for such areas as drug delivery, electronics, and other highly technological applications.

Packaging protects products from contaminants and is an essential part of every human's life. In the case of food packaging, materials must not only provide protection but also be green, flexible, and waterproof. The food-grade packaging can be either rigid or flexible, depending on the contents. Conventional petroleum-based plastic materials are highly detrimental to the environment [75], driving the need for alternative, sustainable materials. Recently, much attention has been paid to the preparation of cellulose-based packaging materials with a wide range of characteristics.

For example, Gu et al. [76] developed an antibacterial cellulose film containing silver nanoparticles (AgNPs) and cotton fibers using a hyperbranched polyamide-amine template, reducing agent, and stabilizer. Cotton fibers were first dissolved in a hydroxide/urea solution, followed by oxidation of hydroxyl groups at the C-2 and C-3 positions to aldehyde groups using sodium periodate ($NaIO_4$). Then, hyperbranched PAMAM was anchored to the oxidized cellulose by the reaction of the aldehyde and amino groups. AgNPs-embedded cellulose films were obtained

by recasting the cellulose solution into ethanol for regeneration. The resultant film showed antibacterial activity, thus making it suitable for food packaging.

In another study, Koshani et al. [77] developed an antibacterial film based on aminated nanocrystalline cellulose (ANCC). To synthesize ANCC, cellulose underwent oxidation, amination, and reduction, and was subsequently conjugated with rose Bengal (RB), a photosensitizer that generates reactive oxygen species (ROS) to damage bacterial cells. Successful conjugation of RB and ANCC was confirmed using FTIR and solid-state 13C CP/MAS NMR spectroscopy. The antibacterial testing showed that the ANCC-RB film possessed good antibacterial properties under UV light, especially on foodborne bacteria like *Listeria monocytogenes*.

Additionally, an active and intelligent cellulose-polypyrrole-ZnO film was developed by modifying bacterial cellulose (BC) with a polypyrrole-Zinc oxide nanocomposite (BC-PPy-ZnO) [78]. Metal-oxide compounds like ZnO are known for their antibacterial properties due to hydrogen peroxide production, which occurs through a photocatalytic process where UV light excites electrons, creating electron-hole pairs that reduce oxygen to form superoxide radicals, which then react to produce H_2O_2. On the other hand, polypyrrole is a conductive material commonly used in food packaging. The film's electrical resistance changes were correlated with microbial growth, sensory properties, and pH changes in chicken thigh meat, enabling the estimation of food spoilage and expiration time. This intelligent film offers the potential to monitor food quality in real-time, improving the safety and shelf life of food products.

Sim et al [79]. developed a transparent composite film by combining carboxymethylated fibers (CMF) with carboxymethyl cellulose (CMC), where CMC serves as a strength enhancer. The

mechanical properties of the composite film are comparable to those of commercial tracing papers. Water absorbency, transparency, and oxygen-barrier properties of the film improve with increased degrees of substitution DSC, which have considerable potential for application in wound dressing.

Moradian et al.'s study [2] demonstrated that the transparency and hydrophilicity of cellulose films could be improved by increasing the substitution of hydroxyl groups with carboxyl groups. Carboxyl groups, being highly hydrophilic, were introduced to modify the water absorption properties of the cellulose films. It was found that with an increasing amount of carboxyl groups from 0.8 to 2.5 mmol/g, the films' moisture absorption increased. The tensile modulus of the films was at its optimum at a CMF film charge of 1.5 mmol/g, indicating an improvement in the flexibility and resilience of the CMF films. The films had a water vapor permeability in the range of 130 to 166 g/m²·day, implying that the films have poor moisture barrier compared to the high-barrier films. For example, polyethylene has a water vapor permeability below 5 g/m²·day [80]. This is probably because the CMF films contain high water affinity; the films are unsuitable for food packaging purposes and need modification for moisture resistance.

One approach to modifying the hydrophilicity of cellulose films is through surface treatments that increase their hydrophobicity. Li et al. [81] achieved that by soaking a cellulose matrix in polyurethane acrylate (PUA) prepolymers through dip-coating; thus, the water repellence of the films was improved. Their process started with dissolving natural cellulose in a LiOH/NaOH solution, which was then precipitated in ethanol. A double-network system of cellulose and PUA was obtained by polymerizing the urethane acrylate in the cellulose solution. Scanning electron microscopy (SEM) showed the porous structure of the cellulose hydrogels before adding the urethane acrylate monomer. After polymerization, the smooth surface revealed by SEM indicated that the PUA filled the pores. FTIR showed the completion of the PUA polymerization. Water

contact angle measurements showed the enhanced hydrophobicity of the modified cellulose films: for example, the contact angle of the modified cellulose film remained almost unchanged for about two minutes, while pure cellulose films showed a very rapid decrease in contact angle.

Cellulose films are also being applied in medical applications. Maver et al. [82] prepared ultrathin cellulose films for the purpose of controlled drug delivery, specifically for use in wound dressings. Diclofenac (DCF), a well-known analgesic, served as a model drug. DCF-loaded cellulose films were prepared by mixing trimethylsilyl cellulose solutions containing DCF followed by spin coating. In vitro release studies were conducted on the films using UV-Vis spectroscopy. The release rate could be controlled by adding additional layers of cellulose without DCF, which slowed the release significantly. This allowed for the gradual release of the drug, preventing rapid spikes in drug concentration in the bloodstream.

Another study focused on improving the biocompatibility of cellulose membranes by grafting zwitterionic materials like sulfobetaine and carboxybetaine, which are known for their good blood compatibility and antifouling properties [83]. Carboxybetaine brushes were grafted onto cellulose via atom transfer radical polymerization (ATRP) to further enhance the blood compatibility of cellulose films. Specifically, 2-bromoisobutyryl bromide (BIBB) was first immobilized onto the surface of cellulose membrane via esterification. This step was followed by ARGET-ATRP polymerization of 2-(dimethylamino) ethyl methacrylate (DMAEMA The resultant polymer then reacted with cellulose via a ring-opening reaction with beta-propiolactone (PL) to give polycarboxybetaine. Various tests, including platelet adhesion, hemolysis, and plasma protein adsorption, demonstrated that the grafted cellulose membrane exhibited improved resistance to nonspecific protein adsorption and platelet adhesion, as well as a reduced hemolysis rate,

compared to pure cellulose. This functionalized cellulose membrane holds great potential for biomedical applications.

Guo et al. [84] explored the surface modification of carboxymethyl cellulose (CMC) films using boron nitride nanosheets (BNNSs) and 2-(methacryloyloxy)ethyltrimethylammonium chloride (DMC). BNNSs/PDMC were first prepared by anchoring α-bromoisobutyryl bromide (BiBB) to the nanosheets in the presence of 4-dimethylaminopyridine and triethylamine via esterification, followed by initiating DMC through ARGET ATRP. The resulting BNNSs/PDMC composite was then applied to CMC films by mixing them with deionized water and allowing the water to evaporate. The surface-modified BNNSs/PDMC cellulose films hence achieved a significant enhancement in mechanical properties. Indeed, the Young's modulus of the films increased by 729% as compared to pure CMC films.

Cellulose films are inherently a non-conductive material, but they possess excellent mechanical properties. To combine the advantages of cellulose with the conductive properties of other materials, various conductive substances have been introduced onto cellulose substrates. Chen et al. [85] reported the preparation of cellulose-based conductive films by simply incorporating active conductive materials, specifically graphite powder (GP) and polypyrrole (PPy), into the cellulose matrix. In their work, cellulose/PPy composite films were prepared by the polymerization of polypyrrole in a cellulose solution with dispersed graphite. The process involves dispersing GP in the ionic liquid 1-butyl-3-methylimidazolium chloride ([Bmim]Cl), followed by the addition of cellulose. This dispersion was then cast onto a plate and dried to form a graphite-containing cellulose film. The dried film was subsequently immersed in an iron chloride ($FeCl_3$) solution, which acted as both an oxidant and a doping agent. Fe(III) oxidized the pyrrole (Py) monomer into a radical to initiate polymerization and yield PPy within the cellulose matrix. As a result, the

composite film gained enhanced conductivity and thermal stability. Additionally, the conductive cellulose films displayed excellent electromagnetic shielding performance, owing to the strong shielding effect of the graphite powder.

1. 7 References

[1] Yang, H.; Tejado, A.; Alam, N.; Antal, M.; van de Ven, T. G. M., *Films prepared from electrosterically stabilized nanocrystalline cellulose.* Langmuir, 2012. 28(20): p. 7834-7842.

[2] Moradian, M.; Alam, M.N.; van de Ven, T. G. M, *Influence of carboxyl charge density on properties of extruded cellulose films.* Industrial & Engineering Chemistry Research, 2021. 60(38): p. 13756-13763.

[3] Payen, A., *Mémoire sur la composition du tissu propre des plantes et du ligneux.* Comptes rendus, 1838. 7(lu 17 décembre 1838): p. 1052-1056.

[4] Klemm, D.; Heublein, B.; Fink, H.P.; Bohn, A., *Cellulose: fascinating biopolymer and sustainable raw material.* Angewandte chemie international edition, 2005. 44(22): p. 3358-3393.

[5] Rojas, O.J., *Cellulose chemistry and properties: fibers, nanocelluloses and advanced materials*. Vol. 271. 2016: Springer.

[6] Rajinipriya, M.; Nagalakshmaiah, M.; Robert, M.;Elkoun, S., *Importance of agricultural and industrial waste in the field of nanocellulose and recent industrial developments of wood based nanocellulose: a review.* ACS Sustainable Chemistry & Engineering, 2018. 6(3): p. 2807-2828.

[7] Trache, D.; Tarchoun, A.F.; Derradji, M.; Hamidon, T.S.; Masruchin, N.; Brosse, N.; Hussin, M.H., *Nanocellulose: from fundamentals to advanced applications.* Frontiers in Chemistry, 2020. 8: p. 392.

[8] Rao, V.; Sundararajan, P.; Ramakrishnan, C.; Ramachandran, G., *Conformational studies of amylose*, in *Conformation of biopolymers*. 1967, Elsevier. p. 721-737.

[9] Hon, D. N. S., *Cellulose: a random walk along its historical path.* Cellulose, 1994. 1: p. 1-25.

[10] Krässig, H. A., *Cellulose: structure, accessibility and reactivity. Gordon and Breach Science, Yverdon.* 1993.

[11] Dukhin, A. S.; Goetz, P. J., *Acoustic and electroacoustic spectroscopy.* Langmuir, 1996. 12(18): p. 4336-4344.

[12] Dukhin, A. S.; Goetz, P. J., *Acoustic spectroscopy for concentrated polydisperse colloids with high density contrast.* Langmuir, 1996. 12(21): p. 4987-4997.

[13] Poisson, S. D. *Sur l'integration de quelques equations lineaires aux differnces partielles, et particulierement de l'equation generalie du mouvement des fluides elastiques,* Mem., de l'Institut, t.III, 1820, p. 121.

[14] Pellam, J. R.; Galt, J., *Ultrasonic propagation in liquids: I. Application of pulse technique to velocity and absorption measurements at 15 megacycles.* The journal of chemical physics, 1946. 14(10): p. 608-614.

[15] Sewell, C., *The extinction of sound in a viscous atmosphere by small obstacles of cylindrical and spherical form.* Philosophical Transactions of the Royal Society of London. Series A, Containing Papers of a Mathematical or Physical Character, 1911. 210(459-470): p. 239-270.

[16] Epstein, P. S.;Carhart, R. R., *The absorption of sound in suspensions and emulsions. I. Water fog in air.* J. acoust. soc. am, 1953. 25(3): p. 553-565.

[17] McClements, D. J., *Ultrasonic characterisation of emulsions and suspensions.* Advances in Colloid and Interface Science, 1991. 37(1-2): p. 33-72.

[18] Dukhin, A. S.; Goetz, P. J., *Acoustic and electroacoustic spectroscopy for characterizing concentrated dispersions and emulsions.* Advances in colloid and interface science, 2001. 92(1-3): p. 73-132.

[19] Dukhin, A. S.; Goetz, P. J.; van de Ven, T. G. M., *Ultrasonic characterization of proteins and blood cells.* Colloids and Surfaces B: Biointerfaces, 2006. 53(2): p. 121-126.

[20] Morse, P. M.; Ingard, K. U., *Theoretical acoustics*. 1986: Princeton university press.

[21] Rayleigh, J. W. S. B., *The theory of sound*. Vol. 2. 1896: Macmillan.

[22] Dukhin, A. S., *Ultrasound for Characterizing Colloids Particle Sizing, Zeta Potential Rheology*. 2002: Elsevier.

[23] Wood, A. B.; Lindsay, R., *A textbook of sound*. 1956, American Institute of Physics.

[24] Debye, P., *A method for the determination of the mass of electrolytic ions.* The Journal of chemical physics, 1933. 1(1): p. 13-16.

[25] Hermans, J. J., *Charged colloid particles in an ultrasonic field.* The London, Edinburgh, and Dublin Philosophical Magazine and Journal of Science, 1938. 25(168): p. 426-438.

[26] Frenkel, J., *On the theory of seismic and seismoelectric phenomena in a moist soil, republished at 2005.* Journal of Engineering Mechanics, 1944. 131(9): p. 879-887.

[27] Dukhin, A. S.; Goetz, P. J., *Characterization of aggregation phenomena by means of acoustic and electroacoustic spectroscopy.* Colloids and Surfaces A: Physicochemical and Engineering Aspects, 1998. 144(1-3): p. 49-58.

[28] Carasso, M. L.; Rowlands, W. N.;Kennedy, R. A., *Electroacoustic determination of droplet size and zeta potential in concentrated intravenous fat emulsions.* Journal of colloid and interface science, 1995. 174(2): p. 405-413.

[29] Safari, S.; Sheikhi, A.; van de Ven, T. G. M., *Electroacoustic characterization of conventional and electrosterically stabilized nanocrystalline celluloses.* Journal of colloid and interface science, 2014. 432: p. 151-157.

[30] Koshani, R.; van de Ven, T. G. M, *Electroacoustic characterization of trimmed hairy nanocelluloses.* Journal of colloid and interface science, 2020. 563: p. 252-260.

[31] Moradian, M.; van de Ven, T. G. M., *Formation of cellulose microspheres and nanocrystals from mildly carboxylated fibers.* Cellulose, 2022. 29(6): p. 3225-3237.

[32] Yousefi, N.; Wong, K. K.; Hosseinidoust, Z.; Sørensen, H. O.; Bruns, S.; Zheng, Y.; Tufenkji, N., *Hierarchically porous, ultra-strong reduced graphene oxide-cellulose nanocrystal sponges for exceptional adsorption of water contaminants.* Nanoscale, 2018. 10(15): p. 7171-7184.

[33] Tavakolian, M.; Lerner, J.; Tovar, F. M.; Frances, J.; van de Ven, T. G. M.; Kakkar, A., *Dendrimer directed assembly of dicarboxylated hairy nanocellulose.* Journal of colloid and interface science, 2019. 541: p. 444-453.

[34] Liu, X.; Xiao, W.; Ma, X.; Huang, L.; Ni, Y.; Chen, L.; Ouyang, X.; Li, J., *Conductive regenerated cellulose film and its electronic devices–a review.* Carbohydrate polymers, 2020. 250: p. 116969.

[35] Glasser, W. G.; Atalla, R. H.; Blackwell, J.; Malcolm Brown, R.; Burchard, W.; French, A. D.; Klemm, D. O.; Nishiyama, Y., *About the structure of cellulose: debating the Lindman hypothesis.* Cellulose, 2012. 19: p. 589-598.

[36] Swatloski, R. P.; Spear, S. K.; Holbrey, J. D.; Rogers, R. D., *Dissolution of cellulose with ionic liquids.* Journal of the American chemical society, 2002. 124(18): p. 4974-4975.

[37] Pinkert, A.; Marsh, K. N.; Pang, S.; Staiger, M. P., *Ionic liquids and their interaction with cellulose.* Chemical reviews, 2009. 109(12): p. 6712-6728.

[38] Ren, F.; Wang, J.; Xie, F.; Zan, K.; Wang, S.; Wang, S., *Applications of ionic liquids in starch chemistry: A review.* Green Chemistry, 2020. 22(7): p. 2162-2183.

[39] Zhang, H.; Wu, J.; Zhang, J.; He, J., *1-Allyl-3-methylimidazolium chloride room temperature ionic liquid: a new and powerful nonderivatizing solvent for cellulose.* Macromolecules, 2005. 38(20): p. 8272-8277.

[40] Xiong, B.; Zhao, P.; Hu, K.; Zhang, L.; Cheng, G., *Dissolution of cellulose in aqueous NaOH/urea solution: role of urea.* Cellulose, 2014. 21: p. 1183-1192.

[41] Qi, H.; Chang, C.; Zhang, L., *Effects of temperature and molecular weight on dissolution of cellulose in NaOH/urea aqueous solution.* Cellulose, 2008. 15: p. 779-787.

[42] Cai, J.; Zhang, L.; Liu, S.; Liu, Y.; Xu, X.; Chen, X.; Chu, B.; Guo, X.; Xu, J.; Cheng, H., *Dynamic self-assembly induced rapid dissolution of cellulose at low temperatures.* Macromolecules, 2008. 41(23): p. 9345-9351.

[43] Cai, J.; Zhang, L., *Rapid dissolution of cellulose in LiOH/urea and NaOH/urea aqueous solutions.* Macromolecular bioscience, 2005. 5(6): p. 539-548.

[44] Kong, W.; Yu, G.; Xing, J.; Zhang, H.; Liu, M.; Shi, Y., *Effect of the Dissolving Method on the Dissolution of Dissolving Pulp Cellulose Fibers with Different Dried-States in Different NaOH/Additives Aqueous Solutions.* Journal of Polymers and the Environment, 2021. 29(12): p. 3909-3917.

[45] Feng, L.; Chen, Z. l., *Research progress on dissolution and functional modification of cellulose in ionic liquids.* Journal of Molecular Liquids, 2008. 142(1-3): p. 1-5.

[46] Rosenau, T.; Potthast, A.; Sixta, H.; Kosma, P., *The chemistry of side reactions and byproduct formation in the system NMMO/cellulose (Lyocell process).* Progress in polymer science, 2001. 26(9): p. 1763-1837.

[47] Dogan, H.; Hilmioglu, N. D., *Dissolution of cellulose with NMMO by microwave heating.* Carbohydrate Polymers, 2009. 75(1): p. 90-94.

[48] Chrapava, S.; Touraud, D.; Rosenau, T.; Potthast, A.; Kunz, W., *The investigation of the influence of water and temperature on the LiCl/DMAc/cellulose system.* Physical Chemistry Chemical Physics, 2003. 5(9): p. 1842-1847.

[49] Potthast, A.; Rosenau, T.; Sixta, H.; Kosma, P., *Degradation of cellulosic materials by heating in DMAc/LiCl.* Tetrahedron Letters, 2002. 43(43): p. 7757-7759.

[50] Huang, H.-D.; Liu, C.-Y.; Zhang, L.-Q.; Zhong, G.-J.; Li, Z.-M., *Simultaneous reinforcement and toughening of carbon nanotube/cellulose conductive nanocomposite films by interfacial hydrogen bonding.* ACS Sustainable Chemistry & Engineering, 2015. 3(2): p. 317-324.

[51] Zhou, J.; Zhang, L., *Solubility of cellulose in NaOH/urea aqueous solution.* Polymer journal, 2000. 32(10): p. 866-870.

[52] Röder, T.; Morgenstern, B., *The influence of activation on the solution state of cellulose dissolved in N-methylmorpholine-N-oxide-monohydrate.* Polymer, 1999. 40(14): p. 4143-4147.

[53] Willberg-Keyriläinen, P., & Ropponen, J., *Evaluation of esterification routes for long chain cellulose esters*. Heliyon, 2019. *5*(11).

[54] Weißl, M.; Hobisch, M.A.; Johansson, L.S.; Hettrich, K.; Kontturi, E.; Volkert, B.; Spirk, S., *Cellulose carbamate derived cellulose thin films: preparation, characterization and blending with cellulose xanthate.* Cellulose, 2019. 26: p. 7399-7410.

[55] Zhao, Y.; Zhou, S.; Xia, X.; Tan, M.; Lv, Y.; Cheng, Y.; Tao, Y.; Lu, J.; Du, J.; Wang, H., *High-performance carboxymethyl cellulose-based hydrogel film for food packaging and*

preservation system. International Journal of Biological Macromolecules, 2022. 223: p. 1126-1137.

[56] Ebrahimi, Y.; Peighambardoust, S. J.; Peighambardoust, S.H.; Karkaj, S. Z., *Development of antibacterial carboxymethyl cellulose-based nanobiocomposite films containing various metallic nanoparticles for food packaging applications.* Journal of Food Science, 2019. 84(9): p. 2537-2548.

[57] Sheikh, J.; Bramhecha, I.; Teli, M., *Recycling of terry towel (cellulosic) waste into carboxymethyl cellulose (CMC) for textile printing.* Fibers and Polymers, 2015. 16: p. 1113-1118.

[58] Pettignano, A.; Charlot, A.; Fleury, E., *Carboxyl-functionalized derivatives of carboxymethyl cellulose: Towards advanced biomedical applications.* Polymer Reviews, 2019. 59(3): p. 510-560.

[59] Ogushi, Y.; Sakai, S.; Kawakami, K., *Synthesis of enzymatically-gellable carboxymethylcellulose for biomedical applications.* Journal of bioscience and bioengineering, 2007. 104(1): p. 30-33.

[60] Mittal, H.; Al Alili, A.; Morajkar, P. P.; Alhassan, S. M., *GO crosslinked hydrogel nanocomposites of chitosan/carboxymethyl cellulose–A versatile adsorbent for the treatment of dyes contaminated wastewater.* International Journal of Biological Macromolecules, 2021. 167: p. 1248-1261.

[61] El-Shafai, N. M.; Ibrahim, M. M.; Abdelfatah, M.; Ramadan, M. S.; El-Mehasseb, I. M., *Synthesis, characterization, and cytotoxicity of self-assembly of hybrid nanocomposite*

modified membrane of carboxymethyl cellulose/graphene oxide for photocatalytic antifouling, energy storage, and supercapacitors application. Colloids and Surfaces A: Physicochemical and Engineering Aspects, 2021. 626: p. 127035.

[62] Moradian, M.; Islam, M. S.; van de Ven, T. G. M., *Insoluble regenerated cellulose films made from mildly carboxylated dissolving and kraft pulps.* Industrial & Engineering Chemistry Research, 2021. 60(15): p. 5385-5393.

[63] Yang, H.; Alam, M. N.; van de Ven, T. G. M., *Highly charged nanocrystalline cellulose and dicarboxylated cellulose from periodate and chlorite oxidized cellulose fibers.* Cellulose, 2013. 20: p. 1865-1875.

[64] Sharma, A.; Thakur, M.; Bhattacharya, M.; Mandal, T.; Goswami, S., *Commercial application of cellulose nano-composites–A review.* Biotechnology Reports, 2019. 21: p. e00316.

[65] Vatanpour, V.; Pasaoglu, M. E.; Barzegar, H.; Teber, O. O., Kaya, R.; Bastug, M.; Khataee, A & Koyuncu, I., (2022). *Cellulose acetate in fabrication of polymeric membranes: A review.* Chemosphere*, 295*, 133914.

[66] Mendes, I. S.; Prates, A.; Evtuguin, D. V., *Production of rayon fibres from cellulosic pulps: state of the art and current developments.* Carbohydrate Polymers, 2021. 273: p. 118466.

[67] Wilkes, A. G., *The viscose process.* Regenerated cellulose fibres, 2001: p. 37-61.

[68] Gondhalekar, S. C.; Pawar, P. J.; Dhumal, S. S.; Thakre, S., *Fate of CS_2 in viscose process: a chemistry perspective.* Cellulose, 2022. 29(3): p. 1451-1461.

[69] Sisson, W. A., *The spinning of rayon as related to its structure and properties.* Textile Research Journal, 1960. 30(3): p. 153-170.

[70] Mitchell, R., *Viscose processing of cellulose.* Industrial & Engineering Chemistry, 1949. 41(10): p. 2197-2201.

[71] Wardman, R. H., *An introduction to textile coloration: principles and practice*. 2017: John Wiley & Sons.

[72] Amokrane, G.; Falentin-Daudré, C.; Ramtani, S.; Migonney, V., *A simple method to functionalize PCL surface by grafting bioactive polymers using UV irradiation.* Irbm, 2018. 39(4): p. 268-278.

[73] Correa, D.; Medeiros, E.; Oliveira, J.; Paterno, L.; Mattoso, L. H., *Nanostructured conjugated polymers in chemical sensors: synthesis, properties and applications.* Journal of nanoscience and nanotechnology, 2014. 14(9): p. 6509-6527.

[74] Moradian, M.; Wiebe, H.; van de Ven, T. G. M, *Ultrathin ultrastrong transparent films made from regenerated cellulose and epichlorohydrin.* Carbohydrate Polymers, 2023. 318: p. 121131.

[75] Huang, X.; Andry, S.; Yaputri, J.; Kelly, D.; Ladner, D.A.; Whelton, A. J., *Crude oil contamination of plastic and copper drinking water pipes.* Journal of hazardous materials, 2017. 339: p. 385-394.

[76] Gu, R.; Yun, H.; Chen, L.; Wang, Q.; Huang, X., *Regenerated cellulose films with amino-terminated hyperbranched polyamic anchored nanosilver for active food packaging.* ACS Applied Bio Materials, 2019. 3(1): p. 602-610.

[77] Koshani, R.; Zhang, J.; van de Ven, T. G. M.; Lu, X.; Wang, Y., *Modified hairy nanocrystalline cellulose as photobactericidal nanofillers for food packaging application.* ACS Sustainable Chemistry & Engineering, 2021. 9(31): p. 10513-10523.

[78] Pirsa, S., Shamusi, T., & Kia, E. M. (2018). Smart films based on bacterial cellulose nanofibers modified by conductive polypyrrole and zinc oxide nanoparticles. *Journal of Applied Polymer Science*, *135*(34), 46617.

[79] Sim, G.; Liu, Y.; van de Ven, T. G. M. Transparent composite films prepared from chemically modified cellulose fibers, Cellulose 23 (2016) 2011-2024.

[80] Keller, P. E.; Kouzes, R. T. Water vapor permeation in plastics[R]. Pacific Northwest National Lab. (PNNL), Richland, WA (United States), 2017.

[81] Li, W.; Wu, Y.; Liang, W.; Li, B.; Liu, S., *Reduction of the water wettability of cellulose film through controlled heterogeneous modification.* ACS Applied Materials & Interfaces, 2014. 6(8): p. 5726-5734.

[82] Maver, T.; Maver, U.; Mostegel, F.; Griesser, T.; Spirk, S.; Smrke, D.M.; Stana-Kleinschek, K., *Cellulose based thin films as a platform for drug release studies to mimick wound dressing materials.* Cellulose, 2015. 22: p. 749-761.

[83] Wang, M.; Yuan, J.; Huang, X.; Cai, X.; Li, L.; Shen, J., *Grafting of carboxybetaine brush onto cellulose membranes via surface-initiated ARGET-ATRP for improving blood compatibility.* Colloids and Surfaces B: Biointerfaces, 2013. 103: p. 52-58.

[84] Guo, M.; Wu, Y.; Xue, S.; Xia, Y.; Zhang, R.; Liu, D.; Lei, W.; Zhang, T., *Surface modification of boron nitride nanosheets with polycationic electrolytes through ARGET ATRP for enhancing mechanical properties of cellulose film.* Materials Letters, 2019. 242: p. 127-130.

[85] Chen, J.; Xu, J.; Wang, K.; Qian, X.; Sun, R., *Highly thermostable, flexible, and conductive films prepared from cellulose, graphite, and polypyrrole nanoparticles.* ACS applied materials & interfaces, 2015. 7(28): p. 15641-15648.

Preface to Chapter 2

As outlined in Chapter 1, both acoustic spectroscopy and electroacoustics have proven to be highly effective techniques for characterizing cellulose-based materials. These methods offer significant advantages over traditional techniques, such as light scattering, by enabling precise measurements of particle size distribution and zeta potential. Notably, these measurements can be taken even in concentrated systems, without the need for sample dilution— a limitation commonly encountered with other methods. Moreover, acoustic spectroscopy provides the unique advantage of real-time, non-invasive monitoring, making it particularly well-suited for studying the complex behavior of nanocellulose, a material of growing importance in emerging technologies.

Given the numerous benefits of acoustic techniques, we aim to characterize cellulose dope using acoustic spectroscopy. The dope consists of a mixture of dissolved cellulose polymer, nanocellulose particles, and salts. In this chapter, we focus on characterizing the salts within the dope using sound speed. We begin by deriving an equation that establishes a relationship between sound speed and volume fraction. Using this equation, we measured the sound speed of 11 different salts and incorporated these values to calculate the intrinsic sound speed of each salt. This theoretical framework provides the basis for predicting the potential composition of an unknown solution, offering valuable insights into its characteristics.

Chapter 2

Cations and Anions Affect the Speed of Sound in Water Oppositely

2. 1 Abstract

Identifying the composition of a solution using acoustics remains a challenge. It is known that for low salt concentrations, the speed of sound in water increases linearly with the concentration of electrolytes, but the contribution of individual cations is unknown. We introduce the concept of the intrinsic sound speed A_i to quantify the contribution of ions to the speed of sound. We found that cations increase the speed of sound in water, whereas anions decrease the speed of sound. Hydration layers around ions play a major role. Because cations have a thicker hydration layer than anions, their contribution to the speed of sound is larger than that of anions. Experimental data on salts not used to determine the contribution of individual ions are in quantitative agreement with predicted values. Our method is applicable to various systems containing small quantities of ions, molecules, or particles. With the knowledge that cations increase the speed of sound, we were able to explain previously unexplained data in the literature.

Figure 2. 1 TOC GRAPHICS

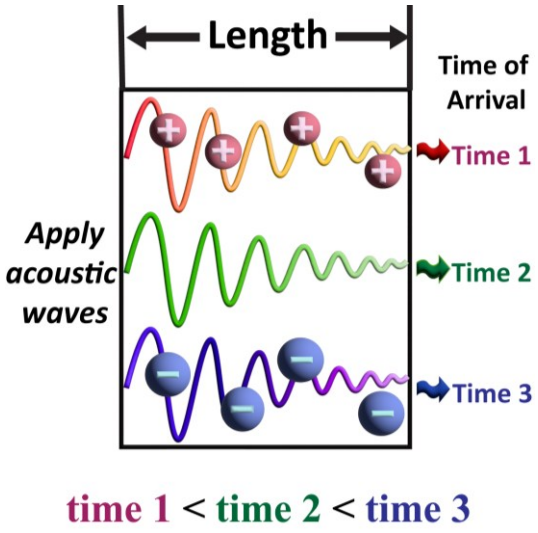

KEYWORDS Speed of sound of electrolytes; Contribution of ions to speed of sound; hydrated ions; intrinsic sound speed

2. 2 Introduction

Acoustic spectroscopy employs non-destructive and low-energy ultrasound for extracting information, including the speed of sound. Ultrasound can penetrate materials that are opaque to light, opening up a wide range of novel applications that are not achievable with traditional light scattering techniques. Compared to conventional light-based approaches, they are substantially less susceptible to contamination because the high particle concentration in the sample overwhelms any little residual from the old sample [1[. Therefore, the characterization of solution or even concentrated dispersion can be achieved by acoustic spectroscopy. Acoustics has been widely used in gas sensing [2[and underwater sensor networks [3-6]. Sound speed measurements have been used for the determination of the energy loss in a liquid sample [7]. Millero et al. reported positive transitions in the speed of sound in certain concentrated aqueous solutions, largely attributed to the hydration layer of cations [8]. The mechanism of sound propagation in supercritical liquid was found to be related to the adiabatic-to-isothermal crossover [9].

At the molecular level, sound speeds and Debye temperatures were measured to characterize the crystal lattice stiffness and its elastic properties [10-14]. Acoustics has also been used to determine the speed of sound in different electrolyte solutions, however, how different electrolytes contribute to the change in speed of sound remains obscure. Wood has derived a relationship between the speed of sound and volume fraction for suspensions of particles [15]. For small-volume fractions, the Wood equation can be simplified to the following equation [16].

$$\frac{c_s}{c_m} = 1 + (1 - \frac{\rho_p{}^2 + B\rho_m{}^2}{2\rho_p\rho_m})\varphi \quad \text{with } B = (\frac{c_m}{c_p})^2 \qquad \text{Equ 1}$$

where ρ_p and ρ_m are the densities of the particles and the medium, c_s, c_p, and c_m are the sound speed in the whole suspension, in particles, and in the liquid medium, respectively and φ is the volume fraction. For low volume fractions, the speed of sound changes linearly with volume fraction. Depending on whether the term $1-\frac{\rho_p^2+B\rho_m^2}{2\rho_p\rho_m}$ is positive or negative, the speed of sound can either increase or decrease with volume fraction. This equation is consistent with other experimental investigations. Maisano et al.[17] and Ebrahimi et al.[18] showed an increase in sound velocity with polymer concentration in binary and ternary systems. The addition of salts would also induce a change in polymer hydration, thus leading to a change in the speed of sound [17].

To the best of our knowledge, there is no report regarding the effects of individual ions on the speed of sound. In this paper, for the first time, we propose a theory that quantifies the contribution of individual ions to the speed of sound. Initially, the speed of sound of eleven different salts was experimentally determined. We use the following equation to model the theoretical contribution of each ion to the speed of sound.

$$\frac{c_s}{c_m}=1+\sum_1^n A_i\varphi_1 \qquad \text{Equ 2}$$

Here φ_1 is the volume fraction of ion i and A_i is the intrinsic ion sound speed.

Analogous to the Wood equation, in which for low concentrations the increase in sound speed is proportional to volume fraction, we hypothesize that the contribution of each ion to the speed of sound is also proportional to its volume fraction, with the proportionality constant determined by the type of ion. The volume fraction of ions was calculated based on their hydrated ion radii. After the intrinsic ion sound speed of several ions was obtained from the experiment, the speeds of the

sound of other salts were measured and compared with theoretical predictions to examine the validity of the proposed theory.

2. 3 Results and Discussion

The speed of sound for different salts was first measured for various salt concentrations. The speed of sound in solutions of 11 salts is presented in Figure 2. 2, 10 of which show a consistent upward trend in the speed of sound with the molarity of the salts. NaI shows a slight downward trend. Our data reveal that sodium sulfate (Na_2SO_4) and sodium carbonate (Na_2CO_3) cause the most significant increase in the speed of sound with increasing concentration, whereas hydrochloric acid (HCl) displays the smallest increase in the speed of sound among all these salts studied. Despite some slight differences, these observations are consistent with other work [19-24] as can be seen in Table 1, in which the changes in the speed of sound of this work are compared to literature values.

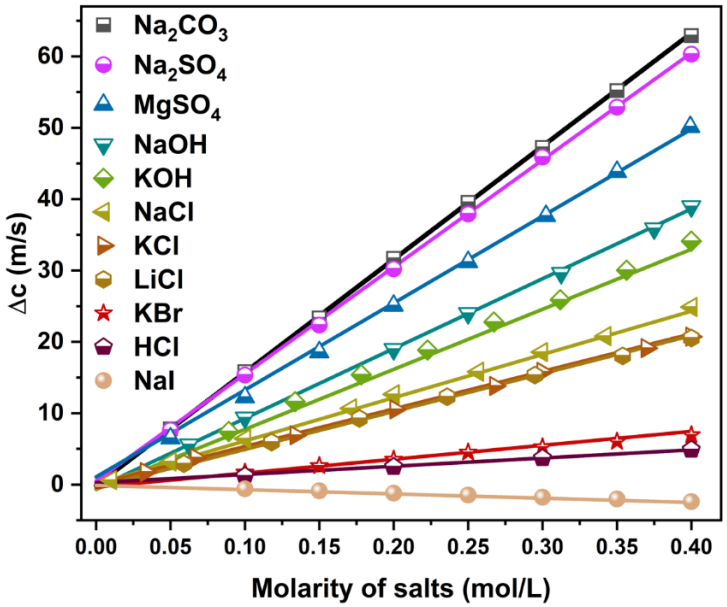

Figure 2. 2 Change in the speed of sound ($\Delta c = c_s - c_m$) in water for various salt solutions as a function of molarity

Table 2. 1 Change in speed of sound in water at 1 atm

	Experimental (23°C, 0.4M, this work)	From Reference*
LiOH	33.94	~45 (0.52M) [20] ~27 (0.32M) [20]
NaOH	38.26	38.78[22] ~62 (0.68M) [20]
KOH	34.11	~41 (0.50M) ~19 (0.25M) [20]
LiCl	20.54	23.02 (0.434M) [22] ~32 (30 °C, 0.5mol/kg) [19]
NaCl	24.87	24.76 [22] ~36 (30°C, 0.5mol/kg) [19] 2.22 (20°C, 0.035mol/kg) [24] 31.03 (25°C, 0.50410mol/kg) [23]
KCl	20.71	21.00[24], 23.14 (5°C, 0.3595M) [21] ~31 (30°C, 0.5M) [19] 1.88 (20°C, 0.035mol/kg) [24]
NaI	-2.40	-2.59[22]
KI	-6.36	-6.06[22]
KBr	6.95	7.11[22]
NaBr	11.11	10.72[22]
Na_2SO_4	60.32	60.16[22] 5.9 (20°C, 0.035mol/kg) [24] 50.72 (25°C, 0.33369mol/kg) [23]
K_2SO_4	51.93	51.33[22]
Na_2CO_3	62.90	62.74[22] 6.4 (20°C, 0.035mol/kg) [24]

K_2CO_3	60.33	60.29[22]
HCl	4.90	4.94[22]
MgSO4	50.12	59.47at 0.48 M[22] 38.33 (25°C, 0.30801mol/kg) [23]
$MgCl_2$	44.23	49.43 at 0.46 M[22], 4.44 (20°C, 0.035mol/kg) [24] 43.99 (25°C, 0.40946mol/kg) [23]
H_2SO_4	-4.22	~-3.80 (20°C) [25]

*The measurements were taken at 25°C and 0.4M if not specified otherwise.

The speed of sound is described by equation 2, applicable for low salt volume fractions. We used salt solutions containing 11 different ions. Measuring the increase in the speed of sound in these 11 salt solutions yields 11 equations with 11 unknowns, which can be solved to give the intrinsic sound speed A_i。 $A_{Na^+}, A_{K^+}, A_{Li^+}, A_{OH^-}, A_{Cl^-}$ were obtained first by applying this equation to 0.4 M salt solutions of NaOH, KOH, LiCl, NaCl and KCl and the procedure was next applied to KBr, Na_2SO_4, Na_2CO_3, Mg_2SO_4, NaI and HCl to obtain A_{Br^-}, $A_{SO_4{}^{2-}}, A_{CO_3{}^{2-}}, A_{Mg^{2+}}, A_{H^+}, A_{I^-}$, respectively.

Volume fraction φ was taken as the hydrated volume fraction of ions with $\varphi = \frac{N_A \times n \times V}{V_w}$. φ^+ and φ^- are the volume fraction of cations and anions, respectively. N_A is Avogadro's number, n is the amount of substance (mol) of ions, V is the hydrated volume of an ion, V_w is the volume of the solution. The radii of ions are listed in Table 2.

The results are presented in Figure 2. 3, which reveals that the contribution A_i depends on the charge polarity of ions. Cations contribute positively to the sound speed, whereas anions contribute

negatively. The most probable solvation arrangement for the hydrated proton is a distorted Eigen-type complex ($H_9O_4^+$) [26]. Thus, the intrinsic sound speed of the proton was obtained from the volume of $H_9O_4^+$ and was calculated to be the lowest among all the studied cations, perhaps because the hydration layer around a proton is less ice-like than hydration layers around other cations.

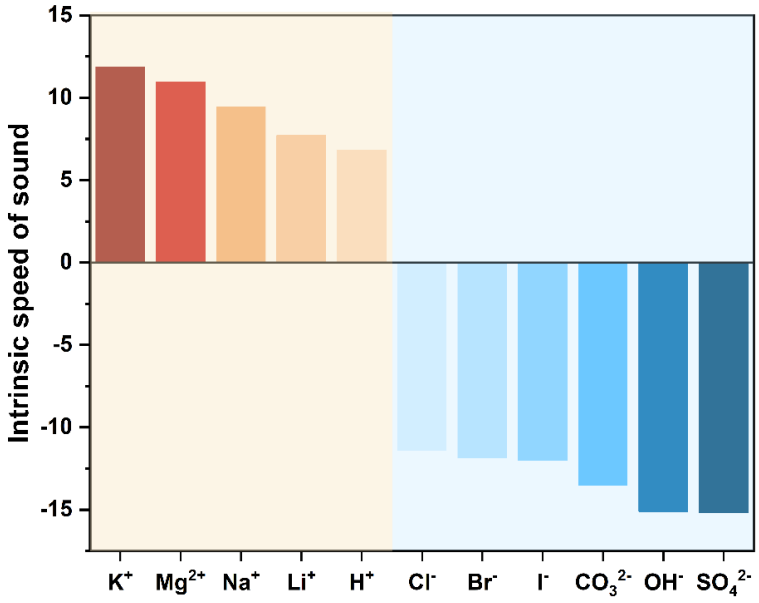

Figure 2. 3 Intrinsic speed of sound A_i (defined in eq.2)

The 11 intrinsic speed of sound A_i can be further used to calculate the speed of sound of other salts such as sodium bromide (NaBr), magnesium chloride ($MgCl_2$), potassium carbonate (K_2CO_3), lithium hydroxide (LiOH), potassium sulfate (K_2SO_4) and potassium iodide (KI), using Equ 2. The results are shown in Figure 2. 4. Figure 2. 4 provides a comparison between the theoretical and experimental speeds of sound in different salt solutions vs. molarity ranging from 0-0.4 M. Notably, it is evident that the calculated speed of sound varies linearly with molarity (0-0.4M) for all the six salts tested. Most of the theoretical values closely align with experimental values. There is a small

discrepancy for K_2CO_3, which might be related to the ionization of the carbonate ion [27], as in slightly acidic water, bicarbonate ion (HCO_3-) and CO_3^{2-} are both present. The discrepancy might also be attributed to the formation of $HCO_3^-\cdot nH_2O$ clusters and the hydrogen bonding between them [28]. A slight discrepancy also occurred for $MgCl_2$. This is mainly because A_{Mg2+} is calculated from $MgSO_4$ in which solution species other than Mg^{2+} and SO_4^{2-} are present, such as bisulfate anions [29, 30]. This can be concluded from various studies on H_2SO_4 solutions, in which the coexistence of diverse ion species within the solution, encompassing sulfate ions, bisulfate ions and hydronium ions have been demonstrated [28]. These species can further form various clusters, ion pairs and engage in hydrogen bonding. Wang et al [31] and Yacovitch et al [32] observed $SO_4^{2-}(H_2O)_n$ clusters (n=3-10) and $HSO_4^-(H_2O)_n$ clusters (n=1-16), respectively, shedding light on the complexity of species formation and interactions within H_2SO_4. Meanwhile, the difference in the solvation configuration of hydrated protons also significantly affects the speed of sound, particularly due to the presence of two hydrogen ions in sulfuric acid [26]. Because of the uncertainties which ions and clusters are present in H_2SO_4 solutions, we made no attempt to compare it with theory. The decrease in the speed of sound in dilute H_2SO_4 solutions, has been found by others [25].

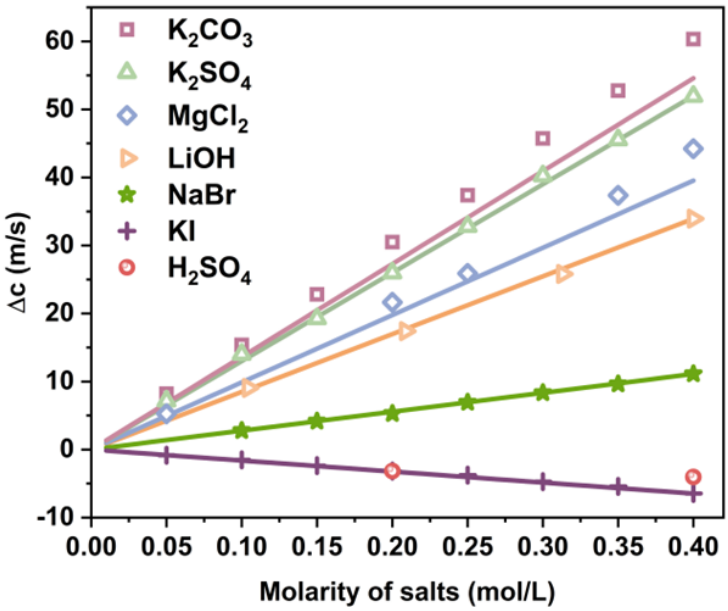

Figure 2. 4 Experimental and theoretical speed of sound of K_2CO_3, K_2SO_4, $MgCl_2$, LiOH, NaBr, H_2SO_4 and KI solutions with molarity in the range of 0-0.4 M; The experimental data are expressed as symbols and theoretical data are expressed as lines. Data for H_2SO_4 are not fitted (see text).

We did not observe any discrepancies between K_2SO_4 and Na_2SO_4 because the large contribution of the two cations in each sample nearly eliminates any small discrepancies in SO_4^{2-}.

In aqueous salt solutions, ions are surrounded by hydration layers consisting of water molecules, and therefore, the hydrated ion radii were used in the calculation of A_i. We can assume that the intrinsic speed of sound of the hydration layer is larger than that of bulk water, because it is more ordered and is ice-like [33-35]. Given that the speed of sound in ice is higher than that in water, hydration layers are expected to increase the speed of sound in water. Because cations have larger hydration layers than anions (see Table 2), the intrinsic speed of sound of hydrated layers to the

speed of sound is large for cations and small for anions, for which the bare ion radii contribute most.

Table 2. 2 Hydrated and bare ionic radii (nm)

	Hydrated Ionic Radii	Bare Ionic Radii
H^+	0.395 [36] *	-
Li^+	0.382 [36-38]	0.094 [36]
Na^+	0.358 [37-39]	0.095 [37, 39]
K^+	0.331 [37, 39-41]	0.133 [37]
Mg^{2+}	0.428 [37, 40]	0.072 [37]
OH^-	0.300 [38, 39, 41, 42]	0.176 [37]
Cl^-	0.332 [37-41]	0.181 [39]
Br^-	0.330 [38, 39]	0.195 [39]
I^-	0.331 [36]	0.205 [36]
SO_4^{2-}	0.379 [37-39, 41]	0.290 [37, 39]
CO_3^{2-}	0.394 [37, 38, 42]	0.266 [37, 38]

* Corresponding to $H_9O_4^+$

Due to the substantial volume fraction of the hydration layer, its positive impact is rather significant. Consequently, for all salts tested, the magnitude of the negative effect on the speed of sound due to anions was less than the increase in the speed of sound caused by the hydration layer of cations, resulting in a general increase in sound speed in electrolyte solutions.

These findings provide empirical proof for the theory that both volume fraction and ion polarity play a crucial role in affecting the speed of sound in the salts tested. The simplest explanation of the observed effects is that bare ions contribute negatively to the speed of sound and hydration layers contribute positively. Because the hydration layer for cations is larger than anions, hydrated cations contribute positively to the speed of sound, whereas hydrated anions contribute negatively. The possibility exists that some large bulky cations might reduce the speed of sound, as the contribution of the bare ion might exceed that of the hydration layer.

2. 4 Concluding remarks

In this paper, we have shown that the speed of sound in an electrolyte solution is influenced by the volume fraction of all ions present. We have found that cations with large hydration layers contribute positively, while anions contribute negatively to the speed of sound. The increase in the speed of sound is described very well by an equation in which the contribution of each ion to the speed of sound is proportional to its volume fraction, calculated from hydrated ion sizes. This equation can be applied for all systems containing small amounts of ions, molecules, or particles. With the knowledge that cations contribute largely to an increase in the sound speed in water, we can explain data presented in Koshani and van de Ven [43], who found that the increase in the speed of sound in a 1% solution of highly charged dicarboxylated cellulose (DCC) was much larger than the increase in a 1% dispersion of weakly charged cellulose nanocrystals. Since the DCC solution contained many sodium counterions, their contribution to the increase in sound speed was the dominant contribution.

2. 5 Material and Methods

Materials. Sodium bromide (NaBr, ≥99%) was purchased from fisher scientific, Lithium hydroxide (LiOH, anhydrous, 98%), potassium chloride (KCl, ≥99%), was purchased from Thermo Fisher scientific. Potassium carbonate (K_2CO_3, ≥99%), magnesium chloride ($MgCl_2$, anhydrous, ≥98%), sodium chloride (NaCl, >99%), potassium hydroxide (KOH, ≥99.99%), potassium sulfate (K_2SO_4, ≥99.0%), lithium chloride (LiCl, ≥99%), potassium bromide(KBr, ≥99%), hydrochloric acid (HCl, 37%), sodium carbonate (Na_2CO_3, ≥99.5%), sodium sulfate

(Na_2SO_4, ≥99%), magnesium sulfate ($MgSO_4$, anhydrous, ≥99.5%), sulfuric acid (H_2SO_4, 95%-98%), potassium iodide (KI, ≥99%) was purchased from Sigma-Aldrich.

Preparation and measurement of the speed of sound of salt solutions. Salts were first put in a 50℃ oven for 4 hours to remove the moisture. Solutions were prepared by measuring certain amounts of salts on a balance and mixing them with 100 mL of distilled water. The mixtures were then sealed in tubes immediately. The tubes were fully immersed in a 23 ± 0.1°C water bath and stirred for 20 minutes.

To measure the speed of sound of salt solutions, an Acoustic Spectrometer DT-1202 (Dispersion Technology, Bedford Hills, NY, USA) composed of a servomotor with transducer, dispersion chamber and a detector, was used. A solution was poured into dispersion chamber which was covered by tin foil to avoid evaporation which might lead to a small temperature change. The temperature was monitored manually and found to be constant at 23°C ± 0.1°C during each measurement. The acoustic sensor measures the sound speed at 10 MHz under 1 atm. At least seven independent measurements have been conducted for each molarity of each salt. The standard deviation was computed for each molarity. Comprehensive instructions and operational methods are available in the book by Dukhin and Goetz and the operating manual [44, 45].

2. 6 Acknowledgements

This work was supported by NSERC Discovery grant RGPIN-2018-05781. We thank Dr. Andei Dukhin for valuable suggestions.

2. 7 References

[1] Dukhin, A. S.; Goetz, P. J. Acoustic and electroacoustic spectroscopy for characterizing concentrated dispersions and emulsions. *Adv Colloid Interface Sci.* **2001**, *92*, 73-132, DOI: 10.1016/s0001-8686(00)00035-x

[2] Liu, S.; Zhu, M.; Yang, J.; Wu, J. Identifying gas composition based on the decomposed relaxation strength from sound-speed dispersion. *Appl. Acoust.* **2023**, *206*, 109264, DOI: https://doi.org/10.1016/j.apacoust.2023.109264

[3] Masmitja, I.; Navarro, J.; Gomariz, S.; Aguzzi, J.; Kieft, B.; O'Reilly, T.; Katija, K.; Bouvet, P. J.; Fannjiang, C.; Vigo, M. Mobile robotic platforms for the acoustic tracking of deep-sea demersal fishery resources. *Sci. Robot.* **2020**, *5*, eabc3701, DOI: 10.1126/scirobotics.abc3701

[4] Consortium, A. Ocean climate change: Comparison of acoustic tomography, satellite altimetry, and modeling. *Science.* **1998**, *281*, 1327-1332, DOI: 10.1126/science.281.5381.1327

[5] Wunsch, C. Advance in global ocean acoustics. *Science.* **2020**, *369*, 1433-1434, DOI: 10.1126/science.abe0960

[6] Dyer, I.; Dahl, P. H.; Baggeroer, A. B.; Mikhalevsky, P. N. Ocean dynamics and acoustic fluctuations in the fram strait marginal ice zone. *Science.* **1987**, *236*, 435-436, DOI: 10.1126/science.236.4800.435

[7] Yamaguchi, T.; Dukhin, A.; Ryu, Y. J.; Zhang, D.; Borodin, O.; González, M. A.; Yamamuro, O.; Price, D. L.; Saboungi, M.-L. Non-newtonian dynamics in water-in-salt electrolytes. *J. Phys. Chem. Lett.* **2023**, *15*, 76-80, DOI: https://doi.org/10.1021/acs.jpclett.3c03145

[8] Millero, F. J.; Fernandez, M.; Vinokurova, F. Transitions in the speed of sound in concentrated aqueous electrolyte solutions. *J. Phys.Chem*. **1985**, *89*, 1062-1064, DOI: https://doi.org/10.1021/j100253a002

[9] Bolmatov, D.; Zhernenkov, M.; Zav'yalov, D.; Stoupin, S.; Cai, Y. Q.; Cunsolo, A. Revealing the mechanism of the viscous-to-elastic crossover in liquids. *J. Phys. Chem. Lett.* **2015**, *6*, 3048-3053, DOI: https://doi.org/10.1021/acs.jpclett.5b01338

[10] Slade, T. J.; Pal, K.; Grovogui, J. A.; Bailey, T. P.; Male, J.; Khoury, J. F.; Zhou, X.; Chung, D. Y.; Snyder, G. J.; Uher, C. Contrasting SnTe–$NaSbTe_2$ and SnTe–$NaBiTe_2$ thermoelectric alloys: high performance facilitated by increased cation vacancies and lattice softening. *J. Am. Chem. Soc*. **2020**, *142*, 12524-12535, DOI: https://doi.org/10.1021/jacs.0c05650

[11] Xie, H.; Su, X.; Hao, S.; Zhang, C.; Zhang, Z.; Liu, W.; Yan, Y.; Wolverton, C.; Tang, X.; Kanatzidis, M. G. Large thermal conductivity drops in the diamondoid lattice of $CuFeS_2$ by discordant atom doping. *J. Am. Chem. Soc*. **2019**, *141*, 18900-18909, DOI: https://doi.org/10.1021/jacs.9b10983

[12] Kraft, M. A.; Culver, S. P.; Calderon, M.; Böcher, F.; Krauskopf, T.; Senyshyn, A.; Dietrich, C.; Zevalkink, A.; Janek, J. r.; Zeier, W. G. Influence of lattice polarizability on the ionic

conductivity in the lithium superionic argyrodites Li_6PS_5X (X= Cl, Br, I). *J. Am. Chem. Soc.* **2017**, *139*, 10909-10918, DOI: https://doi.org/10.1021/jacs.7b06327

[13] Das, A.; Pal, K.; Acharyya, P.; Das, S.; Maji, K.; Biswas, K. Strong antibonding I (p)–Cu (d) states lead to intrinsically low thermal conductivity in $CuBiI_4$. *J. Am. Chem. Soc.* **2023**, *145*, 1349-1358, DOI: https://doi.org/10.1021/jacs.2c11908

[14] Ma, N.; Li, F.; Li, J. G.; Liu, X.; Zhang, D. B.; Li, Y. Y.; Chen, L.; Wu, L. M. Mixed-Valence $CsCu_4Se_3$: Large phonon anharmonicity driven by the hierarchy of the rigid $[(Cu^{+})_4 (Se^{2-})_2](Se^{-})$ double anti-CaF_2 layer and the soft Cs^{+} sublattice. *J. Am. Chem. Soc.* **2021**, *143*, 18490-18501, DOI: https://doi.org/10.1021/jacs.1c07629

[15] Wood, A. B. A Textbook of Sound. *Bell,* London, **1941**.

[16] Dukhin, A. S.; Goetz, P. J.; van de Ven, T. G. M. Ultrasonic characterization of proteins and blood cells. *Colloids. Surf B. Biointerfaces.* **2006**, *53*, 121-126, DOI: 10.1016/j.colsurfb.2006.08.011

[17] Maisano, G.; Majolino, D.; Migliardo, P.; Venuto, S.; Aliotta, F.; Magazú, S. Sound velocity and hydration phenomena in aqueous polymeric solutions. *Mol. Phys.* **1993**, *78*, 421-435, DOI: https://doi.org/10.1080/00268979300100311

[18] Ebrahimi, S.; Sadeghi, R. Density, speed of sound, and viscosity of some binary and ternary aqueous polymer solutions at different temperatures. *J. Chem. Eng. Data.* **2015**, *60*, 3132-3147, DOI: https://doi.org/10.1021/acs.jced.5b00290

[19] Uedaira, H.; Suzuki, Y. Ultrasonic velocity and compressibility in aqueous solutions of alkali metal chlorides. *Bull. Chem. Soc. Japan.* **1979**, *52*, 2787-2790, DOI: https://doi.org/10.1246/bcsj.52.2787

[20] Marks, G. W. Dependence of acoustic velocity in some aqueous hydroxide solutions on temperature and concentration. *J. Acoust. Soc. Am.* **1960**, *32*, 327-335, DOI: https://doi.org/10.1121/1.1908047

[21] Kumar, A. Speed of sound in concentrated aqueous KCl solutions from 278.15 to 338.15 K. *J. Chem. Eng. Data.* **2003**, *48*, 388-391, DOI: https://doi.org/10.1021/je025605k

[22] Millero, F. J.; Ward, G. K.; Chetirkin, P. V. Relative sound velocities of sea salts at 25 °C. *J. Acoust. Soc. Am.* **1977**, *61*, 1492-1498, DOI: https://doi.org/10.1121/1.381449

[23] Chen, C. T.; Chen, L. S.; Millero, F. J. Speed of sound in NaCl, $MgCl_2$, Na_2SO_4, and $MgSO_4$ aqueous solutions as functions of concentration, temperature, and pressure. *J. Acoust. Soc. Am.* **1978**, 63, 1795-1800, DOI: 10.1121/1.381917

[24] Golabiazar, R.; Sadeghi, R. Salt-effects in aqueous surface-active ionic liquid 1-dodecyl-3-methylimidazolium bromide solutions: volumetric and compressibility property changes and critical aggregation concentration shifts. *J. Chem. Thermodyn.* **2014**, *76*, 29-44, DOI: https://doi.org/10.1016/j.jct.2014.03.001

[25] Vray, D.; Berchouz, D.; Delachartre, P.; Gimenez, G. Speed of sound in sulfuric acid solution: application to density measurement. IEEE. 1992 Ultrason. Symp. Proc., **1992**, 969-972, DOI: 10.1109/ULTSYM.1992.275835

[26] Kulig, W.; Agmon, N. Both zundel and eigen isomers contribute to the IR spectrum of the gas-phase $H_9O_4^+$ cluster. *J. Phys. Chem. B.* **2014**, *118*, 278-286, DOI: https://doi.org/10.1021/jp410446d

[27] Heinze, C.; Meyer, S.; Goris, N.; Anderson, L.; Steinfeldt, R.; Chang, N.; Le Quere, C.; Bakker, D. C. The ocean carbon sink–impacts, vulnerabilities and challenges. *Earth Syst. Dyn.* **2015**, *6*, 327-358, DOI: https://doi.org/10.5194/esd-6-327-2015

[28] Kohns, M.; Lazarou, G.; Kournopoulos, S.; Forte, E.; Perdomo, F. A.; Jackson, G.; Adjiman, C. S.; Galindo, A. Predictive models for the phase behaviour and solution properties of weak electrolytes: nitric, sulphuric, and carbonic acids. *Phys. Chem. Chem. Phys*. **2020**, *22*, 15248-15269, DOI: https://doi.org/10.1039/C9CP06795G

[29] Casas, J. M; Alvarez, F.; Cifuentes, L. Aqueous speciation of sulfuric acid–cupric sulfate solutions. *Chem.Eng. Sci.* **2000**, *55*, 6223-6234, DOI: https://doi.org/10.1016/S0009-2509(00)00421-8

[30] Knopf, D.; Luo, B.; Krieger, U.; Koop, T. Thermodynamic dissociation constant of the bisulfate ion from raman and ion interaction modeling studies of aqueous sulfuric acid at low temperatures. *J. Phys. Chem. A.* **2003**, *107*, 4322-4332, DOI: https://doi.org/10.1021/jp027775+

[31] Wang, X. B.; Nicholas, J. B.; Wang, L. S. Electronic instability of isolated SO_4^{2-} and its solvation stabilization. *J. Chem. Phys.* **2000**, *113*, 10837-10840, DOI: https://doi.org/10.1063/1.1333703

[32] Yacovitch, T. I.; Wende, T.; Jiang, L.; Heine, N.; Meijer, G.; Neumark, D. M.; Asmis, K. R. Infrared spectroscopy of hydrated bisulfate anion clusters: $HSO_4^-(H_2O)_{1-16}$. *The J. Phys. Chem. Lett.* **2011**, *2*, 2135-2140, DOI: https://doi.org/10.1021/jz200917f

[33] Chakraborty, S.; Jana, B. Ordered hydration layer mediated ice adsorption of a globular antifreeze protein: mechanistic insight. *Phys. Chem. Chem. Phys.* **2019**, *21*, 19298-19310, DOI: 10.1039/C9CP03135A

[34] Smolin, N.; Daggett, V. Formation of ice-like water structure on the surface of an antifreeze protein. *J. Phys. Chem. B.* **2008**, *112*, 6193-6202, DOI: https://doi.org/10.1021/jp710546e

[35] Yang, C.; Sharp, K. A. The mechanism of the type III antifreeze protein action: a computational study. *Biophys. Chem.* **2004**, *109*, 137-148, DOI: https://doi.org/10.1016/j.bpc.2003.10.024

[36] Volkov, A. G.; Paula, S.; Deamer, D. W. Two mechanisms of permeation of small neutral molecules and hydrated ions across phospholipid bilayers. *Bioelectrochem.Bioenerg.* **1997**, *42*, 153-160, DOI: https://doi.org/10.1016/S0302-4598(96)05097-0

[37] Zhong, C.; Deng, Y.; Hu, W.; Qiao, J.; Zhang, L.; Zhang, J. A review of electrolyte materials and compositions for electrochemical supercapacitors. *Chem. Soc. Rev.* **2015**, *44*, 7484-7539, DOI: 10.1039/C5CS00303B

[38] Nightingale Jr, E. Phenomenological theory of ion solvation. effective radii of hydrated ions. *J. Phys. Chem.* **1959**, *63*, 1381-1387, DOI: https://doi.org/10.1021/j150579a011

[39] Li, Y.; Zhang, C.; Jiang, Y.; Wang, T. J.; Wang, H. Effects of the hydration ratio on the electrosorption selectivity of ions during capacitive deionization. *Desalination.* **2016**, *399*, 171-177, DOI: https://doi.org/10.1016/j.desal.2016.09.011

[40] Jia, Z.; Wang, Y. Covalently crosslinked graphene oxide membranes by esterification reactions for ions separation. *J. Mate. Chem. A.* **2015**, *3*, 4405-4412, DOI: https://doi.org/10.1039/C4TA06193D

[41] Paul, S.; Choi, K. S.; Lee, D. J.; Sudhagar, P.; Kang, Y. S. Factors affecting the performance of supercapacitors assembled with polypyrrole/multi-walled carbon nanotube composite electrodes. *Electrochim. Acta.* **2012**, *78*, 649-655, DOI: https://doi.org/10.1016/j.electacta.2012.06.088

[42] Kiss, A. M.; Myles, T. D.; Grew, K. N.; Peracchio, A. A.; Nelson, G. J.; Chiu, W. K. Carbonate and bicarbonate ion transport in alkaline anion exchange membranes. *J. Electrochem. Soc.* **2013**, *160*, F994, DOI: 10.1149/2.037309jes

[43] Koshani, R.; van de Ven, T. G. M. Electroacoustic characterization of trimmed hairy nanocelluloses. *J. Colloid. Interface. Sci.* **2020**, *563*, 252-260, DOI: https://doi.org/10.1016/j.jcis.2019.12.034

[44] Dukhin, A. S.; Goetz, P. J. Characterization of liquids, dispersions, emulsions, and porous materials using ultrasound; *Elsevier*, Amsterdam. **2017**.

[45] Operating manual of dispersion technology instruments, acoustic and electroacoustic spectrometer DT-1202, Version 5.6.30. **July 2012**.

2. 8 Supporting information

Table S2. 1 Experimental changes in speed of sound for all salts at 23 ± 0.1°C, 1 atm

Molarity (M)	Δc ***(m/s)***	Molarity (M)	Δc ***(m/s)***	Molarity (M)	Δc ***(m/s)***
	Na_2CO_3		**Na_2SO_4**		**$MgSO_4$**
0.4000	62.9±0.6	0.4000	60.3±0.3	0.4000	50.1±0.2
0.3502	55.7±0.8	0.3500	52.1±0.5	0.3500	44.5±0.2
0.2996	47.6±0.3	0.3003	45.8±0.4	0.2995	38.3±0.2
0.2501	39.8±0.4	0.2502	39.1±0.3	0.2500	32.2±0.2
0.1995	31.9±0.6	0.2000	31.2±0.2	0.2000	25.9±0.1
0.1500	23.4±0.3	0.1500	22.3±0.2	0.1500	19.5±0.005
0.1000	15.6±0.1	0.1021	16.3±0.1	0.1001	13.2±0.1
0.0500	7.8±0.03	0.0500	8.1±0.003	0.0500	7.0±0.1
	NaOH		**KOH**		**NaCl**
0.4000	38.3±0.4	0.4000	34.1±0.2	0.4000	24.9±0.3
0.3750	35.9±0.3	0.3565	30.0±0.4	0.3422	20.8±0.2
0.3125	30.4±0.3	0.3119	25.9±0.1	0.2994	18.5±0.2
0.2500	24.5±0.01	0.2673	20.9±0.3	0.2566	15.5±0.1
0.2000	19.7±0.1	0.2228	16.9±0.2	0.2000	12.6±0.2
0.1002	9.3±0.1	0.1782	13.4±0.03	0.1711	9.7±0.3
0.0625	5.6±0.03	0.1337	9.6±0.02	0.1000	6.440.2
		0.0891	6.9±0.1	0.0500	3.2±0.3
	KCl		**LiCl**		**KBr**
0.4000	20.7±0.4	0.4000	20.5±0.1	0.4000	6.9±0.1
0.3700	19.1±0.1	0.3538	18.0±0.3	0.3500	6.6±0.2
0.3004	16.2±0.3	0.2948	15.7±0.1	0.3000	5.3±0.3

0.2683	13.8±0.2	0.2359	12.3±0.22	0.2501	4.6±0.2
0.2012	11.0±0.3	0.1769	9.3±0.1	0.2005	3.7±0.2
0.1341	6.9±0.2	0.1179	5.9±0.2	0.1500	2.6±0.1
0.0671	3.8±0.1	0.0590	2.7±0.04	0.0999	1.7±0.1
0.0335	1.±0.1				
	HCl		**NaI**		**K_2CO_3**
0.4000	4.9±0.03	0.4000	-2.4±0.1	0.4000	60.3±0.1
0.2999	3.8±0.02	0.3501	-2.2±0.1	0.3500	52.8±0.1
0.1999	2.5±0.01	0.3000	-2.0±0.2	0.3002	45.7±0.2
0.1000	1.3±0.01	0.2500	-1.6±0.2	0.2500	37.4±0.1
		0.2001	-1.4±0.2	0.2001	30.5±0.1
		0.1502	-1.1±0.1	0.1500	22.8±0.2
		0.1000	-0.8±0.1	0.0999	15.4±0.1
				0.0500	8.2±0.2
	K_2SO_4		**$MgCl_2$**		**LiOH**
0.4000	51.9±0.2	0.4000	44.2±0.2	0.4000	33.9±0.2
0.3500	45.5±0.2	0.3501	37.4±0.01	0.3131	25.8±0.02
0.3001	40.2±0.4	0.2500	25.9±0.1	0.2088	17.4±0.2
0.2499	32.8±0.03	0.2000	21.7±0.01	0.1044	9.1±0.3
0.2000	26.0±0.3	0.0500	5.2±0.05		
0.1500	19.2±0.2				
0.0998	14.0±0.04				
0.0500	7.1±0.1				
	NaBr		**KI**		**H_2SO_4**
0.4000	11.1±0.1	0.4000	-6.4±0.1	0.4000	-4.2±0.4
0.3500	9.6±0.1	0.3500	-5.4±0.3	0.2000	-3.2±0.2

0.3002	8.3±0.1	0.3001	-4.7±0.2
0.2501	6.9±0.3	0.2500	-3.8±0.2
0.2000	5.3±0.3	0.1999	-3.2±0.02
0.1500	4.2±0.1	0.1500	-2.4±0.2
0.1002	2.8±0.2	0.1000	-1.5±0.03
		0.0491	-0.8±0.003

Table S2.2 Theoretical change in speed of sound in m/s for six salts

Molarity (M)	K_2CO_3	K_2SO_4	$MgCl_2$	LiOH	NaBr	KI
0.01	1.364	1.300	0.989	0.848	0.278	-0.164
0.02	2.729	2.600	1.977	1.697	0.556	-0.328
0.03	4.093	3.900	2.966	2.545	0.830	-0.492
0.04	5.458	5.200	3.954	3.394	1.110	-0.656
0.05	6.822	6.499	4.943	4.242	1.389	-0.820
0.06	8.186	7.799	5.930	5.091	1.667	-0.984
0.07	9.551	9.099	6.920	5.939	1.944	-1.148
0.08	10.915	10.399	7.908	6.788	2.222	-1.312
0.09	12.280	11.699	8.897	7.636	2.500	-1.475
0.1	13.644	12.999	9.885	8.485	2.778	-1.639
0.11	15.008	14.299	10.874	9.333	3.056	-1.803
0.12	16.373	15.599	11.86	10.181	3.333	-1.967
0.13	17.737	16.890	12.851	11.030	3.610	-2.131
0.14	19.102	18.199	13.839	11.879	3.889	-2.295
0.15	20.466	19.498	14.828	12.727	4.167	-2.459
0.16	21.830	20.798	15.816	13.576	4.445	-2.623
0.17	23.194	22.098	16.805	14.424	4.722	-2.787
0.18	24.559	23.398	17.79	15.273	5.000	-2.95
0.19	25.923	24.698	18.782	16.121	5.278	-3.115
0.2	27.288	25.998	19.770	16.970	5.556	-3.279
0.21	28.652	27.298	20.759	17.818	5.833	-3.443
0.22	30.016	28.598	21.747	18.667	6.111	-3.607
0.23	31.381	29.898	22.736	19.515	6.389	-3.771
0.24	32.745	31.197	23.724	20.364	6.667	-3.935

0.25	34.110	32.497	24.713	21.212	6.945	-4.098
0.26	35.474	33.797	25.701	22.061	7.222	-4.262
0.27	36.839	35.097	26.689	22.909	7.500	-4.426
0.28	38.203	36.397	27.678	23.758	7.780	-4.590
0.29	39.567	37.697	28.667	24.606	8.056	-4.754
0.3	40.932	38.997	29.660	25.455	8.333	-4.918
0.31	42.296	40.297	30.644	26.303	8.611	-5.082
0.32	43.661	41.597	31.632	27.152	8.889	-5.246
0.33	45.025	42.896	32.621	28.000	9.167	-5.410
0.34	46.389	44.196	33.610	28.849	9.440	-5.574
0.35	47.754	45.496	34.598	29.697	9.722	-5.738
0.36	49.118	46.796	35.587	30.546	10.000	-5.902
0.37	50.483	48.096	36.575	31.394	10.278	-6.066
0.38	51.847	49.396	37.564	32.243	10.556	-6.230
0.39	53.211	50.696	38.552	33.091	10.834	-6.393
0.4	54.576	51.996	39.541	33.940	11.111	-6.558

Preface to Chapter 3

In the previous chapter, we investigated how ions present in the dope affect the speed of sound. Since CMF dope is composed of polymers, particles, and salts, the next logical step is to examine the contribution of the cellulose components to sound speed. Understanding the impact of salts on sound speed is of great importance to obtain a deeper understanding of the interactions within cellulose-based systems. This insight could significantly improve the application of acoustics as a powerful tool for characterizing these materials. However, using the equations for salts to CMF dope or other cellulose materials directly has remained rather difficult. This difficulty arises from the complex structure of cellulose, which contains numerous hydroxyl and highly charged carboxyl groups. These interactions require a more sophisticated equation to accurately model the behavior.

Moreover, preparing the dope is a critical first step in the continuous production of cellulose films. The subsequent step in fabricating cellulose films involves extruding the dope through a slit into an acid bath, which induces the resolidification of cellulose into a film. In Chapter 3, we introduce a continuous production method for CMF films and explore how variations in jet-to-wire velocity impact the mechanical properties of the resulting films.

Chapter 3

Continuous production of resolidified cellulose-based film

3. 1 Abstract

Films commonly used in food packaging are often derived from petroleum-based plastics, which pose a threat to the environment due to them being non-biodegradable and non-ecological. Herein, we present an approach wherein robust and flexible cellulose-based films were continuously generated using a flow casting method, involving the extrusion of dope through a slit followed by resolidification in acid. The extruded films were deposited on a conveyor belt submerged in the acid bath, capable of operating at speeds up to 7 cm/s. The morphological and physiochemical properties of films were assessed using field emission scanning electron microscopy (FE-SEM), solid-state ^{13}C NMR, and X-ray diffraction (XRD). XRD analysis revealed that carboxymethylated cellulose films (CCF) regenerated at higher extrusion speeds exhibited higher alignment in the orientation of cellulose crystals. The tensile stress of the film increased from 105 to 125 MPa as the speed of the conveyor belt increased from 0.8 to 7 cm/s. Notably, the tensile strength in the belt direction (BD) (125 MPa) is significantly higher (125 MPa) than the tensile stress in the cross direction (CD) (76 MPa). This difference confirms that the anisotropic nature of the films, with cellulose chains preferentially aligning along the BD, as well do the specific crystallographic planes $(1\bar{1}0)$ and (110).

Keywords: carboxymethylated cellulose film; continuous production: crystal orientation

3. 1. 1 Table of Contents

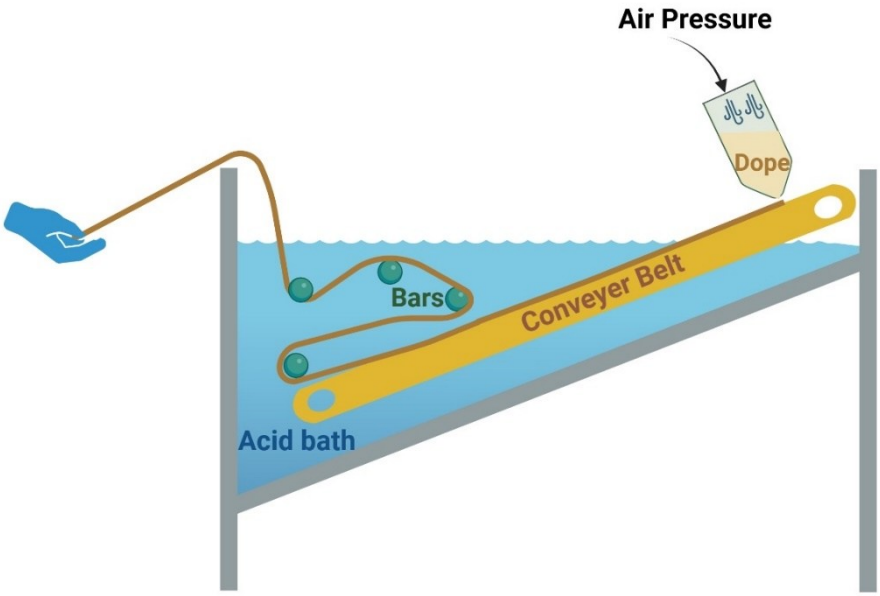

3. 2. Introduction

Plastic waste is of increasing global concern due to a drastic increase in plastic debris in the oceans, terrestrial environments, and on coastlines [1]. This is primarily due to the extensive use of plastic, which offers numerous advantages, including affordability, adaptability, lightweight, and resistance to the external environment [2]. Industries, particularly the packaging industries, heavily rely on plastics for packaging food, beverages, pharmaceuticals, and chemicals, thereby contributing substantially to global plastic waste accumulation [3]. The inherent non-biodegradability of most plastic products exacerbates this challenge, facilitating their widespread proliferation and persistence in the environment. Consequently, researchers are ardently looking for eco-friendly alternatives to plastic to mitigate its detrimental impact on ecosystems.

Cellulose is extensively acknowledged as the predominant terrestrial source, revered for its exceptional biodegradability, biocompatibility, and sustainability [4]. The cellulose-based film offers numerous benefits including affordability, remarkable mechanical resilience, non-toxicity, and resistance to degradation. These exceptional qualities position cellulose-based films as promising substitutes for diverse applications ranging from packaging material, separation membranes [5] absorbents for dye removal [6], electronic devices [7], and water purification systems [8, 9].

Numerous methods to produce cellulose-based films that emulate the properties of conventional plastics have been developed. The oldest method is the production of cellophane, which was the dominant transparent packaging material before the ascent of plastics [10]. It is made by reacting cellulose with carbon disulfide (CS_2) in an alkaline solution, producing cellulose xanthate, which

is regenerated into cellulose when placed in an acid bath. However, during the regeneration process, the release of CS_2, a highly toxic substance, occurs.

Cellulose functionalized with a variety of side groups bestows cellulose with outstanding properties such as water insolubility, low water permeability, oxygen barrier properties, and antibacterial activity, rendering it suitable for different applications [11]. For example, cellulose derivatives including cellulose carbamate [12, 13], cellulose acetate [14], esterified cellulose [15, 16], carboxymethylcellulose [17, 18] and methylcellulose [19] have been explored extensively. Moreover, coated cellulose-based films [20] have been extensively investigated for their potential applications.

However, the majority of regeneration of cellulose-based film involves either toxic procedures or the dissolution of cellulose typically necessitates the incorporation of solvents that pose environmental hazards, coupled with intricate processing methods. For example, the dissolution of cellulose usually involves binary solvent systems comprising organic solvents or ionic liquids such as sodium hydroxide/urea [21], butyl-3-methylimidazolium chloride/dimethylsulfoxide (DMSO) [22] or 1-ethyl-3-methylimidazolium acetate/DMSO [23]. Pang et al. [24] prepared regenerated cellulose film by dissolving cellulose from different sources in 1-ethyl-3-methylimidazolium acetate (EmimAc) at 80 ^{o}C followed by regeneration in water. Their investigation revealed that cellulose derived from pine possesses the highest tensile strength among various cellulose sources while cotton cellulose exhibits superior thermal stability, surpassing those prepared from other resources. In the study of Zheng et al., [25] the impact of the ionic liquid on the physical properties of the cellulose was investigated. They discovered that films regenerated from 1-Allyl-3-methylimidazolium chloride [Amim][Cl] liquids exhibit a higher

tensile strength than those regenerated from other ionic liquids. However, the time and energy-consuming process significantly restricts the widespread application of such a cellulose film.

Previous research from our lab produced carboxymethylcellulose films (CCF) from pulp that had undergone a mild carboxymethylation [26, 27]. Subsequently, a flow casting technique was used to resolidify CCF by submerging dissolved carboxymethylcellulose (CMF) into an acid bath [26]. For the cellulose-based films, we prefer the term resolidification, rather than regeneration, because the carboxylated cellulose is first dissolved and subsequently resolidified. During resolidification, it does not change its chemical structure, in contrast to cellophane, which is formed by modifying cellulose in cellulose xanthate, which is regenerated in cellulose in an acid bath. In the resolidification of carboxylated cellulose, no chemical reaction occurs in the acid bath other than the neutralization of alkaline by acid. The flow casting technique yielded small, non-continuous individual films with promising tensile strength and transparency for potential applications in the food packaging industry [26, 27]. The films can also be regenerated from different coagulation baths such as an HCl and HNO_3 bath. The porosity and tensile strength properties of the CMF film generated from different bath have been characterized and discussed [27].

However, this production method for cellulose films only allows for limited film production which may encounter lots of challenges for scale-up to industrial operations. Transitioning to continuous flow casting to produce cellulose films offers notable advantages over conventional methods. By integrating principles of green chemistry and green engineering, this approach presents several benefits, including cost-effectiveness, reduced equipment size, lower energy consumption, minimized waste generation, enhanced safety measures, improved manufacturing efficiency, and superior product quality.

Producing a continuous film enables large-scale production and quality improvement as the resolidification conditions can be precisely controlled. Our primary objective is to establish a continuous process for producing flexible and strong cellulose film that is commercially viable on an industry-wide scale.

Here, we present a prototype apparatus designed for the continuous resolidification of cellulose films. This device comprises a dope reservoir and a conveyor belt, with the lower portion of the belt submerged in an acid bath. The dope in the reservoir is slowly extruded through a narrow slit onto the belt, immersed in a sulfuric acid bath allowing the film to form. This process generates one long, continuous, and seamlessly smooth film. In this study, three different conveyor belt speeds were applied, and the alignment of cellulose chains on both BD and CB is discussed. Additionally, we analyze the chemical structure, XRD results, water resistance, roughness, and mechanical properties of the produced continuous films.

3. 3 Experimental Section

3. 3. 1 Materials

Unrefined, bleached softwood kraft pulp (FPInnovations, Canada) was ground using a GlenMills SM300 (Clifton, NJ, USA). Reagent-grade sodium chloroacetate (MCA), sodium hydroxide (NaOH), sulfuric acid (H_2SO_4), and ethanol were purchased from Sigma-Aldrich (Oakville, ON, Canada) and were used as received. Cellophane was purchased from Thermo Fisher Scientific.

3. 3. 2 Carboxymethylation of cellulose

The pulp was screened once by 0.5 mm, followed by 0.25 mm sieves. The carboxymethylation reaction was performed in a continuously stirred chemical reactor (Figure 3. 2) generating a carboxyl charge density of 1.8 mmol/g (DS~ 0.3). 1 kg of the milled pulp was put into the reactor, followed by the addition of 10 L of isopropyl alcohol and 650g 50wt% sodium hydroxide solution (Figure 3. 2a). The reaction first took place in a 50℃ water bath for an hour. Then the reaction temperature was increased to 60 ℃, and 687g 40wt% sodium chloroacetate was added and left to react for 2 hours. After 2 hours, the solvent was released through the outlet at the bottom of the reactor and the product CMF 1.8 (carboxymethylated fibers with a carboxyl content of 1.8 mmol/g)) remained in the reactor. 4 L of 70% ethanol was added to the reactor and stirred for 20 minutes to remove the unreacted salts. The precipitated cellulose was collected, dried, and stored in room temperature for future use, while the dissolved unreacted salts remained in the solution. CMF 1.0 (DS~0.17), CMF 1.5 (DS~0.25), and CMF 2.5 (DS~0.41) were made by adding sodium hydroxide solution and sodium chloroacetate solution proportionally.

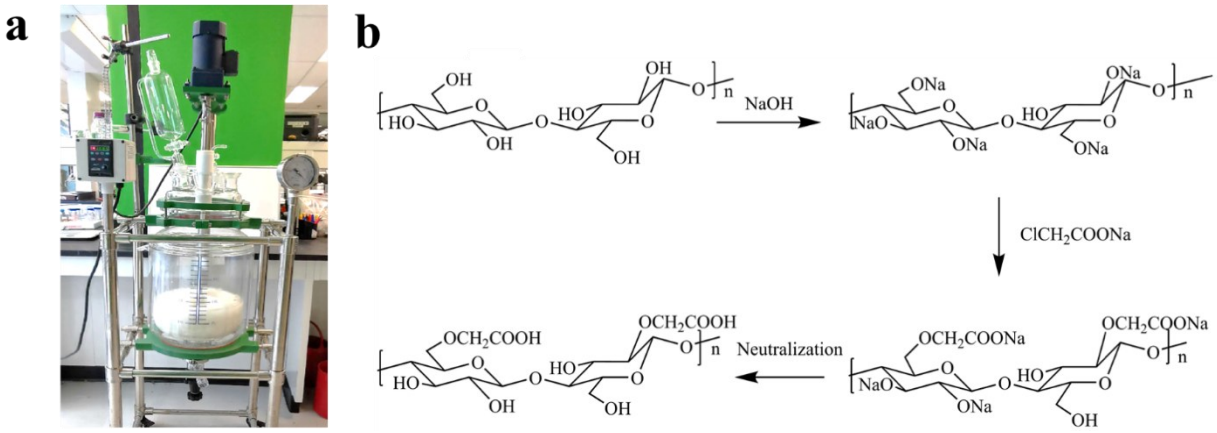

Figure 3. 2 (a) Chemical reactor in which the carboxymethylation of CMF occurs (top b). This reaction is followed by dissolution in an aqueous alkaline solution, and subsequent resolidification in an acid bath.

3. 3. 3. Preparation of viscous dope

Viscous dope is prepared by adding 5% sulfuric acid solution to CMF, followed by a 50 wt.% NaOH solution. To be more detailed, 900 g 5 wt.% sulfuric acid was added to 150 g CMF. Bubbles were observed upon the addition of sulfuric acid, attributed to the partial decarboxylation of carboxymethyl groups [28]. The mixture was allowed to react for approximately 10 minutes. Subsequently, 300 g 50 wt% solution of sodium hydroxide was introduced while stirring vigorously, resulting in the formation of a transparent suspension. Finally, 150 g water was added while stirring. The dope is stored at room temperature for future use.

3. 3. 4. Film preparation with the use of a conveyor belt

As Figure 3. 3a indicates, the flow casting set-up consists of a tank, a feeder, a conveyor belt, and several metallic bars. Within the tank, four bars were mounted and about 20 L of 10% sulfuric acid

was introduced. The viscous dope was then loaded into the feeder. After air pressure was applied to the feeder, the homogeneous viscous dope was extruded through the exit slit (width 1 mm) of the feeder on the belt (Figure 3. 3b). The speed of the belt can be adjusted with a maximum capacity of 7 cm/s. To maintain a consistent thickness of the film, increased air pressure was applied with a higher speed of the conveyor belt. For the speeds of 0.8, 4.5, and 7 cm/s, air pressure of ~ 150, 310, and 470 kPa were applied, respectively. Following the extrusion process, it was immersed in the acid bath and was kept in the acid bath longer by winding the film along the metallic bars to reach complete regeneration (as indicated by the graphic abstract). For films produced at conveyor belt speeds of 4.5 cm/s and 7 cm/s, we temporarily stopped the conveyor belt and the films were left in the acid bath for at least 2 minutes after reaching the end of the belt, to allow sufficient time for resolidification. In industrial applications, it is necessary to employ a longer tank and an extended conveyor belt to ensure that the films have sufficient time to fully resolidify. Figure 3. 3c shows the regenerated film being withdrawn from the acid bath, followed by being suspended in the air for drying overnight. The dried film is shown in Figure 3. 4. A supplementary video has been prepared to elucidate the operation of the conveyor belt, the link to which is shown in the supplemental information.

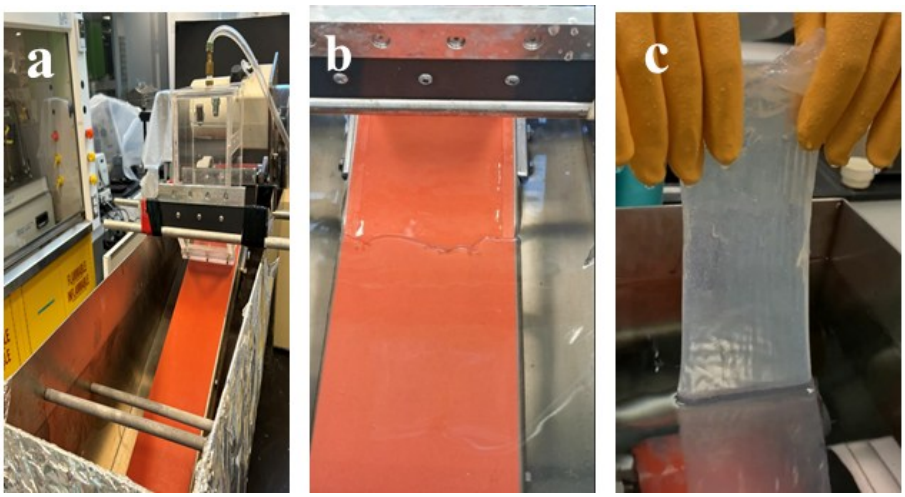

Figure 3. 3 (a) Conveyor belt and feeder; (b) Dope extruded onto the belt; (c) Resolidification of CMF into a film.

3. 3. 5 Structural characterization

3. 3. 5. 1. Carboxyl charge density and porosity calculation

Following the procedure by Yang *et al.*,[29] conductometric titrations were carried out using a Metrohm 836 Titrando apparatus to ascertain the number of carboxyl groups. Briefly, 100 mL of distilled water and 50 mg of the dry material were well mixed before 1 M HCl was added to bring the pH level to 3.5. 45 mL of a 10 mM NaOH solution was then gradually added to the sample mixture for a few hours. The graph of conductance vs increased NaOH volume was used to determine the carboxyl content.

The porosity of the film is calculated by the following equation:

$$Porosity\ (\%) = (1 - \frac{\rho_s}{\rho_{cell}}) \times 100 \quad (1)$$

Here ρ_{Cell} is the density of cellulose, and ρ_S is the density of the cellulose sample (1.5 g/cm^3).

3. 3. 5. 2. Fourier transform infrared (FTIR) spectroscopy and X-ray diffraction (XRD)

A PerkinElmer spectrometer equipped with a single bounce diamond attenuated total reflectance (ATR) accessory was used to gather FTIR spectra to ascertain the surface chemical characteristics of CCF. Dry samples were put on the ATR crystal, and then the pressure clamp's tip was lowered until the samples were subjected to the required pressure. The study was performed for wave numbers ranging from 400 to 4000 cm^{-1}.

The XRD spectra of the kraft pulp, CMF, and CCF were gathered on a Bruker Discover D8 diffractometer equipped with a 2D VANTEC-500 area detector, using a fixed time mode with a step interval of 0.005° and Copper Kα radiation (1. 54 Å) at 35 kV and 45 mA, the 2θ range was from 5 to 55°.

The crystallinity index (CI) of the pulp, CMF, and CCF was calculated by the following equation [30]:

$$CI\ (\%) = \left(\frac{I_{cry} - I_{am}}{I_{cry}}\right) \times 100 \qquad (2)$$

where I_{cry} is the intensity of the cellulose crystalline peak at 22.5° for cellulose I (pulp) and 21.6° for cellulose II (CMF and CCF) respectively. I_{AM} is the minimum intensity in the amorphous region, which is between the two major peaks at 11° and 21°.

3. 3. 5. 3. Solid-state ^{13}C NMR spectroscopy

A solid-state A Varian/Agilent VNMRS-400 Wide-bore spectrometer operating at a frequency of 100.5 MHz was used to collect ^{13}C NMR spectra. A 4 mm rotor was filled with film strips that were 2-3 mm wide and 2 cm long, and it was then spun at 10 kHz. The DS of the CCF equals the ratio of the integral of NMR peaks at around 170-180 ppm to the peaks at 100 to 110 ppm [31].

3. 3. 5. 4. Film Tensile Strength

An Instron Mini 44 tensile tester with a 500 N load cell was used to measure the mechanical strength of the films in an ambient environment. The experiments were conducted using film strips that were 5 mm broad and 30 mm long, stretching them at a rate of 5 mm per minute. For each sample, the average number was determined after at least five measurements.

3. 3. 5. 5. Water Vapor Permeation (WVP)

The water vapor permeation is assessed according to the method ASTM-E96/E96-05 [32]. 20 g of DI water was put into a Petri dish. There is at least 1 cm between the top of the dish and the surface of the water. The films were attached to the dish top using a water-resistant sealant. Weights were assessed 24 hours after Petri plates had been conditioned at 25 °C and 75% RH in a container with stable humidity. WVP was calculated by the following formula:

$$WVP = (g\ m^{-1}s^{-1}Pa^{-1}) = (\frac{w}{t}) \times d \times A^{-1} \times \Delta p^{-1} \quad (3)$$

where w is the weight loss of water (g), t is time (s), d is the film thickness (m), A is the film area (m^2), and Δp is the vapor pressure difference (3167.2 Pa, at 25 °C). The water vapor transmission rate (WVTR) is determined by:

$$WVTR(g\ m^{-2}day^{-1}) = (\frac{w}{t}) \times A^{-1} \quad (4)$$

where w is the weight loss of water (g), t is time (day), A is the film area (m^2)

3. 3. 5. 6. Field-emission scanning electron microscopy (FE-SEM)

The morphology of the films was characterized by a High-resolution FEI Quanta 450 environmental scanning electron microscope (FE-ESEM) with EDAX Octane Super 60 mm2 SDD.

The samples were prepared by coating about 5 nm with Platinum and the images were taken at an accelerating voltage of 10 kV.

3. 3. 5. 7. Atomic Force Microscopy (AFM)

The surface morphology of films was observed by atomic force microscopy (AFM) with a Cypher-S scanning probe atomic force microscope (Asylum Research, UK). Samples were air-dried overnight. To prepare the AFM sample, a freshly cleaved mica was attached to a magnetic disc. The dried films were directly attached to the surface of the mica using glue. The experiments were conducted in a height retrace mode with a silicon tip with a force constant of 42 N/m, resonance frequency of 320 kHz, and a scan size of 2 radius μm.

3. 4 Results and discussion

The dried pulp used contained about 5% moisture. The pulp composition includes 12.3% hemicellulose and 0.14% lignin [33]. Carboxymethylation of cellulose results in the formation of cellulose microfibrils, cellulose nanocrystals, and soluble carboxylated polymers. Additionally, We identified the presence of microspheres and nanorods in the dope [33]. The final concentration of sulfate ion and sodium ion in the dope were 0.3 mol/L and 2.5 mol/L, respectively, and the pH of the dope was approximately 13. It should be noted that all sodium and sulfate ions in the dope are removed and washed out afterwards in the acid bath and neutralization stages, leaving no peak in FTIR spectra of films.

The carboxyl group density in CCF was quantified to be 2.5, 1.8, and 1.0 mmol/g by conductometric titration, corresponding to a degree of substitution DS ~0.42, 0.3, and 0.17,

respectively. Photographic images of CCF with carboxyl contents of 2.5 mmol/g and 1.8 mmol/g are shown in Figure 3. 4.

The transparency of films increased with higher charge densities, which is because there are more dissolved polymers and fewer nanocellulose particles within CCF with a higher charge density. The nanoparticles scatter more light than dissolved polymers, thus increasing the turbidity of the film. Higher turbidity is primarily attributed to the pore-air interface caused by undissolved fiber fragments [26, 27].

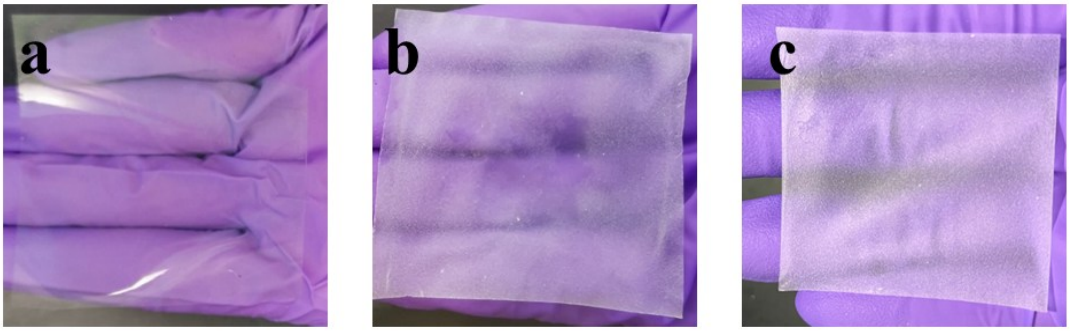

Figure 3. 4 Photographs of CMF films with carboxyl contents of (a) 2.5 mmol/g; (b) 1.8 mmol/g; (c) 1.0 mmol/g

FE-SEM imaging has been performed to evaluate the smoothness of CCF (Figure 3. 5 a,b) and cellophane (Figure 3. 5 d,e). They both exhibited rather smooth surfaces. The thickness of CCF is measured to be about 53 µm, a dimension commensurate with that of the cellophane employed for comparative analysis. The morphology of the films was examined by AFM as depicted in Figures 3. 5c and 3. 5f. The images indicate smooth surfaces for both films which is in agreement with FE-SEM results. Quantitative Analysis of surface roughness via root mean square (RMS)

measurements unveiled subtle discrepancies between the two materials. CCF exhibited an RMS of 5.1 nm, marginally higher than that of cellophane film (RMS roughness = 3.5 nm). This disparity suggests that CCF possesses a slightly rougher texture compared to cellophane.

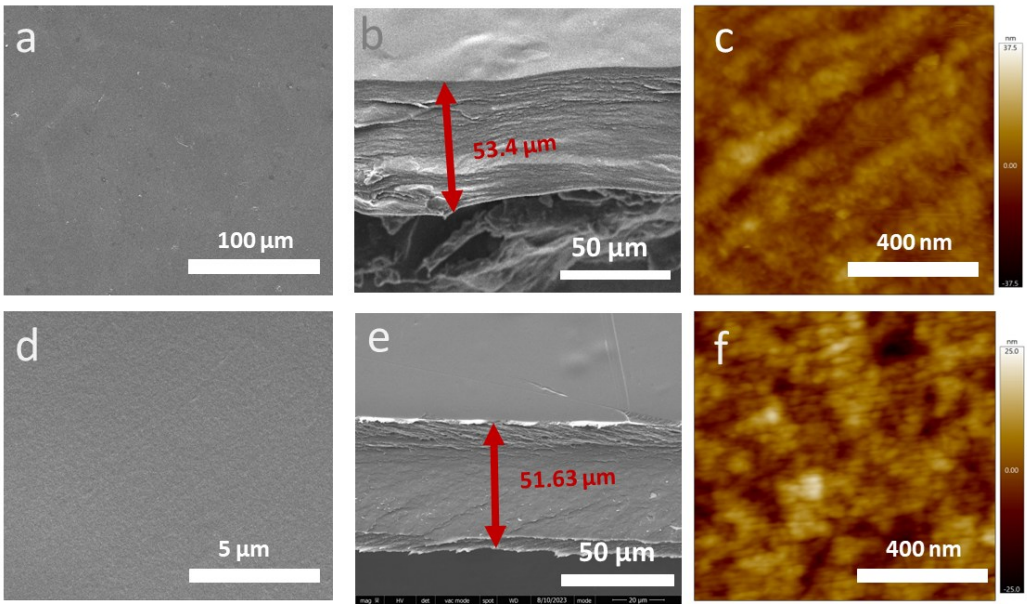

Figure 3. 5 (a) FE-SEM images of CCF with scale bar of 100 µm; (b) cross-section image of CCF with scale bar of 20 µm; (c) AFM image of CCF with scale bar of 400 nm; (DS of CCF~0.3) (d) FE-SEM images of cellophane film with scale bar of 5 µm; (e) cross-section image of cellophane with scale bar of 20 µm; (f) AFM image of cellophane film with scale bar of 400 nm

FTIR was employed to analyze the chemical structure of CCF. Figure 3. 6 displays the FTIR of kraft pulp, CMF, and CCF. In all three spectra, bands at 1057 cm^{-1} and 897 cm^{-1} corresponds to –C–O–C pyranose ring skeletal vibration and β-glycosidic linkages, respectively.[34] The wide bands observed at 3330 and 2890 cm^{-1} are attributed to O-H stretching and C-H stretching vibrations, respectively. Notably, a distinct vibration at 1600 cm^{-1} is observed in the CCF spectrum but absent in pulp, indicative of the presence of -COONa, confirming the success of the carboxymethylation

reaction [35]. This peak shifts to 1730 cm^{-1} for CCF, which is because of the protonation of -COONa to -COOH in the acid bath.

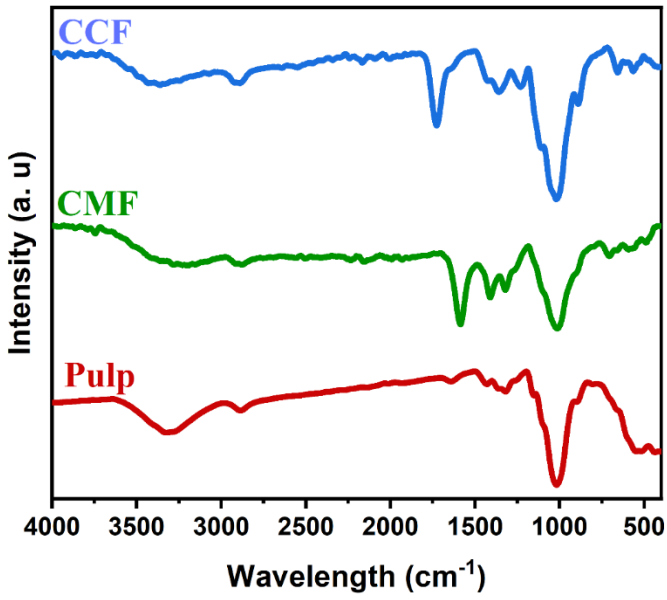

Figure 3. 6 FTIR spectra of cellulosic pulp, CMF, and CCF with carboxyl group density of 1.8 mmol/g

The XRD Spectrum of Kraft pulp, CMF and CCF are depicted in Figure 3. 7. Notably, the peaks observed at 2θ angles of 15.2°, 16.9°, 22.6°, and 34.8° in the XRD pattern of the kraft pulp correspond to the overlapping $(1\bar{1}0)$ and (110) planes, to (200) and to (004) planes, respectively, indicative of the characteristic cellulose I structure [36]. The crystallinity index (CI) of the kraft pulp is determined to be 78.5%. After carboxymethylation and resolidification, the distinct peaks at about 11.2° and 20° are attributed to the merged $(1\bar{1}0)$ planes and the overlapping of (110) and (020) planes of cellulose II, respectively [37]. After carboxymethylation, the crystallinity index of CMF decreased to 36.2%, respectively, consistent with findings by Lin *et al* [38].

As shown in Figure 3. 7, the mercerization and carboxylation help the dissolution of cellulose fiber and the transformation of cellulose from cellulose I to cellulose II. The decrease in crystallinity of CMF and CCF compared to the original pulp is attributed to the dissolution of carboxymethylated crystals in the dope. Figure 3. 7 also illustrates the XRD profiles of CCF resolidified at three distinct speeds of the conveyor belt. The intensity of peak for the $(1\bar{1}0)$ plane at 11.2° for CCF solidified at different speeds is considerably increased, possibly because of the improved orientation of the cellulose molecules during solidification resulting in a quasi-crystalline structure of aligned cellulose molecules. In contrast, the intensity of the overlapping crystalline (110) and (020) planes is hardly affected, implying they are not affected by flow alignment. The CI of CCF, as calculated from eq. 2 at conveyor belt speeds of 7 cm/s, 4.5 cm/s, and 0.8 cm/s is found to be 34.7%, 26.3%, and 20.0%, respectively, showing an increasing trend with the higher speed of the conveyor belt. The Crystallinity Index values are only approximate, as no theoretical XRD spectra for CMF are available.

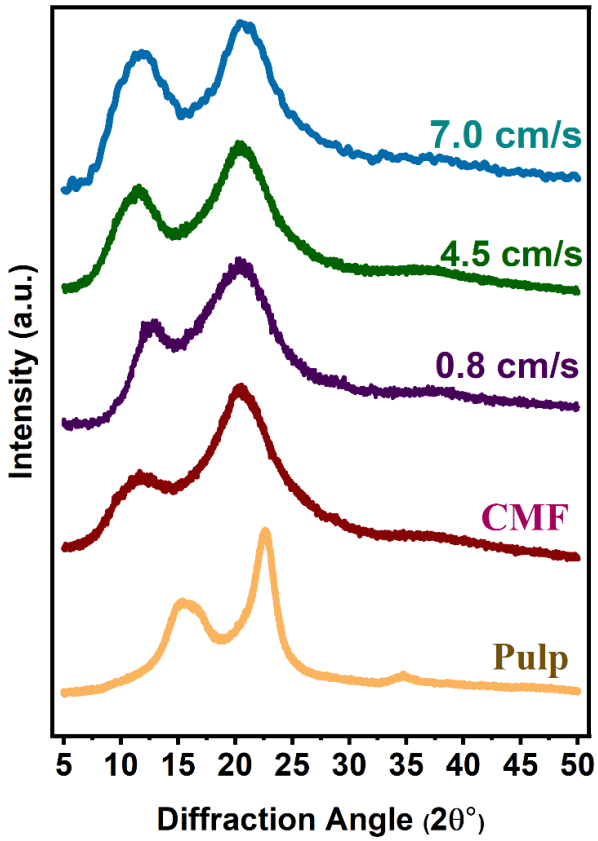

Figure 3. 7 XRD spectra of cellulosic pulp, CMF and CCF with carboxyl group density of 1.8 mmol/g resolidified with conveyor belt speeds of 7, 4.5 and 0.8 cm/s

Solid-state ^{13} CNMR spectroscopy serves as a valuable tool for elucidating the functional groups within cellulose-based materials. In Figure 3. 8, the solid-state ^{13}C NMR results for CMF and CCF with a carboxyl group density of 1.8 mmol/g are presented. Notably, all characteristic peaks associated with the cellulose pyranose ring are observed between 60 and 110 ppm, encompassing signals at 105 ppm (C1), 70-90 ppm (C2-C5), and 65 ppm (C6) [39].

Furthermore, the peak at approximately 178 ppm corresponds to carbonyl groups in the sodium form in CMF, which shifts to 173 ppm following the protonation of carbonyl groups. Figure 3. 8 also illustrates the solid-state ^{13}C NMR outcomes for CMF samples with varying charge densities,

specifically 1, 1.8, 2.5, and 3 mmol/g. The pH of 2 (wt) % CMF 3, CMF 2.5, CMF 1.8, and CMF 1.0 is measured to be 10.1, 9.8, 9.6, and 8.9, respectively. The DS is calculated to be 0.58, 0.39, 0.28, and 0.16 mmol/g for CMF 3, CMF 2.5, CMF 1.8 and CMF 1.0, respectively.

In the spectra of CMF 3, CMF 2.5, and CMF 1.8, peaks at 83.8 and 65 ppm are assigned to C4 and C6, respectively. However, new peaks around 89.2 and 65.5 ppm emerge in the NMR of CMF 1.0. This is because peaks around 89.2 and 83.7 ppm represent C4 crystalline and amorphous regions, respectively. Peaks around 65.5 and 63.2 ppm represent C6 crystalline and amorphous regions, respectively [40]. Interestingly, the peaks for the crystalline region for C4 and C6 are much more prominent in the NMR of CMF 1.0 compared to other CMFs. This observation is attributed to the lower DS (~0.16) in CMF, resulting in only a small portion of -COOH being substituted on C6 in cellulose, thus fewer dissolved cellulose polymers. Conversely, higher DS values lead to overlap between peaks corresponding to the crystalline region and amorphous region, indicating that more dissolved cellulose polymers were separated from the crystals. These results are consistent with the photographic images of CMF 2.5 and 1.8 (Figure 3. 4).

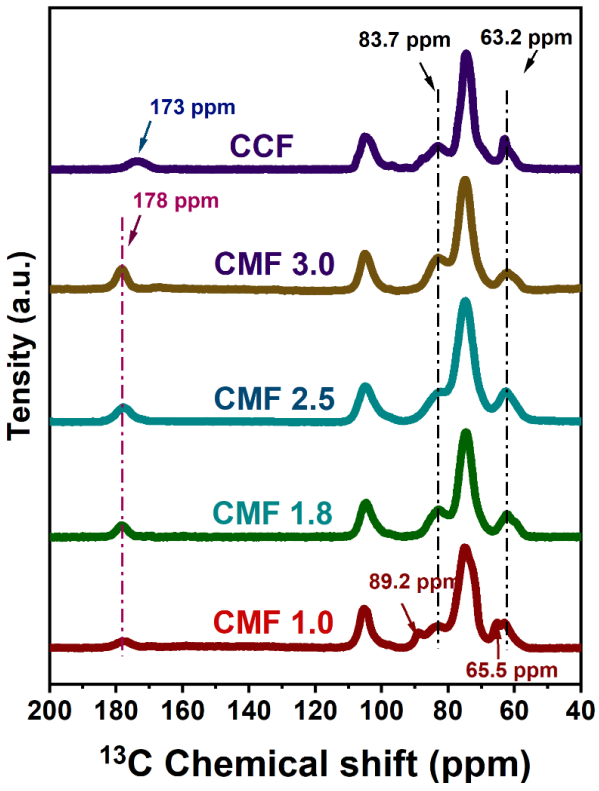

Figure 3. 8 (a) ^{13}C NMR spectra of CMF and CCF with carboxyl content of 1.8 mmol/g; b NMR spectra of CMF with carboxyl content of 1, 1.8, 2.5, and 3 mmol/g

Figure 3. 9 shows the mechanical properties of CCF regenerated with different conveyor belt speeds. With the increasing speed of the conveyor belt from 0.8 cm/s to 7 cm/s, the tensile stress rises from 105 to 125 MPa, accompanied by an increase in Young's modulus from 4.25 to about 5 GPa. However, the tensile strain decreases by approximately 1%. The process of flow casting engenders the formation of anisotropic films, wherein the alignment of constituents is influenced by the extrusion from the slit. Notably, with higher conveyor belt speeds, the films exhibit heightened anisotropy, culminating in augmented tensile stress and Young's modulus, particularly in the belt direction. These findings substantiate the observations made by Zheng et al., who reported a direct relationship between enhanced mechanical strength and heightened crystallinity.[25]

Figure 3. 9 represents the mechanical properties of CCF in belt direction (BD) and cross direction (CD). There is a dramatic difference between CCF tested in BD and CD. Tensile stress at maximum load decreases from 125 to 76 MPa, and tensile strain at maximum load decreases from 4.28 to 1.5 %, even though there is a slight increase in Young's modulus. CCF tested in BD exhibits much exceptional mechanical properties than tested in CD, which is because the crystal aligns with the direction of the conveyor belt (BD). In the BD, aligned chains result in higher tensile strength, because the force to break chains or pull them out of the matrix is larger than the force required to break the bonds between aligned chains, which happens in the cross direction. Due to similar underlying factors, paper also exhibits greater strength in the machine direction compared to the cross direction [41]. In papermaking, the jet-to-wire velocity has been reported to be approximately 1 [42]. In the resolidification of CCF, the jet-to-conveyor belt speed ratios were calculated as 0.31, 0.24, and 0.21 for conveyor belt speeds of 0.8 cm/s, 4.5 cm/s, and 7 cm/s, respectively. This indicates that the dope undergoes elongation as it moves over the conveyor belt, with greater stretching observed at higher conveyor belt speeds.

We expect that the cellulose chains are preferably oriented parallel to the conveyor belt direction, as are the $(1\bar{1}0)$, (110) and (020) crystalline planes. These results indicate that the improved mechanical properties of CCF with higher speed can be attributed to the better crystal orientation and arrangement, which corroborates with the XRD results.

Table 3. 1 summarizes the mechanical properties of conventional films utilized in the packaging industry. The data indicate that the tensile strength of CCF (BD) surpasses that of low density polyethylene (LDPE), high density polyethylene (HDPE), polypropylene (PP), polystyrene (PS) and cellophane, and is comparable to polyvinyl alcohol (PVA). In terms of tensile strain, CCF

(BD) demonstrates greater values than bacterial cellulose and is competitive with PS, although it is lower compared to other polymeric plastics. Additionally, CCF (BD) exhibits a high Young's modulus, yet it is lower than that of bacterial cellulose.

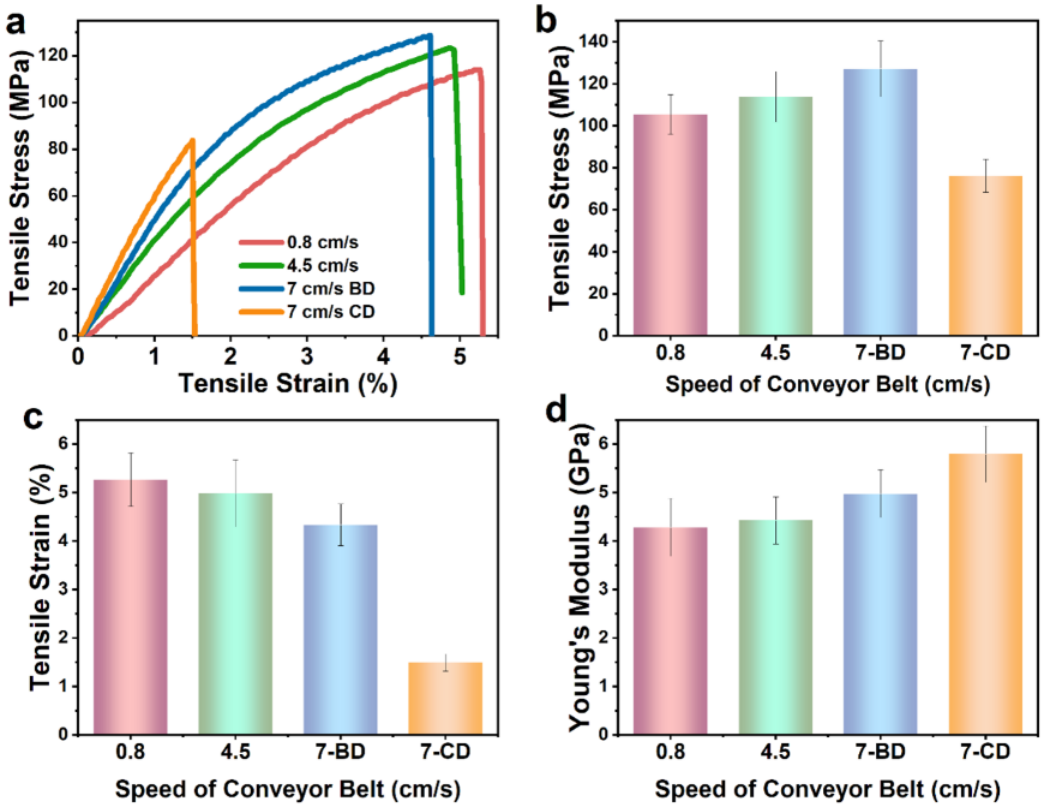

Figure 3. 9 (a) Tensile stress vs strain of CCF (carboxyl group density of 1.8 mmol/g); (b) tensile stress at maximum load; (c) tensile strain maximum load; (d) Young's modulus of films made at speed of conveyor belt of 0.8, 4.5, 7 cm/s

Table 3. 1 Comparison of Mechanical Properties of cellulose films with other polymeric films

Films	Tensile stress at maximum load (MPa)	Elongation at break (%)	Young's modulus (GPa)	Ref
LDPE	9.4-25.5	80-920	0.15-0.52	43
HDPE	22.6	358	0.28	44
PS	43.1	4.1	0.95	44
Bacterial cellulose	200-300	1.5-2.0	15-35	45
Polypropylene (PP)	30-40	100-600	1-1.5	45
Polyethylene terephthalate (PET)	157-177	70	3.5	46
PVA	39-118	225	2.9	46
Cellophane	20-100	15-40	2-3	45
CCF (BD)	105-125	4.3-5.2	4.5-5	This work

Figure 3. 10 schematically depicts the crystal structure of CMF. Three predominant planes, denoted by peaks in XRD spectra (Figure 3. 7), namely (110), $(1\bar{1}0)$ and (020) are represented in orange, green, and blue, respectively. Most of these planes are oriented parallel to the direction of the conveyor belt. In the cubic unit cells, the (110) and $(1\bar{1}0)$ planes are perpendicular to each other. Importantly, all three planes are preferential parallel to both the CMF chain and the BD during extrusion from the slit. This crystallographic alignment contributes to the enhancement of the mechanical properties observed in CMF film.

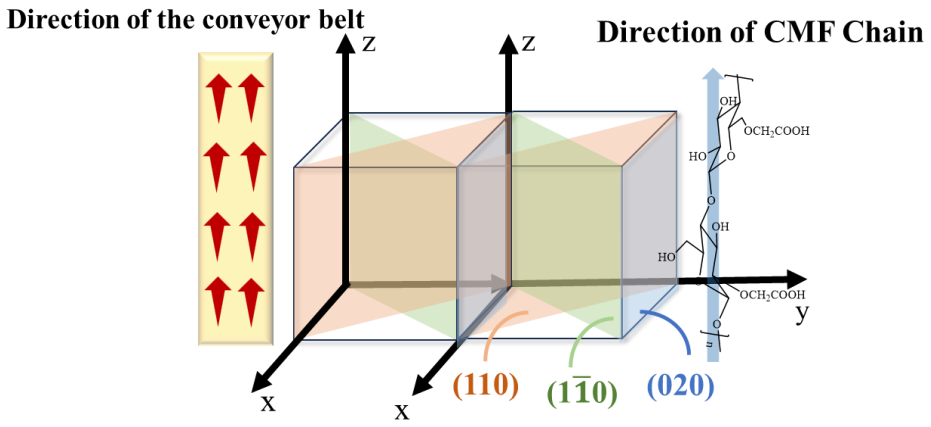

Figure 3. 10 Crystal structure of CCF with the direction of the conveyor belt and the CMF chain.

Figure 3. 11 shows the porosity and water vapor permeation of CCF regenerated at three speeds. The porosity of all CCF is around 9.8% and the water vapor permeation for all CCF remains is about 3.45×10^{-11} J/ms/Pa and 167 g/m^2/day. ANOVA analysis for porosity and WVP showed no significant difference. These results show that the speed of the conveyor belt does not affect the porosity and water vapor permeation of resolidified CCF significantly. This is because all of the films had a similar porosity (9-10%) and a similar thickness (53 µm).

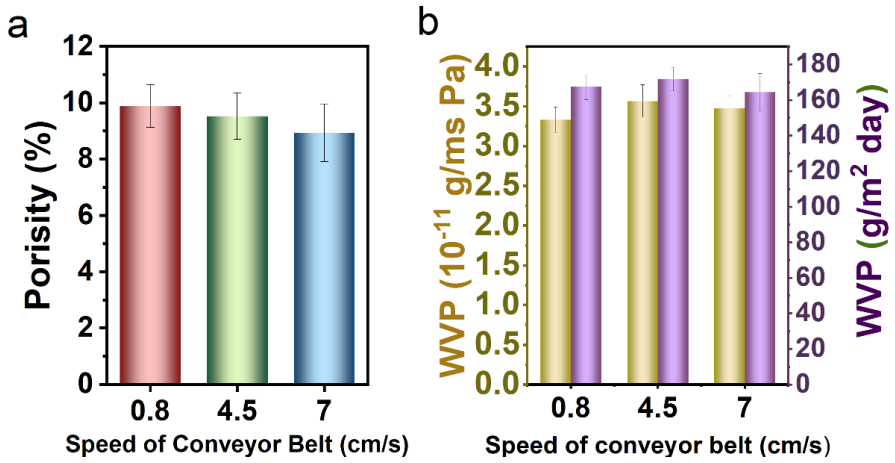

Figure 3. 11 (a) Porosity of CCF (carboxyl group content of 1.8 mmol/g) made from 7, 4.5 and 0.8 cm/s; (b) WVP of CCF made at 7, 4.5 and 0.8 cm/s. The One-way ANOVA analysis showed no significant difference between the data.

3. 5 Concluding remarks

Cellulose has attracted significant attention as a renewable and environmentally friendly alternative to petroleum-derived polymers. Here, the pulp was first carboxymethylated to synthesize CMF, a process validated by IR, XRD and ^{13}C NMR. The DS of CMF was determined by solid-state NMR and can be adjusted by varying the carboxymethylation parameters. Subsequently, a dope was prepared by dissolving CMF in an alkaline solution, followed by a continuous flow casting method that consisted of filling a feeder with dope, extruding it through a slit onto a conveyor belt partially immersed in a tank filled with an aqueous solution of acid. After exiting the tank, the generated film (CCF) was air-dried. The XRD results reveal that the generated film is anisotropic with the $(1\bar{1}0)$, (110) and (020) planes aligning along the belt direction. The tensile stress analysis indicated higher values in the BD compared to the CD, with stress increasing

with the conveyor belt speed. The phenomenon is attributed to the superior orientation of crystals and polymers in the BD, particularly at higher flow rates. Because the crystals and polymers are better oriented in BD and with a higher flowing speed. The resolidification process primarily produces carbon dioxide from partial decarboxylation and sodium sulfate from the neutralization reaction. However, the acid bath can be reused as long as the pH is less than 3.5, in the presence of these salts. Additionally, isopropyl alcohol and ethanol are not consumed and recyclable. This process is more environmentally friendly and less harmful than cellophane production, in which significant amounts of extremely toxic carbon disulfide are used.

To summarize, this ecofriendly and continuous method of making CCF from an abundant inexhaustible biomaterial demonstrates the feasibility of manufacturing robust and flexible film.

A future post-treatment study will be required such as the addition of hydrophobic groups or a plasticizer coating, to optimize CCF properties for specific applications.

3. 6 Supporting Information

A video detailing the process of continuously regenerating of cellulose-based film can be found on https://youtu.be/I_xqrq5uZBg?si=DQgfB3VzS5LulPzD

3. 7 References

[1] Pawar, P. R.; Shirgaonkar, S. S.; Patil, R. B. Plastic marine debris: Sources, distribution and impacts on coastal and ocean biodiversity. PENCIL Publication of Biol. Sci. **2016**, *3*(1), 40-54. DOI: https://www.researchgate.net/publication/295919494

[2] Alam, O.; Billah, M.; Yajie, D. Characteristics of plastic bags and their potential environmental hazards. Resour. Conserv. Recycl. **2018**, *132*, 121-129. DOI: https://doi.org/10.1016/j.resconrec.2018.01.037

[3] Pearson, M.; Khare, E. Addressing the single-use plastic proliferation problem. **2022**, MIT Sci. Policy. Rev.

[4] Ojagh, S. M. A.; Vahabzadeh, F.; Fallah, N.; van de Ven, T. G. M; Hamzehpoor, E.; Cranmer-Smith, S.; Lan, X. Hairy bacterial nanocellulose: Preparation and bioconjugation with an antibacterial agent. Cellulose. **2023**, *30* (17), 10905-10922. DOI: https://doi.org/10.1007/s10570-023-05542-9

[5] Kollarigowda, R. H.; Abraham, S.; Montemagno, C. D. Antifouling cellulose hybrid biomembrane for effective oil/water separation. ACS Appl. Mater. Interfaces. **2017**, *9*(35), 29812-29819. DOI: https://doi.org/10.1021/acsami.7b09087

[6] Zhang, S.; Yu, C.; Liu, N.; Teng, Y.; Yin, C. Preparation of transparent anti-pollution cellulose carbamate regenerated cellulose membrane with high separation ability. Int. J. Biol. Macromol. **2019**, *139*, 332-341. DOI: https://doi.org/10.1016/j.ijbiomac.2019.07.146

[7] Liu, X.; Xiao, W.; Ma, X.; Huang, L.; Ni, Y.; Chen, L.; Ouyang, X.; Li, J. Conductive regenerated cellulose film and its electronic devices–a review. Carbohydr. Polym. **2020**, *250*, 116969. DOI: https://doi.org/10.1016/j.carbpol.2020.116969

[8] Li, S.; Wang, X.; Guo, Y.; Hu, J.; Lin, S.; Tu, Y.; Chen, L.; Ni, Y.; Huang, L. Recent advances on cellulose-based nanofiltration membranes and their applications in drinking water purification: A review. J. Cleaner. Prod. **2022**, *333*, 130171. DOI: https://doi.org/10.1016/j.jclepro.2021.130171

[9] Amiri, M.; Jafarbeigi, E.; Salimi, F. Fabrication of modified nanofiltration membranes by functionalized cellulose nanocrystals with high anti-fouling capability in removing dye from water and wastewater. Korean. J. Chem. Eng. **2022**, *39*(3), 616-627. DOI: https://doi.org/10.1007/s11814-021-0952-8

[10] Tsai, C. H.; Lee, W. J.; Chen, C. Y.; Liao, W. T.; Shih, M. Formation of solid sulfur by decomposition of carbon disulfide in the oxygen-lean cold plasma environment. Ind. Eng. Chem. Res. **2002**, *41*(6), 1412-1418. DOI: https://doi.org/10.1021/ie010292s

[11] Wang, J.; Gardner, D. J.; Stark, N. M.; Bousfield, D. W.; Tajvidi, M.; Cai, Z. Moisture and oxygen barrier properties of cellulose nanomaterial-based films. ACS Sustainable Chem. Eng. **2018**, *6*(1), 49-70. DOI: https://doi.org/10.1021/acssuschemeng.7b03523

[12] Harlin, A. Cellulose carbamate: production and applications. VTT Technical Research Centre of Finland, VTT Technical Research Centre of Finland. 2019. DOI: 10.32040/2019.978-951-38-8707-0

[13] Weißl, M.; Hobisch, M. A.; Johansson, L. S.; Hettrich, K.; Kontturi, E.; Volkert, B.; Spirk, S. Cellulose carbamate derived cellulose thin films: preparation, characterization and blending with cellulose xanthate. Cellulose, **2019**, *26*, 7399-7410. DOI: https://doi.org/10.1007/s10570-019-02600-z

[14] Gemili, S.; Yemenicioğlu, A.; Altınkaya, S.A. Development of cellulose acetate based antimicrobial food packaging materials for controlled release of lysozyme. Journal of Food Engineering, **2009**, *90*(4), 453-462. DOI: https://doi.org/10.1007/s10570-019-02600-z

[15] Balasubramaniam, S. P. L.; Patel, A.S.; Nayak, B. Surface modification of cellulose nanofiber film with fatty acids for developing renewable hydrophobic food packaging. Food Packag. Shelf Life, **2020**, *26*, 100587. DOI:https://doi.org/10.1016/j.fpsl.2020.100587

[16] Lease, J.; Kawano, T.; Andou, Y. Esterification of cellulose with long fatty acid chain through mechanochemical method. Polym. **2021**, *13*(24), 4397. DOI: https://doi.org/10.3390/polym13244397

[17] Šešlija, S.; Nešić, A.; Škorić, M. L.; Krušić, M. K.; Santagata, G.; Malinconico, M. Pectin/carboxymethylcellulose films as a potential food packaging material. Macromol. Symp. **2018**, *378*(1), 1600163. DOI: https://doi.org/10.1002/masy.201600163

[18] Moradian, M.; Wiebe, H.;van de Ven, T. G. M. Ultrathin ultrastrong transparent films made from regenerated cellulose and epichlorohydrin. Carbohydr. Polym. **2023**, *318*, 121131. https://doi.org/10.1016/j.carbpol.2023.121131

[19] Zheng, M.; Chen, J.; Tan, K. B.; Chen, M.; Zhu, Y. Development of hydroxypropyl methylcellulose film with xanthan gum and its application as an excellent food packaging bio-material in enhancing the shelf life of banana. Food Chem. **2022**, *374*, 131794. DOI: https://doi.org/10.1016/j.foodchem.2021.131794

[20] Teisala, H.; Tuominen, M.; Kuusipalo, J. Superhydrophobic coatings on cellulose-based materials: fabrication, properties, and applications. Adv. Mater. Interfaces, **2014**, *1*(1), 1300026. DOI: https://doi.org/10.1002/admi.201300026

[21] Zhang, L.; Ruan, D.; Zhou, J. Structure and properties of regenerated cellulose films prepared from cotton linters in NaOH/urea aqueous solution. Ind. Eng. Chem. Res. **2001**, *40*(25), 5923-5928. DOI: https://doi.org/10.1021/ie0010417

[22] Ma, B.; Qin, A.; Li, X.; He, C. Preparation of cellulose hollow fiber membrane from bamboo pulp/1-butyl-3-methylimidazolium chloride/dimethylsulfoxide system. Ind. Eng. Chem. Res. **2013**, *52*(27), 9417-9421. DOI: https://doi.org/10.1021/ie401097d

[23] Li, G.; Zhang, B.; Tan, Z.; Jiang, L.; Yao, Z.; Zhang, L. Fabrication of Cellulose Nanofiltration Membranes by Reusing a Binary Solvent of EMIMAc Ionic Liquid and DMSO. Ind. Eng. Chem. Res. **2023**, *62*(36), 14588-14600. DOI: https://doi.org/10.1021/acs.iecr.3c02148

[24] Pang, J. H.; Wu, M.; Zhang, Q.; Tan, X.; Xu, F.; Zhang, X.; Sun, R. Comparison of physical properties of regenerated cellulose films fabricated with different cellulose feedstocks in ionic liquid. Carbohydr. Polym. **2015**, *121*, 71-78. DOI: https://doi.org/10.1016/j.carbpol.2014.11.067

[25] Zheng, X.; Huang, F.; Chen, L.; Huang, L.; Cao, S.; Ma, X. Preparation of transparent film via cellulose regeneration: Correlations between ionic liquid and film properties. Carbohydr. Polym. **2019**, *203*, 214-218. DOI: https://doi.org/10.1016/j.carbpol.2018.09.060

[26] Moradian, M.; Islam, S.; van de Ven, T. G. M. Insoluble regenerated cellulose films made from mildly carboxylated dissolving and kraft pulps. Ind. Eng. Chem. Res. **2021**, *60*(15), 5385-5393. DOI: https://doi.org/10.1021/acs.iecr.1c00485

[27] Pino P, Sawalha H, Moradian M, et al. Effects of the coagulation bath on the properties of regenerated carboxymethylated cellulose films. Cellulose, 2024, 31(17): 10389-10401.

[28] Van De Ven, T.G. M.; Alam, N.; Lumb, J.P.; Islam, S.;Moradian, M., Cellulose-based filaments, films and 3d objects and methods of manufacture thereof. 2024, U.S. Patent Application No. 18/555,768. DOI: https://patents.google.com/patent/US20240198579A1/en

[29] Yang, H.; Tejado, A.; Alam, N.; Antal, M.;, T. G. M. Films prepared from electrosterically stabilized nanocrystalline cellulose. Langmuir, **2012**, *28*(20), 7834-7842. DOI: https://doi.org/10.1021/la2049663

[30] Foner, H. A.; Adan, N. The characterization of papers by X-ray diffraction (XRD): measurement of cellulose crystallinity and determination of mineral composition. J. Forensic Sci. Soc. **1983**, *23*(4), 313-321. DOI: https://doi.org/10.1016/S0015-7368(83)72269-3

[31] Kono, H.; Hashimoto, H.; Shimizu, Y. NMR characterization of cellulose acetate: chemical shift assignments, substituent effects, and chemical shift additivity. Carbohydr. Polym. **2015**, *118*, 91-100. DOI: https://doi.org/10.1016/j.carbpol.2014.11.004

[32] Yadav, M.; Chiu, F. C. Cellulose nanocrystals reinforced κ-carrageenan based UV resistant transparent bionanocomposite films for sustainable packaging applications. Carbohydr. Polym. **2019**, *211*, 181-194. DOI: https://doi.org/10.1016/j.carbpol.2019.01.114

[33] Moradian, M.; van de Ven, T. G. M., Formation of cellulose microspheres and nanocrystals from mildly carboxylated fibers. Cellulose, **2022**, *29*(6), 3225-3237.

DOI: 10.1007/s10570-022-04486-w

[34] Chen, W.; He, H.; Zhu, H.; Cheng, M.; Li, Y.; Wang, S. Thermo-responsive cellulose-based material with switchable wettability for controllable oil/water separation. Polym. **2018**, *10*(6), 592. DOI: https://doi.org/10.3390/polym10060592

[35] Kumar, V.; Yang, T. Analysis of carboxyl content in oxidized celluloses by solid-state ^{13}C CP/MAS NMR spectroscopy. Int. J. Pharm. **1999**, *184*(2), 219-226. DOI: https://doi.org/10.1016/S0378-5173(99)00098-8

[36] French, A. D.; Santiago Cintrón, M. Cellulose polymorphy, crystallite size, and the Segal Crystallinity Index. Cellulose, **2013**, *20*, 583-588.

DOI: https://doi.org/10.1007/s10570-012-9833-y

[37] Nam, S.; French, A. D.; Condon, B. D.; Concha, M. Segal crystallinity index revisited by the simulation of X-ray diffraction patterns of cotton cellulose Iβ and cellulose II. Carbohydr. Polym. **2016**, *135*, 1-9. DOI: https://doi.org/10.1016/j.carbpol.2015.08.035

[38] Lin, X.; Qu, T.; Qi, S. Kinetics of the carboxymethylation of cellulose in the isopropyl alcohol system. Acta Polym. **1990**, *41*(4), 220-222. DOI: https://doi.org/10.1002/actp.1990.010410406

[39] Chen, J.; Tang, C.; Yue, Y.; Qiao, W.; Hong, J.; Kitaoka, T.; Yang, Z. Highly translucent all wood plastics via heterogeneous esterification in ionic liquid/dimethyl sulfoxide. Ind. Crop. Prod. **2017**, *108*, 286-294. DOI: https://doi.org/10.1016/j.indcrop.2017.06.054

[40] Chang, S. T.; Chang, H. T. Comparisons of the photostability of esterified wood. Polym. Degrad. Stab. **2001**, *71*(2), 261-266. DOI: https://doi.org/10.1016/S0141-3910(00)00171-3

[41] Bajpai, P.; Biermann's Handbook of Pulp and Paper: Volume 1: Raw Material and Pulp Making. 2018: Elsevier.

[42] Gigac, J.; Fišerová, M. Effect of velocity gradient on papermaking properties. Cellulose Chemistry & Technology 2010, 44 (9), 389.

[43] Overview of materials for Low Density Polyethylene (LDPE), Blow Molding Grade. DOI: https://www.matweb.com/search/DataSheet.aspx?MatGUID=b34a78d271064c4f85f28a9ffaf94045&ckck=1 Accessed Aug. 22. 2024

[44] Taşdemır, M.; Gülsoy, H. Ö., Mechanical properties of polymers filled with iron powder. Int. J. Polym. Mater., 2008. *57*(3), 258-265. DOI: https://doi.org/10.1080/00914030701473656

[45] Klemm, D.; Heublein, B.; Fink, H.P.;Bohn, A., Cellulose: fascinating biopolymer and sustainable raw material. Angew. Chem. Int. Ed., 2005. *44*(22), 3358-3393. DOI: https://doi.org/10.1002/anie.200460587

[46] Bastarrachea, L.; Dhawan, S.; Sablani, S. S., Engineering properties of polymeric-based antimicrobial films for food packaging: a review. Food Engineering Reviews, 2011. *3*(2), 79-93. DOI: https://doi.org/10.1007/s12393-011-9034-8

Preface to Chapter 4

In the previous chapter, a continuous production method for cellulose microfibril (CMF) films was introduced and the transparency can be adjusted by varying the charge density of carboxylated cellulose. Most importantly, the films' tensile strength showed a slight increase when the conveyor belt speed was increased. Additionally, the crystallinity of the films decreased as the conveyor belt speed was lowered. These facts further prove that the majority of cellulose chains align with most of the crystalline planes in the direction of the conveyor belt. These results emphasize the significant role that processing conditions play in shaping the structural properties of CMF films.

However, despite these promising attributes, the films' intrinsic hydrophilicity poses a notable challenge in certain applications. Specifically, when packaging perishable goods, such as grapes, films need to provide mechanical strength, transparency, and hydrophobicity, as well as anticondensation properties, in order to preserve freshness and extend shelf life. However, their hydrophilicity makes the CMF films barely applicable for anticondensation purposes. This chapter addresses this limitation by silanization, which helps enhance the water resistance and hydrophobicity of CMF films. The silanization, which can increase the water vapor transmission rates, aims to improve the anticondensation properties of the films, thereby making them more suitable for perishable food packaging applications. Our findings demonstrate the silanization improves significantly in increasing the water resistance of the films, roughness, as well as water vapor transmission rates, thus guaranteeing that the films exhibit superior anticondensation properties.

Chapter 4

Hydrophobization and anti-condensation of cellulose-based films by silanization

4. 1 Abstract

The substitution of plastic with eco-friendly resources such as cellulose is particularly challenging. One of the primary challenges hindering the application of cellulose films as a substitute for plastics is their inherent hydrophilicity. In this study, we present methods to enhance the water resistance properties of carboxymethylated cellulose fiber (CMF) films through silanization with methyltrichlorosilane (achieved within 5 seconds) to yield SCMF1, and with tetraethylorthosilicate (completed over 24 hours) to produce SCMF2. The silanization was confirmed by Fourier-transform infrared spectroscopy, X-ray photoelectron spectroscopy and nuclear magnetic resonance. Various physical and mechanical properties are also assessed. In stark contrast to CMF film (~55°), the water contact angle increased to 131° and 73.5° for SCMF1 and SCMF2 respectively, indicating a marked improvement in hydrophobicity, especially of SCMF1. Moreover, the porosity of films increased after silanization, rendering them well-suited for various anticondensation packaging applications. We found that French fried potatoes, when covered with SCMF 2 and SCMF 1, maintained their crispness and freshness for longer times than those covered by polyethylene. Beyond applications in certain food packaging grades, the innovative post-treatment of cellulose-based film indicates exceptional potential to be used in a variety of non-food packaging applications.

Keywords carboxymethyl cellulose film (CMF film); silanization, silanized CMF film, hydrophobicity, food packaging

4. 1. 1 Graphic Abstract

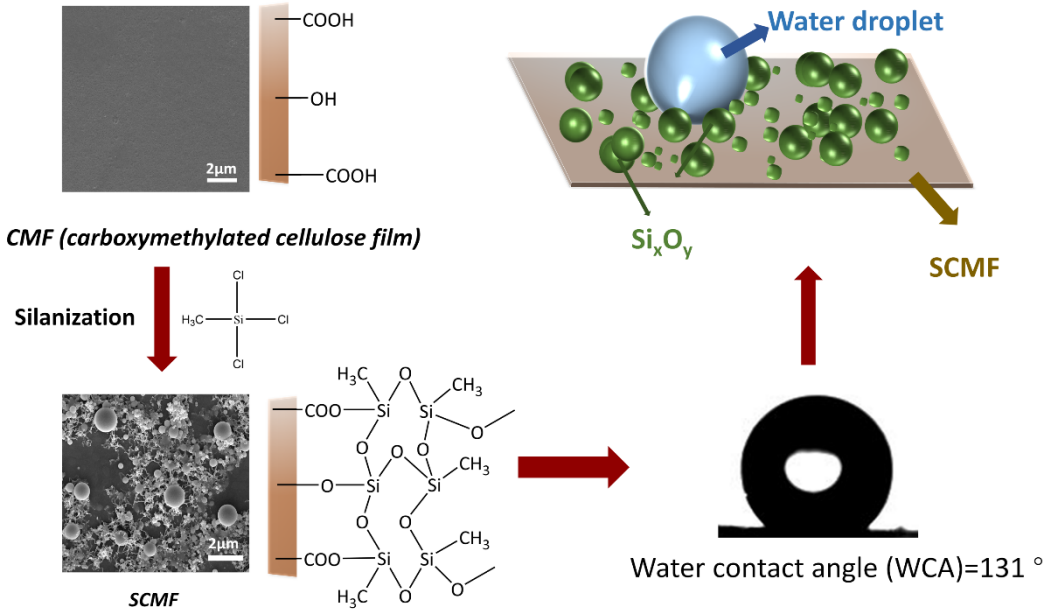

Figure 4. 1 The SEM images of SCMF1 and changes in chemical structure before and after silanization (left), and the water contact angle for SCMF1 with a schematic diagram of a water droplet on silanized film (right).

4. 2 Introduction

Advancements in food packaging are urgently anticipated given the rapid progress in nanotechnology and biotechnologies, as well as the escalating in consumer demands. The suitability of any material for food packaging hinges on its ability to offer consumer convenience while safeguarding food products from degradation and contamination [1]. An example is moisture condensation in closed environments with food items like mushrooms, fruits, and other moisture-sensitive products, say, French fried potatoes.

Excessive condensed moisture not only causes the loss of the freshness of foods [2], but also fosters the proliferation of bacteria [3]. Most of the modern prevalent food packaging materials are petroleum-based non-biodegradable polymers, such as polyethylene (PE), polypropylene (PP), polystyrene (PS), polyvinyl chloride (PVC) and polyvinylidene chloride (PVDC). All of them, however, pose environmental and human health problems [1, 4-7]. Indeed, the replacement of sustainable alternatives has become a burning issue.

Cellulose, as a biodegradable feedstock, has been utilized in food packaging due to its cost-effectiveness, outstanding processability, and noteworthy film-forming capabilities [8-11]. Regenerated cellulose films, distinguished by their flexibility and strength resulting from robust hydrogen bonding between cellulose chains, are regarded as viable substitutes for conventional plastic-based packaging materials [9, 12]. Therefore, numerous efforts have been made to develop cellulose films with the characteristics of plastics for food packaging [13-18]. The difficulty in solubilizing cellulose is a big challenge. Generally, the dissolution of cellulose involves using

appallingly environmentally unfriendly solvents along with a rather lengthy and tedious processing procedure [10, 19].

Solvents commonly used to dissolve cellulose, such as N,N-Dimethylacetamide (DMAc)/Lithium Chloride (LiCl) System, or a copper ethylene diamine solution pose health risks to humans. Ionic liquids are increasingly gaining interest as green and ecological solvents for cellulose, though they usually necessitate heating, a combination of organic solvents, and protracted residence times [20-23]. Moreover, the cost of these solvents remains a limiting factor. Deep eutectic solvents (DES) have garnered significant attention as innovative solvents for cellulose due to their low cost, relatively low toxicity, and ease of preparation.

Another common method of dissolving cellulose involves surface modification. Soluble derivatives of cellulose include cellulose carbamate, which is formed by heating cellulose with urea in the presence of a catalyst, and cellulose xanthate, which is widely used to produce viscose rayon [24, 25]. A film composed of a blend of cellulose carbamate and cellulose xanthate, prepared using spin coating techniques, exhibits a significant water uptake of approximately 85% [26].

Apart from that, relatively low-cost renewable cellulose-based films, such as cellophane, are extensively utilized in food packaging due to their biodegradability, wide-spread availability and other favorable properties. However, the production process for both cellophane and cellulose xanthate involves the use of carbon disulfide, a highly toxic compound [12, 27-29]. Besides, the relatively high cost of films and the difficulty associated with continuous production in a continuous process restrict their application. Hence, it is desirable to develop a facile and ecological approach for the fabrication of regenerated cellulose films.

According to a previous study in our lab, a cellulose derivative, carboxymethyl cellulose fiber (CMF) was effectively synthesized from kraft pulp by the introduction of carboxyl groups [30-32], yielding a degree of substitution (DS) in the range up to 0.4 (12%). This low DS prevents fiber dissolution in water at neutral pH, while facilitating their dissolution in highly alkaline solutions and subsequent regeneration in an acid bath via a flow casting method, producing CMF films [30, 31]. However, CMF exhibits susceptibility to moisture due to the presence of hydroxyl and carboxyl groups rendering it hydrophilicity and hindering its application in food packaging.

Similarly, cellulose films derived from other studies also features a hydrophilic surface because of abundant hydroxyl groups. The absorption of water, resulting in film swelling, will impose an adverse impact on the film's strength [33]. When keeping dry foods such as nuts, the utilization of hydrophobic films is imperative to prevent bacterial growth induced by high moisture levels. On the other hand, to keep perishable food, packaging must possess breathability and anti-condensation attributes to counteract bacterial proliferation resulting from elevated moisture levels stemming from fruit respiration, thereby preventing spoilage [34]. It is reported that the loss of crispiness and freshness of French-fried potatoes is attributed to water absorption [2]. Humidity-responsive smart gates have been devised based on glycerol-cross-linked polyvinyl alcohol and porous polyvinylidene fluoride bilayer films, offering humid control and anti-condensation capabilities when relative humidity exceeds typical thresholds [35]. Huang et al [36] developed an anti-condensation coating employing SiO_2 and TiO_2 to mitigate icing-condensation on pavements. Wu et al [37] examined the formulation of a breathable coating on cementitious surfaces incorporating a bio-based epoxy resin, butyl acetate and SiO_2 nanoparticles, and a hydrophobic component, designed to deter condensation. They synthesized a spray-applicable anti-

condensation coating comprising polyester and SiO_2 nanoparticles on cementitious materials, which was designed to solve the problem of condensation on wall or ceiling [38]. However, little research has been performed. exploring the amalgamation of hydrophobicity and anticondensation properties in cellulose-based film used in food packaging.

The hydrophobization of cellulose can be achieved via physical absorption [39], chemical surface modification, coating, or the introduction of hydrophobic groups, combination of polymer grafting with plasma treatment [40] or ball milling [41]. For example, hydrophobic cellulose film surface can be prepared by wax [42], alkylation [43], acetylation [44], silanization [45]) as well as modification with block polymer [46], and addition of hydrophobic fumed SiO_2 nanoparticles [47].

Among all these methods silanization is proven to be an effective way to make cellulose film hydrophobic for various purposes [45, 48, 49]. Yu et al. [50] altered the hydrophobicity of filter paper by performing silanization with perfluorooctyltriethoxysilane (PFTS), achieving a remarkable oil/water separation efficiency of over 99%.

The demonstrated progress in silanization of cellulose motivated us to develop a facile method to generate and modify cellulose-based films and explore their hydrophobicity and anti-condensation properties.

To the best of our knowledge, there has been a lack of comprehensive research focusing on the hydrophobicity and anti-condensation properties of films used for packaging of perishable food. This represents a significant gap in literature, given the increasing demand for effective and sustainable packaging solutions in the food industry. Therefore, this type of hydrophobic modification holds great promise for certain food packaging, especially for fruits and vegetables.

Here, we used the same soft wood pulp we used before to fabricate CMF films [30, 31]. It contains besides cellulose, 12.3% hemicellulose and 0.14% lignin [51]. The solvent utilized in this process, isopropanol alcohol, is environmentally sustainable. The sodium hydroxide and sulfuric acid employed during the carboxymethylation process and in the formulation of the dope will ultimately transform into salts within the regeneration. This methodology embodies a relatively eco-friendly approach to dissolve and fabricate cellulose-based films, showcasing significant advantages over conventional solvents used for cellulose dissolution. We further performed a post-treatment on CMF films by a silanization reaction that renders the cellulose hydrophobic. Two different chemicals, methyltrichlorosilane (MTCS) and tetraethylorthosilicate (TEOS), were employed for the surface modification of CMF, resulting in SCMF 1 and SCMF 2, respectively. The porosity, morphology, moisture absorption, water uptake, water vapor permeation, water contact angle, mechanical properties and an anti-condensation test of the modified film were performed. We hypothesize that the hydrophobicity and anti-condensation properties of CMF films can be enhanced through silanization, rendering them suitable for certain types of food packaging.

4. 3 Experimental section

4. 3. 1 Materials

Unrefined, bleached softwood kraft pulp (FPInnovations, Canada) was ground using a GlenMills SM300 grinder (Clifton, NJ, USA) and screened with a 0.5 mm sieve. Then it was reground and screened by 0.25 mm sieve. Reagent-grade sodium chloroacetate (MCA), sodium hydroxide (NaOH), sulfuric acid (H_2SO_4), methyltrichlorosilane (MTCS), and tetraethylorthosilicate (TEOS), and ethanol were purchased from Sigma-Aldrich (Oakville, ON, Canada) and used as received.

100% virgin polyethylene (PE film) was bought from ULINE Canada (Milton, ON, Canada). Freshly cooked French fried potatoes were purchased from McDonald's (Montreal, QC, Canada).

4. 3. 2 Carboxymethylation

Milled pulp was carboxymethylated to a target carboxyl charge density of 1.8 mmol/g (DS = 0.3) under the following experimental conditions [30-32]. Initially, a 1 L glass bottle was first filled with 20 g of the powdered pulp, followed by the addition of 170 g of isopropyl alcohol. Subsequently, the mixture was stirred in a 50 °C water bath and a 15.8 mmol/L sodium hydroxide solution was introduced. After 1 hour, the temperature was raised to 60 °C and sodium chloroacetate solution was added for the carboxylation of cellulose. After 120 minutes, the fibers were washed with 400 g of 80% ethanol twice followed by vacuum-filtered using a 60 μm nylon cloth. Following the washing state, CMF was air-dried and stored for further usage at room temperature.

4. 3. 3 Dope and Film Preparation

CMF was partially decarboxylated by the addition of a 5% sulfuric acid solution to the dried CMF [51]. CMF and the sulfuric acid solution had a weight ratio of 1:7. Following the addition of 50% NaOH, CMF was dissolved and made into a dope and its cellulose content was adjusted to 10%. Following that, centrifugation was carried out for 30 minutes at 1000 rpm. The resulting dope was cast onto a Teflon mold with a thickness of 1 mm and immersed in a 20% sulfuric acid bath. After 10 minutes, the CMF film was properly formed. The CMF film was then submerged for 30 minutes in DI water for removal of the acid. The wet film was then air-dried and kept for future usage at room temperature.

4. 3. 4 Silanization

The typical manufacturing process of silanization in the liquid phase is as follows [52, 53]. First, 10 mL of MTCS was added to a 50 mL glass beaker and one piece of dry CMF film was immersed in it for 5 seconds. Then, the processed SCMF 1 was immersed in ethanol for washing. Finally, the film was dried in a drying oven at 50 °C for 30 minutes. The production of SCMF 2 followed a similar process, CMF films were first put in water for 10 minutes followed by 100 ml of ethanol for solvent exchange. After that, 10 mL of TEOS was added into a 50 mL glass beaker, followed by the immersion of CMF film. The mixture was stirred well at room temperature for 24 h. After the reaction, the SCMF 2 film was left in ethanol for 24 hours for washing.

4. 3. 5 Determination of Carboxyl Charge Density

Following the procedure by Yang *et al.* [54], conductometric titrations were carried out on a Metrohm 836 Titrando apparatus to quantify the charge density of carboxyl groups. Specifically, 50 mg of dry sample was thoroughly mixed with 100 mL of distilled water, after which 1 M HCl was added to bring the pH level to 3.5. Subsequently, the sample mixture was incrementally titrated with 45 mL of a 10 mmol/L NaOH solution for a few hours. The plot of conductance versus the volume of additional NaOH was used to determine the carboxyl content.

4. 3. 6 Field-Emission Scanning Electron Microscopy and Energy Dispersive X-ray Spectroscopy

A high-resolution FEI Quanta 450 Environmental Scanning Electron Microscope (FE-ESEM, Hillsboro, OR, USA) with EDAX Octane Super 60 mm2 SDD and TEAM EDS Analysis System was used for imaging. To obtain sharp cross-sections for imaging, the films were fractured under liquid nitrogen.

4. 3. 7 Fourier Transform Infrared (FTIR)

FTIR spectra were collected by attenuated total reflectance (ATR, PerkinElmer, Waltham, USA) with a single bounce diamond to observe the surface chemical characteristics of CMF and silanized films. Dry samples were placed on the ATR crystal, and then the pressure clamp tip was lowered until the samples were subjected to the required pressure. The spectra covered wave numbers from 400 to 4000 cm^{-1} with a 4 cm^{-1} resolution.

4. 3. 8 Solid-state ^{29} Si NMR spectroscopy

Solid-state Silicon-29 and Carbon-13 Nuclear Magnetic Resonance (NMR) spectra were acquired using a Varian/Agilent VNMRS instrument operating at a frequency of 80 MHz and 100.4 MHz, respectively. For the ^{29}Si NMR, the samples, consisting of ground SCMF film, were uniformly packed into a 4 mm zirconium rotor and spun at 5000 Hz. Each spectrum was acquired by accumulating 1051 transients, with an acquisition time of 30 ms and a recycle delay of 5 seconds. For the ^{13}C NMR, a 4 mm rotor was filled with film strips that measured 3 mm in width and 3 cm in length, and it was spun at 10 kHz. Each spectrum was obtained with an acquisition time of 25 ms, a recycle delay of 3 seconds, and the accumulation of 14,000 scans.

4. 3. 9 Moisture Absorption (MA) and Water absorption (WA)

Following the procedure ASTM D5229 [55], moisture absorption is determined. The dried films of size 4 cm x 4 cm were placed in a sealed chamber for approximately 24 h (condition: 25 °C with 95% relative humidity). Finally, the MA was determined by the following formula:

$$MA(\%) = \left[\frac{W_w - W_d}{W_d}\right] \times 100 \quad (1)$$

where W_w and W_d are the wet and dry weights of films, respectively. Similarly, the dry films of 4 cm by 4 cm were submerged in distilled water until they had absorbed the maximum amount of water for 1 hour to calculate the water absorption. The WA was finally calculated using the same formula.

4. 3. 10 Water Vapor Permeation (WVP)

The method ASTM-E96/E96-05 [56] was used to determine the water vapor permeation. The films were attached to the top surface of the dish using a water-resistant sealant. There was at least 1 cm between the top of the dish and the water's surface in a Petri dish that contained 20 g of DI water. Weights were assessed before and after 24 hours after Petri plates had been conditioned at 25 °C and 75% RH in a constant humidity chamber. The following formulae were used to determine the WVP and the WVTR water vapor transmission rate (WVTR):

$$WVP(g\ m^{-1}s^{-1}Pa^{-1}) = \left[\frac{w}{t}\right] dA^{-1}\Delta P^{-1} \quad (2)$$

$$WVTR(g\ m^{-2}day^{-1}) = \frac{w}{TA} \quad (3)$$

where w is the weight loss of water (g), t is time (s), T is time (day), d is the film thickness (m), A is the film area (m^2), and Δp is the vapor pressure difference (3167.2 Pa, at 25 °C).

4. 3. 11 Anticondensation/breathability Measurement

The anti-condensation test was carried out under room temperature (22 °C). Freshly cooked French fried potatoes were placed in a dish which was then sealed by films using a water-resistant glue.

Images were taken at certain times. The softness of the French fried potatoes was tested by breaking them manually.

4. 3. 12 Water Contact Angle (WCA)

An OCA20 contact angle device (Dataphysics, Filderstadt, Germany) was used to perform the water contact angle measurement. A CCD camera took photographs at certain times while a 4 μL water droplet was applied to the surface of a flat film using a Hamilton-Bonaduz microsyringe. The results are based on the average of at least three measurements, and each measurement was carried out on a different fresh point on the film.

4. 3. 13 Tensile and Porosity of Films

An Instron Mini 44 tensile tester with a 500 N load cell was used to measure the mechanical strength of the films in an ambient environment. The tests were conducted using film strips that were 5 mm wide and 30 mm long, stretching them at a rate of 5 mm per minute. Each result is based on a minimum of five measurements.

The porosity of the film is calculated by the following equation [57]:

$$Porosity(\%) = \left[1 - \frac{\rho_s}{\rho_{cell}}\right] \times 100 \quad (4)$$

ρ_{cell} is the density of cellulose (1.5 g/cm^3), ρ_s is the density of sample.

The porosity of the coated film is calculated by:

$$Porosity(SCMF)(\%) = \frac{\sum_1^2 P(\%)_i T_i}{T(SCMF)} \quad (5)$$

T_1 is the thickness of CMF layer and T_2 of the coated layer.

4. 3. 14 Three-point bending test

Three-point bending tests were conducted for all groups in accordance with the ASTM D-790M standard method [58]. The tests utilized the ADMET MTEST Quattro eXpert 7600 series (MA, USA) testing machine. A load was applied at the midpoint between the supporting points, with a crosshead speed set at 0.1 mm/s. Each result is based on a minimum of five measurements. This test was carried out on freshly cooked French fried potatoes with both width and thickness of 7 mm. The span between the supports was set to be 3 cm. The bending force and deflection were automatically recorded by the computer throughout the bending tests.

The flexural modulus of elasticity denoted by E_f is calculated using the equation [59]

$$E_f = \frac{L^3 m}{4bd^3} \quad (6)$$

L the span between the supports (mm), m the slope of the force-deflection curves (N/mm), and b and d the width and thickness of the test beam, respectively (mm).

4. 4 Results and Discussion

4. 4. 1 Determination of Carboxyl Charge Density

The carboxyl group charge density in CMF film was found to be 1.8 mmol/g by conductometric titration, corresponding to a degree of substitution DS = 0.3.

4. 4. 2 FTIR Analysis

FTIR analysis was performed to confirm the surface evolution of silanization. For the pulp and CMF, the wide bands observed at approximately 2860 and 3330 cm^{-1} are assigned to the stretching and bending vibration of the -CH- and -OH, respectively [60, 61]. The vibration at around 1600 cm^{-1} for CMF powder and 1730 cm^{-1} for CMF film corresponding to -COONa (in sodium form) and-COOH (protonated forms), respectively, proof that the carboxylation reaction was successful. For the graph of SCMF1 and SCMF2, the vibration at 2860 cm^{-1} corresponds to C-H, which sharpens and splits into two distinct peaks after the silanization on the surface of the CMF film, indicating successful formation of the siloxane linkage. The small bumping appears around 1150-1080cm^{-1} corresponds to Si-O-Si vibration [62]. The -COOH vibrations around 1730 cm^{-1} are absent after silanization (SCMF1 and SCMF2). This is due to the loss of -COOH groups due to silanization, which indicates that silanization occurs mostly at carboxyl groups [63]. The vibrations approximately at 795 cm^{-1}, and 1260 cm^{-1} are assigned to Si-O, and Si-C, respectively [64].

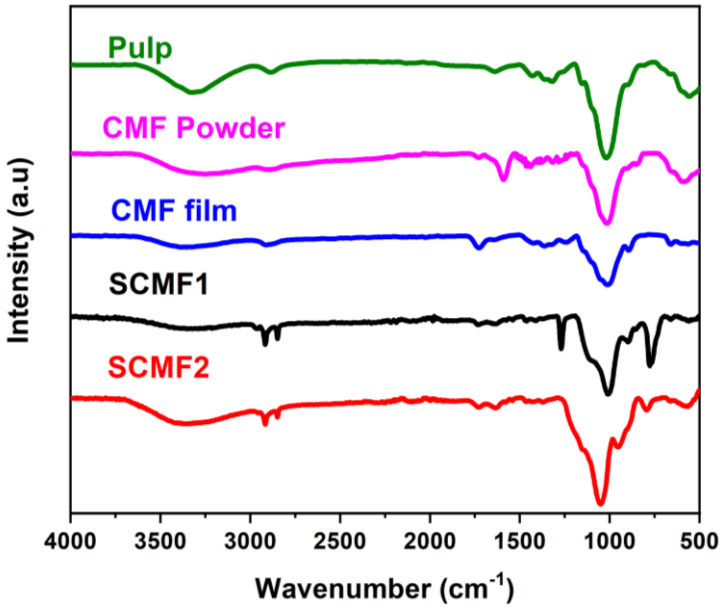

Figure 4. 2 FTIR spectra of the ground kraft pulp, CMF film of charge density 1.8 mmol/g), SCMF 1 and SCMF 2.

4. 4. 3 Solid NMR and XPS Analysis

Solid ^{29}Si NMR spectra of silanized films are presented in Figure 4. 3, revealing insights into the chemical environment surrounding silicon atoms. In particular, the Si chemical shift is intricately linked to the presence of siloxane bridges attached to silicon atoms. These bridges are characterized by the arrangement of silicon and oxygen atoms, denoted as Q for quaternary Si-O-, and T for three Si-O- bonds along with one organic group [65].

For SCMF1, peaks ranging from 50 to 60 ppm are attributed to T2 environments, while those between 62 and 72 ppm correspond to T3 (see insets in Figure 4. 3a). For SCMF 2, peaks observed at 85 to 95 ppm, 95 to 105 ppm, and 106.5 to 115 ppm are assigned to Q2, Q3, and Q4, respectively. The presence of these peaks corroborates the formation of a siloxane network grafted onto the

CMF film, consistent with findings in the literature [66]. Notably, the predominance of T3 sites in SCMF1 and Q3 sites in SCMF2, as depicted in Figure 4. 3, suggests a preference for the formation of three-dimensional siloxane structures over linear structures by both TCS and TEOS.

Solid ^{13}C NMR results of CMF film and silanizated film are presented. The peaks at 105 ppm, 85 ppm, and 65 ppm presented C1, C4, and C6 on the cellulose chain, respectively. The largest peak around 70-80 ppm is the peak for the combination of C2, C3, and C5. For CMF, the peaks at 20 ppm indicated methyl groups, which shifted to 38 ppm after silanization. Meanwhile, to qualify the content of the COOH group, which is around 175 ppm, the integral of C1 peaks is set to 1. Then the integral of the -COOH group for CMF, SCMF1, and SCMF 2 is 0.32, 0.22, and 0.25, respectively, which indicates the loss of carboxyl groups during surface modification. These facts showed that the silanization occurs more on the carboxyl groups on C7.

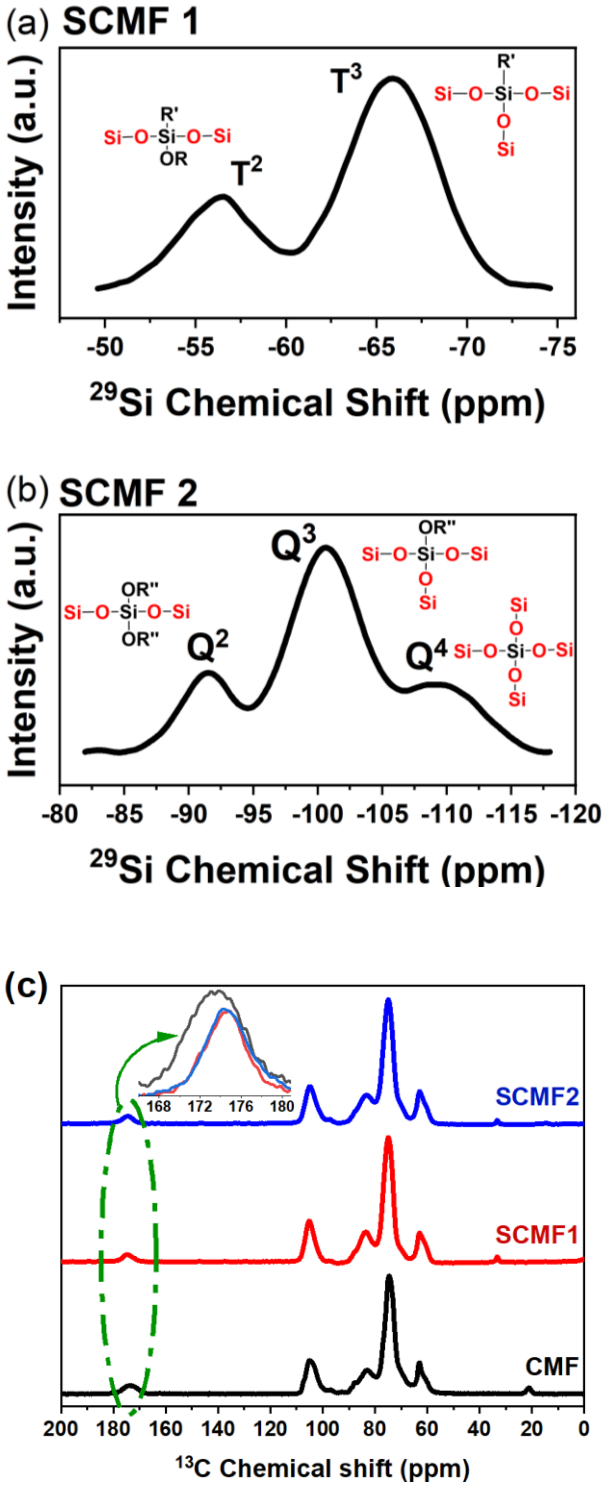

Figure 4. 3 ^{29}Si NMR spectra of SCMF 1(a) and SCMF 2 (b); ^{13}C NMR spectra of CMF, SCMF2 and SCMF2 with an inset of peaks from 168-180 ppm (c).

XPS was applied on SCMF films to further provide information on silanization. The XPS wide scan showed the C 1s band, the O 1s band, and the Si 2p band at 284, 532, and 102 eV, respectively [67, 68]. Subsequent high-resolution C 1s, O 1s, and Si 2p spectra of SCMF films along with their deconvolutions were also obtained.

In the C 1s band of SCMF 1 films, a singular peak at 284.7 eV was observed, indicative of carbon present in C-Si/C-C/C-H configurations [68, 69]. For SCMF2, the deconvolution revealed an additional peak at 286.5 eV, attributed to the C-O bond originating from TEOS, which undergoes further grafting onto the CMF substrate [70]. The peaks in the O 1s spectrum stem from two forms of oxygen: Si-O/C-O at 531.7 eV, and Si-O-Si at 532.5 eV, consistent with FT-IR results [67, 71]. The survey XPS spectrum (table 4. 1) indicates Si atomic composition of around 25% for both SCMF 1 and SCMF 2. These data are consistent with the atomic percent obtained from EDS.

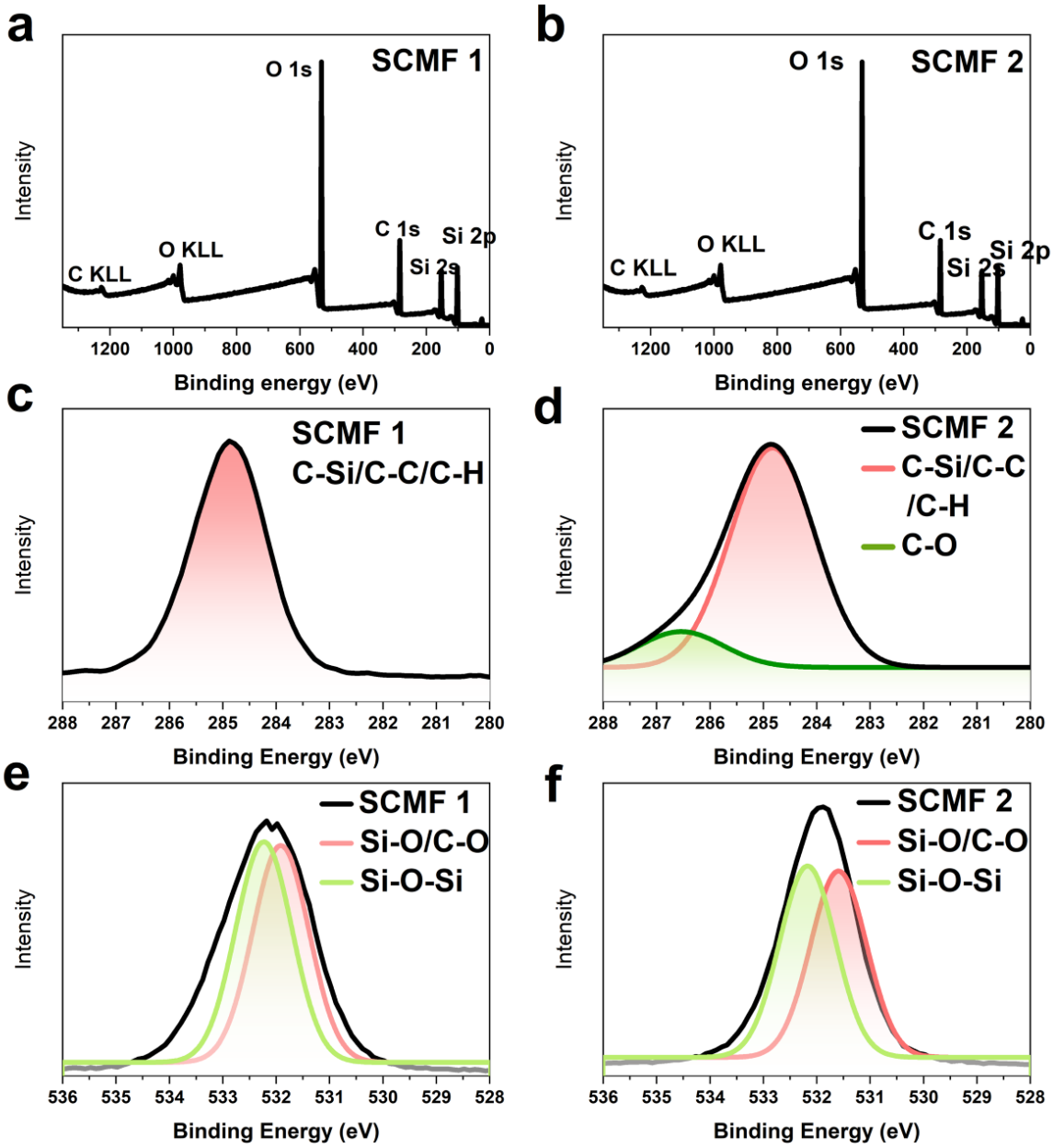

Figure 4. 4 XPS wide survey scan spectra of SCMF1 (a) and SCMF2 (b); XPS high-resolution scan of C 1*s* spectra of SCMF 1 (c) and SCMF 2 (d); XPS high-resolution scan of O 1s spectra of SCMF 1 (e) and SCMF 2 (f);

Table 4. 1 Atomic composition of SCMF 1 and SCMF 2 from XPS

Sample	Atomic composition (%) *		
	C 1s	**O 1s**	**Si 2p**
SCMF1	37.1±0.9	37.7±1.2	25.0±0.2
SCMF2	34.9±0.2	40.0±0.2	24.87±0.04

*The mean values and their respective standard deviations are derived as the arithmetic average of measurements collected from three distinct sampling regions.

The possible structure of SCMF 1 and SCMF 2 are presented in Scheme. 1 and the reactions are as follows [72].

For MTCS:

$$SiCl_3CH_3 + H_2O \rightarrow$$

$$SiCH_3(OH)_3 + cell - COOH \rightarrow cell - OOC - Si_xO_y(CH_3)_z - COO - cell \quad (7)$$

For TEOS:

$$2cell - COOH + Si(OEt)_4 \rightarrow cell - OOC - Si_xO_y(OEt)_z - COO - cell \quad (8)$$

("cell" stands for cellulose backbone, -Et stands for -CH_2CH_3)

Other possible reactions can happen as well. When silanes with hydrolyzable groups, such as chloride or alkoxide, mix with water, they create intermediate silanols which further react with

other silanols or the hydroxyl groups on the surface of solid materials. These reactions create a monolayer of silicone covalently linked to the surface, rendering it hydrophobic [73, 74]. Therefore, trace amounts of water in the film are desirable to hydrolyze MTCS or TEOS to form silanol, which further reacts with the hydroxyl groups on the surface of the CMF film to form new silanol. SiO_2 can also be introduced by hydrolysis of TEOS and the reactions are as follows [73, 74]:

$$2Si(OEt)_3OH \rightarrow (OEt)_3Si - O - Si(OEt)_3 + H_2O \rightarrow SiO_2 \quad (9)$$

$$Si(OEt)_4 + H_2O \rightarrow Si(OEt)_3OH + EtO \quad (10)$$

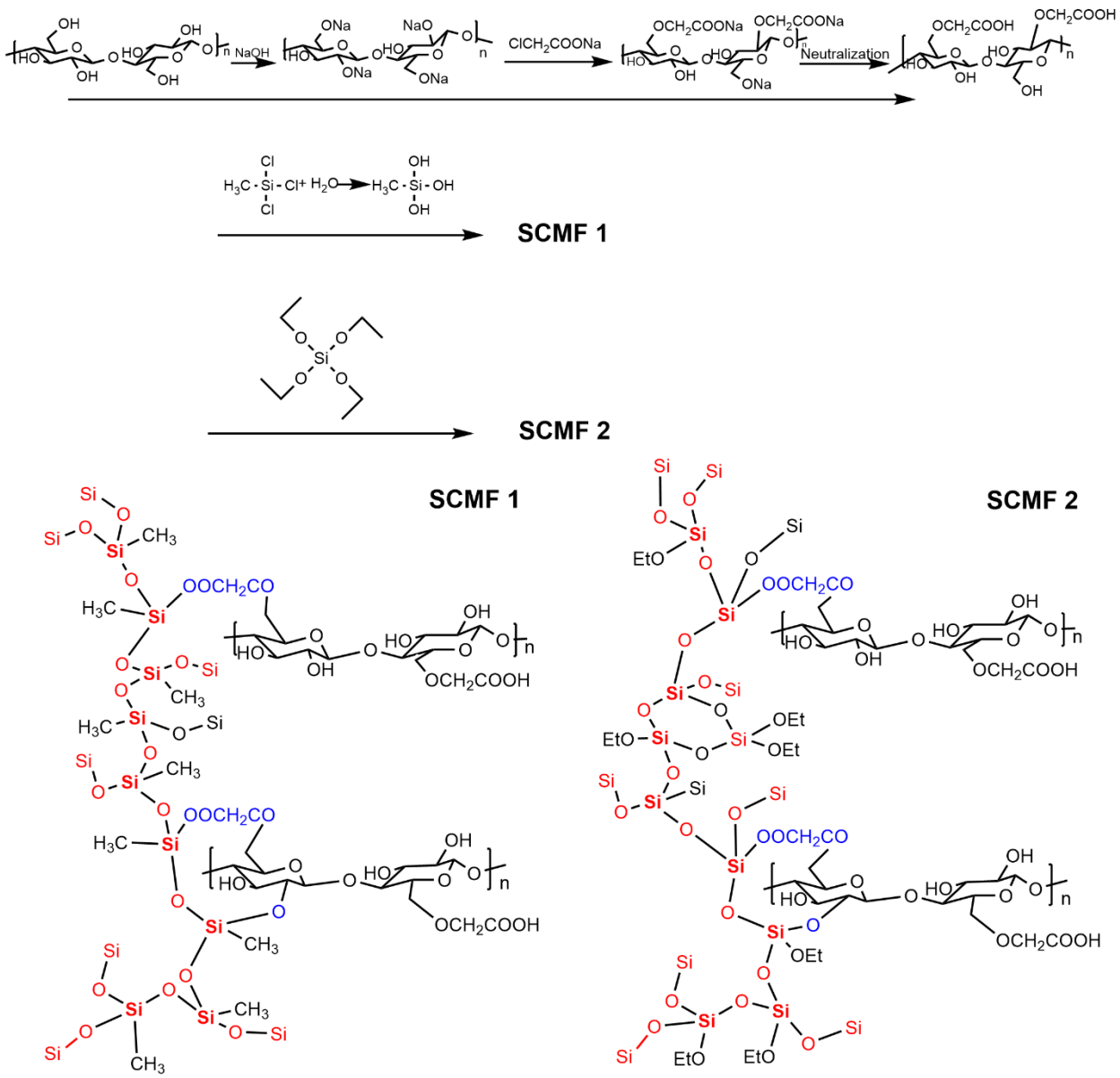

Scheme 4. 1 Schematic diagram of the carboxymethylation of cellulose and silanization of CMF.

The chloride group in MTCS serves as an excellent leaving group, significantly enhancing its reactivity [75, 76]. In fact, the chlorine atom in MTCS makes the silicon center more electrophilic, enhancing its reactivity toward nucleophiles like hydroxyl groups. In contrast, tetraethyl orthosilicate (TEOS) features of silicon atoms bonded to four ethoxy groups where the steric

hindrance fundamentally impacts the reactivity of these compounds [77]. Besides, TEOS's silicon atoms are less electrophilic due to the presence of ethoxy groups, making them less reactive towards OH groups.

4. 4. 4 Microstructure of CMF and SCMF Films

Figure 4. 5 shows SEM of the surface morphology of CMF films (a and b), SCMF2 (c and d), and SCMF 1 (e, f, and g). Moreover, the content of carbon, oxygen, and silicon atoms was determined by EDS, which can be used to quantify the occurrence of silanization. In the micrographs, the red, green, and yellow spots represent the position of carbon, oxygen, and silicon atoms, respectively. Observations from SEM reveal that CMF films exhibit a flat and smooth surface. However, upon surface modification, the surface morphology of SCMF2 (c and d) undergoes a notable transformation, becoming rougher and adorned with irregularly shaped particles. Conversely, SCMF1 (e, f, and g) exhibits the presence of spherical particles with sizes ranging from 100 nm to 1.3 μm. EDS analysis confirms these particles to be silica, further corroborating the successful silanization process.

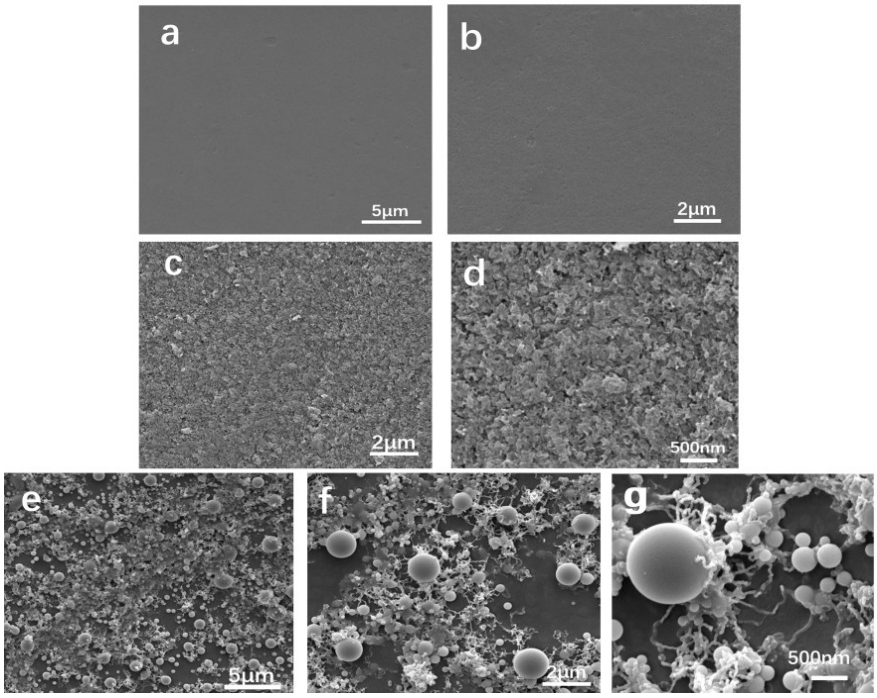

Figure 4. 5 FE-SEM images of films. a and b: CMF with scale bars of 5µm and 2 µm, respectively; c and d: SCMF 2 with scale bars of 2 µm and 500 nm, respectively. e, f and g: SCMF 1 film with scale bars of 5 µm, 2 µm and 500 nm.

Elemental mapping of SCMF 1 and SCMF 2 is shown in Figure 4. 6. For SMF 1, Si is uniformly distributed within the entire region. C and O, however, are conspicuously absent from the region occupied by large spherical particles are present. In contrast, for SCMF2, the three elements, C, O, and Si are uniformly distributed over the whole region. Therefore, SEM and EDS confirmed the successful surface modification of CMF film by silanization. The line scanning of the cross-section for SCMF 1 and SCMF 2 film further elucidates the distribution of Si, indicating its predominant

presence on the film surface. However, a small fraction of Si can penetrate the CMF film to a depth of approximately 5 μm for SCMF1 and about 2 μm for SCMF 2.

Table 4. 2 presents the weight and atomic percentage of C, O, and Si elements in SCMF 1 and SCMF 2. According to the table, there are 43% and 35% of weight % of Si in SCMF1 and SCMF 2, respectively. In the case of SCMF1, the Si content substantially dropped from 42.9 (wt)% to 21.03 (wt)% within a 5 μm distance from the surface. Only a minimal fraction of about 1.25 (wt)% of Si managed to infiltrate the film at a depth of approximately 5.3 μm. Meanwhile, for SCMF 2, 3.2% (wt%) of Si could permeate the CMF film. This phenomenon can be attributed to the with hydroxyl groups, which disrupts hydrogen bonding and weakens the film, facilitating further diffusion of MTCS molecules [75]. Additionally, the larger molecular size of TEOS with ethyl groups compared to MTCS renders it more challenging for TEOS to diffuse within the CMF film.

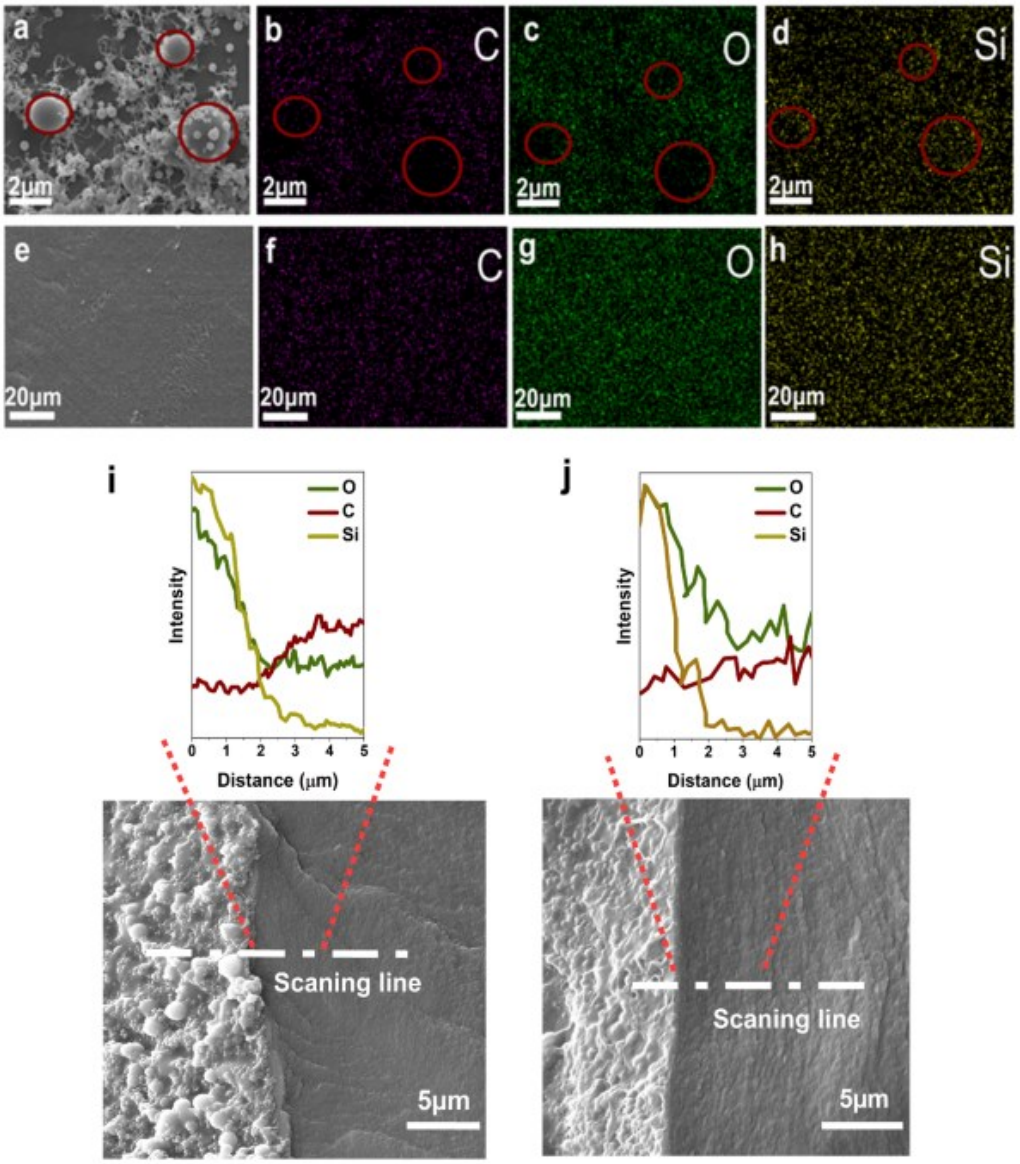

Figure 4. 6 SEM images for SCMF 1 (a) and SCMF 2 (e); Elemental mapping analysis showed C, O and Si atoms distributed for SCMF 1 (b, c and d) and SCMF 2 (f, g and h), respectively. Red circles show positions of large silica particles where carbon content is near zero. EDS line scan analysis for cross-sections of SCMF 1 (i) and SCMF 2 (j) showing the distribution of O, C and Si atoms along the black line (scanning line). The enlarged images show the intensity of O, C and Si atoms versus the distance from the surface along the scanning line.

Table 4. 2 Weight % and Atomic % for SCMF 1 and SCMF 2 at the surface and for various distances below the surface

Element	Weight % (CMF film)	Atomic % (CMF film)	Weight % (SCMF1)	Atomic % (SCMF1)	Weight % (SCMF2)	Atomic % (SCMF2)
C (surface)	57.3 ± 3.0	64.7 ± 2.6	18.2 ± 2.8	27.8 ± 2.8	17.6 ± 0.4	25.9 ± 0.4
O (surface)	41.3 ± 2.3	35.1± 2.5	38.1 ± 1.3	43.7 ± 1.2	47.4 ± 0.5	52.2 ± 0.4
Si (surface)	-	-	42.9 ± 2.5	28.0 ± 2.3	35.0 ± 0.4	22.0 ± 0.4
Si (~0.5µm)	-	-	21.0 ± 0.5	13.0 ± 0.5	3.2 ± 0.2	1.9 ± 0.3
Si (~1.5µm)	-	-	2.7 ± 0.3	1.4 ± 0.5	1.6 ± 0.3	0.8 ± 0.4
Si (~5.3µm)	-	-	1.3 ± 0.3	0.7 ± 0.4	0.7 ± 0.2	0.4 ± 0.3

MA (Moisture absorption) and WA (water absorption) of CMF, SCMF1, and SCMF2 are presented in Figure 4. 7. CMF films exhibit significant MA and WA values of approximately 60% and 139%, respectively. This is owing to the abundance of hydroxyl and carboxyl groups present on their surface. Following surface modification, the MA diminishes notably to 23% and 14% for SCMF1 and SCMF2, respectively. Correspondingly, WA exhibits a similar decreasing trend, attributable to the introduction of siloxane onto the CMF surface. With NMR it was proven that silanization occurs at the sites rich in hydrophilic carboxyl and hydroxyl groups. The grafting of methyl or ethyl groups facilitates the transformation of the surface from hydrophilic to hydrophobic, thereby contributing to the observed reduction in MA and WA values [78]. Wang et al [79] also observed a lower water adsorption of microcrystalline cellulose (MCC) after silanization.

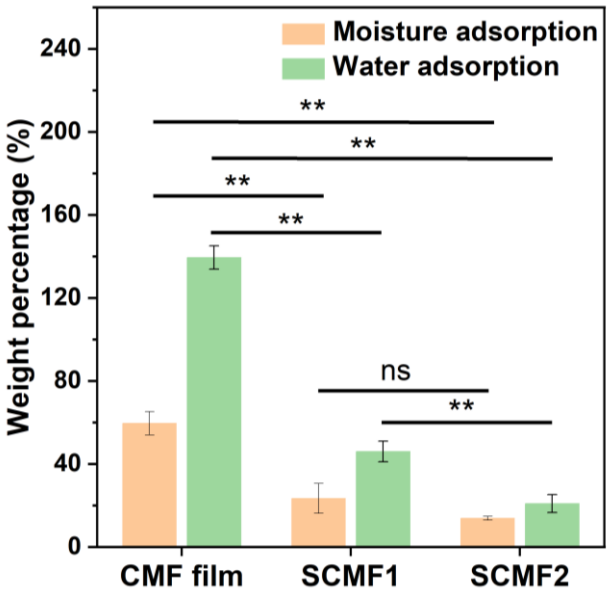

Figure 4. 7 Moisture absorption MA (orange bar) and water absorption WA (green bar) of CMF and SCMF films: SCMF1 and SCMF2. "ns" stands for no significant difference ($p \geq 0.05$), **: $p < 0.01$

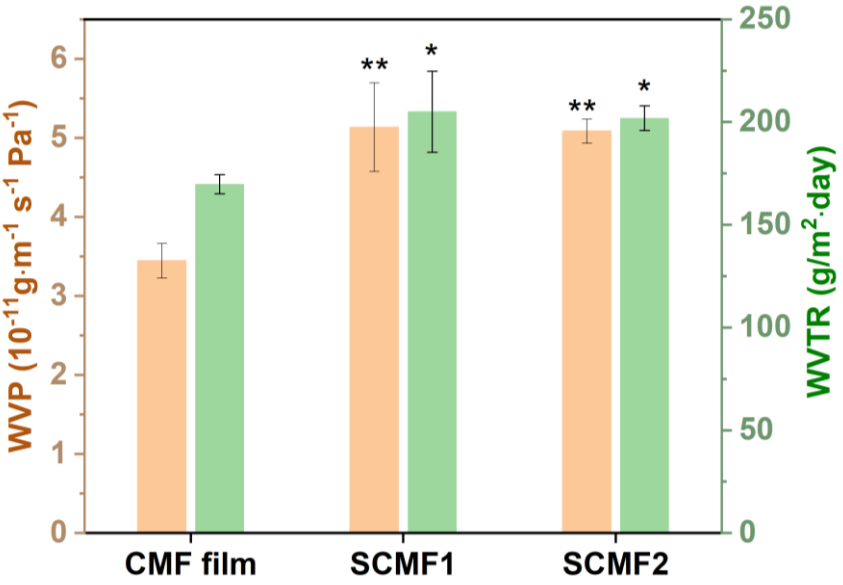

Figure 4. 8 WVP and WVTR of CMF and SCMF films. *: significant difference from CMF film, *: $p<0.05$; **: $p<0.01$. There is no significant difference between SCMF1 and SCMF2

Table 4. 3 Water Vapor permeation of common plastics and our films

Polymer	**WVP (10^{-11} g/m s Pa)**	**Ref**
Pullulan ester films	0.792-3.476	[80]
Bacterial cellulose	2.44-13.5	[81]
tapioca starch	~50	[82]
Corn starch	~33	[83]
methylcellulose	~8.5	[84]
Polystyrene (PS)	0.01-0.045	[85]
Polypropylene (PP)	0.0023-0.0046	[85]
Poly vinyl chloride (PVC)	0.071	[86]
Poly lactic acid (PLA)	3.52	[87]
Low-density polyethylene (LDPE)	0.055	[86]
High-density polyethylene (HDPE)	0.0017-0.0034	[84]
CMF	3.4 ± 0.2	This work

SCMF 1	5.1 ± 0.6	This work
SCMF 2	5.1 ± 0.1	This work

WVP of CMF, SCMF1, and SCMF2 are shown in Figure 4. 8. Water vapor barrier classification and water vapor permeation of common plastics are compiled in Tables S1 and 3. Among all the films, CMF exhibited the lowest water vapor permeation which is around 169 g/m^2 day. Following silanization, the WVP increased to 195 and 182 g/m^2 day for SCMF 1 and SCMF 2 after silanization, respectively. Even though the hydrophilic groups (-COOH and -OH) has been substituted by the silica and methyl/ethyl group, the inter- and intra-molecular hydrogen bonding network has been interrupted. Moreover, the porosity of CMF, SCMF 1 and SCMF 2 is found to be 7.8%, 21.9%, and 11.4%, respectively. When the thickness of CMF film in SCMF is assumed to be constant after silanization, the porosity of coated layer is calculated to be 56.7% and 33.6% for SCMF1 and SCMF2, respectively. This porosity of coated layer is underestimated as the silanization reaction primarily occurs at the surface with only a minor portion penetrating the film's interior. The pores in silanizated films enable small water molecules to permeate more easily. According to Table 4. 3, all three films show a low barrier to water compared to that of plastic films which limits their packaging applications to fruits and vegetables.

Despite the observed reduction in WVP compared to other materials like methylcellulose films, and starch films, CMF and SCMF films still demonstrate relatively low barrier properties, limiting their packaging applications primarily to fruits and vegetables. Furthermore, when compared to low-density polyethylene, CMF and SCMF films are not considered viable alternatives due to their comparatively higher permeability to water vapor.

4. 4. 5 Mechanical Properties of Films

Tensile stress, strain, and Young's modulus of different films are shown in Figure 4. 9. Because of the substantial presence of hydrogen bonding and the stacking interactions between the intra-layer and inter-layer of cellulose, the CMF film exhibited the highest Young's modulus and tensile stress. [55, 88].

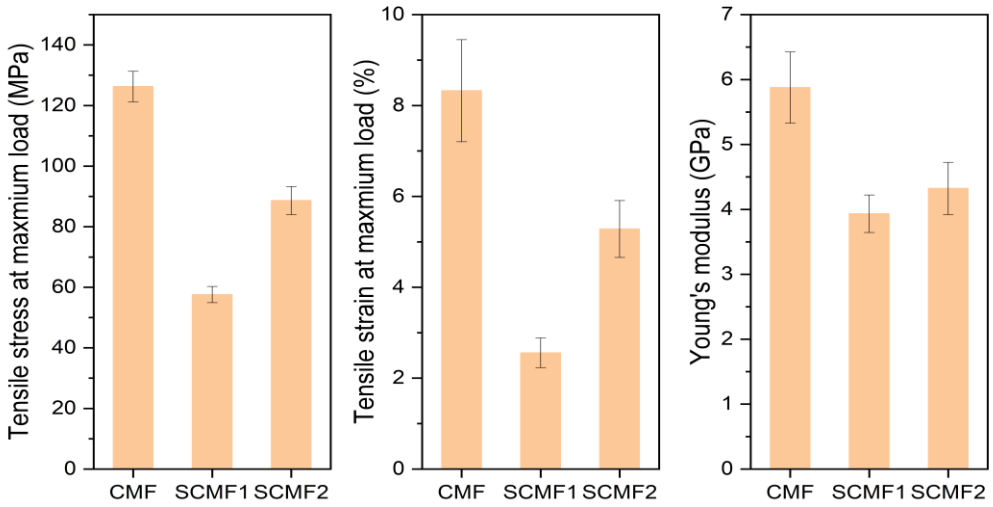

Figure 4. 9 Tensile stress at maximum load (left), Elongation at break (middle), and Young's modulus (right) of different films.

Table 4. 4 Mechanical Properties of conventional films in the packaging area

Films	Tensile stress (MPa)	Elongation at break (%)	Young's modulus (GPa)	Ref
PP	27-98	200-1000	2	[89]
Polyhydroxybutyrate (PHB)	35	10	1.7	[90]
polyvinyl alcohol PVA	25	149	2.3	[91]
PVC	24	124	0.83	[92]
Polyethylene terephthalate (PET)	59.6	5.2	2.5	[93]
LDPE	8-20	100-1000	0.3-0.5	[94]
HDPE	19-31	20-50	0.9	[89]
PLA	48-53	30-240	3.5	[94]
Polyvinylidene dichloride (PVDC)	49-98	0.2-0.6	10-40	[89]
PS	34-50	1.2-2.5	2.3-3.3	[94]
CMF	126 ± 5	8.3 ± 1.1	5.8 ± 0.6	This work
SCMF 1	58 ± 3	2.3 ± 0.3	4.0 ± 0.3	This work

Films	Tensile stress (MPa)	Elongation at break (%)	Young's modulus (GPa)	Ref
SCMF 2	89 ± 5	5.1 ± 0.6	4.3 ± 0.4	This work

The silanization has a discernible impact on the hydrogen bonding within CMF films, resulting in weakened mechanical properties. After the surface modification, Young's modulus decreased from 5.8 GPa to 4 GPa and 4.3 GPa for SCMF 1 and SCMF 2, respectively. The substitution of carboxyl and hydroxyl groups by siloxanes and methyl/ethyl groups disrupts hydrogen bonding and film strength. SCMF 2 showed higher tensile strengths than SCMF 1. The distinction can be attributed to the higher reactivity of MTCS, allowing it to penetrate deeper into the film and break more hydrogen bonds, thereby lowering the film strength as well as increasing its porosity. Similar results were observed by Huang et al [45], who showed that the tensile strength of regenerated cellulose film was decreased from ~66 MPa to ~42 MPa after chemical modification with organosilanes.

Evaluation against other polymeric materials presented in Table 4.4 indicates that SCMF films showed higher Young's modulus than PP, PHB, PVA, PVC, PET, LDPE, HDPE, PLA and PS, but lower than PVDC. Tensile can be competitive when compared to PET, PLA, PVDC, and PS. For elongation, SCMF films surpass PVDC, competing with PET and PS, but lower than other polymeric films listed in Table 4.

4. 4. 6 Water Contact Angle

The water contact angle (WCA) of CMF and SCMFs was recorded for times varying from 5 s to 30 min (Figure 4. 10). It has been reported that cellulose films have a WCA of about 45° [95]. In this study, a relatively higher WCA of 55° for the CMF film is attributed to roughness and the presence of micro-particles and nanorods that increase the roughness of the film (Figure 4. 5). Within 5 minutes, the WCA decreased gradually, reaching 0° after 30 minutes as the CMF film absorbed water, concurrently reducing the size of the water droplet. For SCMF 2, the WCA decreased from 73.5° to 50° within 30 min. Most importantly, the WCA for SCMF 1 remained constant at 131° after 30 min. The stability can be attributed to the increased presence of hydrophobic groups and enhanced surface roughness, particularly in SCMF 1, where the surface of films is covered with spherical particles as shown by SEM (Figure 4. 5). Moreover, the hydrophobic surface of SCMF films resulted in a slower spread of water droplets within 30 min due to the roughness of the film surface. It is widely acknowledged that the geometric structure of a surface is largely responsible for its hydrophilic and hydrophobic properties [96]. These findings unequivocally confirm the successful chemical modification of the CMF film surface, transforming SCMF 1 into a hydrophobic surface. The reduction in water droplet size over time is primarily due to evaporation, with minimal penetration occurring. As shown in the top right of the graphical abstract, the hydrophobic coating surface of SCMF1 is covered with micro- and nano-sized particles. These particles allow the WCA to be greater than 90^{o} so that the condensed water droplets can stick onto the curved surface. Because WCA > 90^{o}, very little penetration occurs in SCMF1 despite the large porosity. Lazzari et al [97] and Zhang et al [98] achieved a water contact angle of over 110° with methyltrimethoxysilane (MTMS) addition methods.

This value is close to that found by Jing et al. [41] for improved hydrophobic cellulose film obtained by silanization of cellulose and 3-aminopropyltriethoxysilane (APTES) by ball milling. Huang et al. [45] obtained a value of 109° for regenerated cellulose film vapor deposited by 1H,1H,2H,2H-perfluorooctyltriethoxysilane (PFTS).

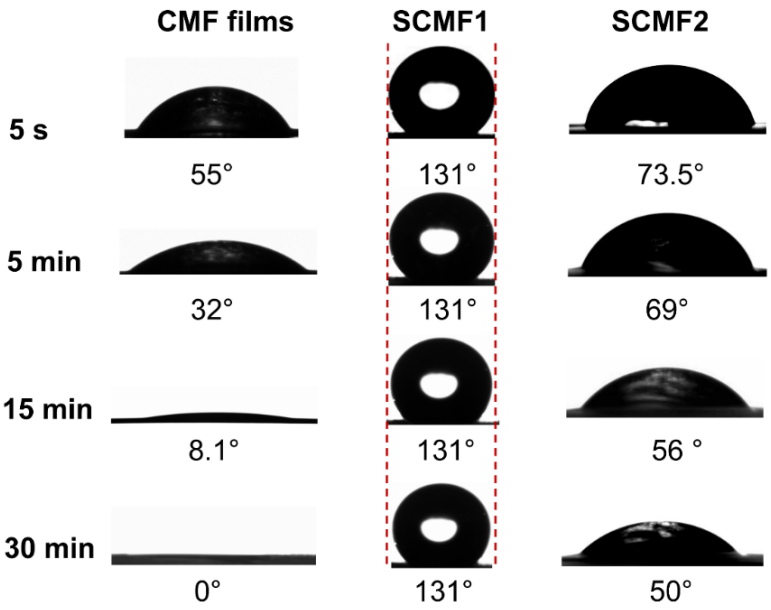

Figure 4. 10 Contact angle images for droplets of water of CMF, SCMF1, and SCMF2 film. All the tests are performed for 30 min. The water droplet images were collected in 5 s, 5 min, 15 min, and 30 min.

4. 4. 7 Anti-condensation/Breathability Measurement and Three-point Bending Test

Research indicates that the loss of stiffness and crispiness in French fried potatoes is primarily due to water absorption [2]. Anti-condensation tests were conducted for PE, CMF, SCMF 1 and SCMF 2 films using freshly prepared French fried potatoes from McDonald's. The French fried potatoes

were freshly prepared at McDonald's. The brittleness of the fries was determined by performing three-point bending tests immediately after preparation. Initially, the French fried potatoes exhibited crispiness and were easily breakable. As shown in Figure 4. 11, water vapor from the French fried potatoes started to condense on PE films and the French fried potatoes retained their brittleness for the initial 30 seconds. After 2 minutes, however, increased moisture accumulation owing to the waterproof nature of PE films, caused the fries to become wet and soft [2]. Images were taken for CMF and SCMF films at varying intervals ranging from 10 seconds to 21 minutes. The photographs from the three bending tests indicated that the fries were breakable within 13 minutes when covered by CMF, SCMF1, and SCMF2 films. Within 21 min, no droplet was observed on the CMF film, and the fries became partially bendable. This duration is significantly longer than when PE was used as a cover. This is attributed to the porosity and hydrophilicity of the CMF film, which allowed some moisture to transfer through the film while some was absorbed by it. In contrast, the French fried potatoes sealed by SCMF 1 and SCMF 2 were still breakable at 21 min. Notably, the degree of breakage observed in fries covered by SCMF1 and SCMF2 films was slightly greater than that of fries covered by CMF film. This suggests that the fries covered by SCMF1 and SCMF2 exhibited lower moisture content compared to those covered by CMF film.

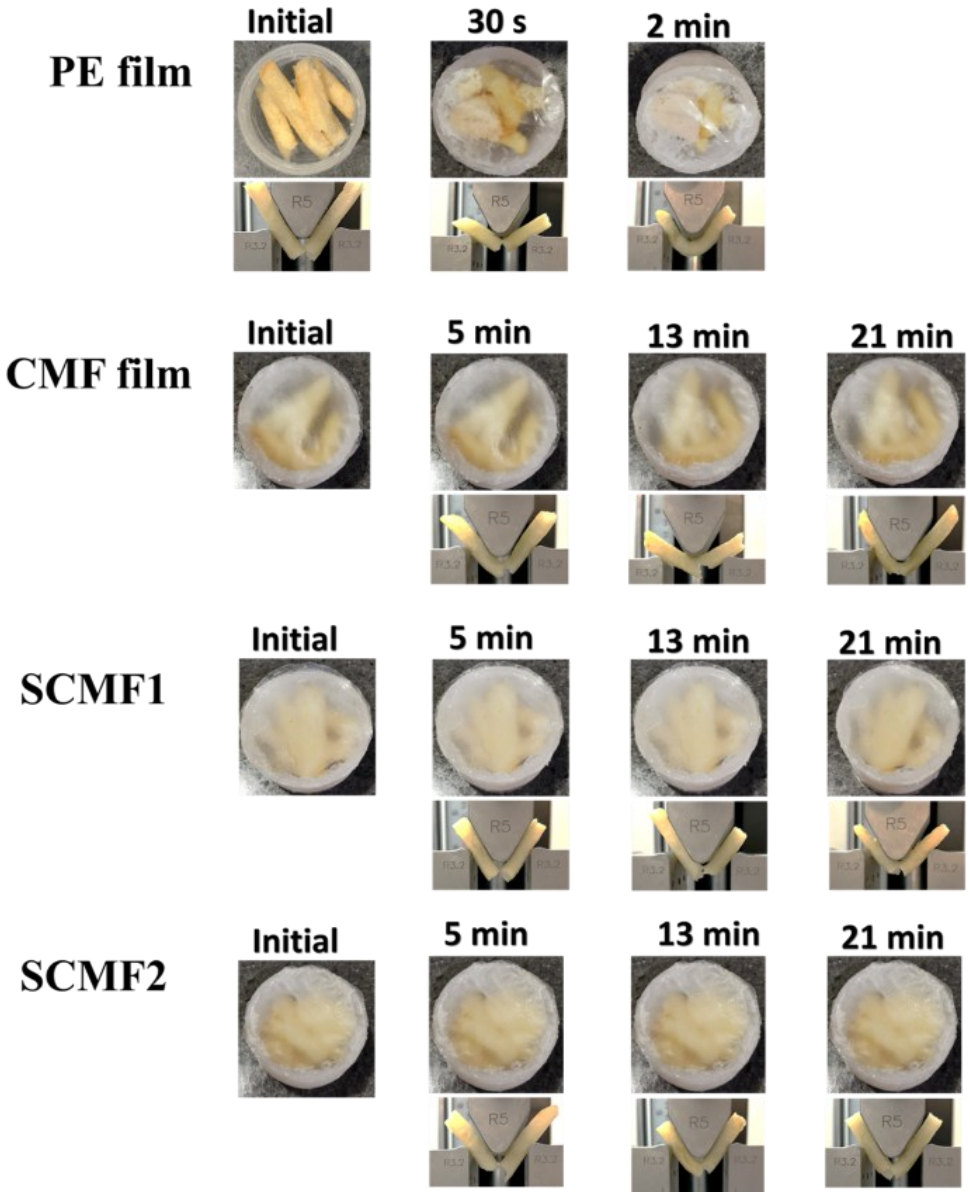

Figure 4. 11 Photographs for droplets of water appearing on PE, CMF, SCMF1, and SCMF2 films due to condensation (up), and photographs of French fried potatoes of three-point bending tests at breakage (lower). The photographs for French fried potatoes at initial conditions are the same for all the cases and only showed at the first case. All the tests were performed within 21 min. The images were collected at initial, 30s and 2 min for PE film and initial, 5 min, 13 min, and 21 min for the other films.

As illustrated in Figure 4. 12, the force versus deflection curves obtained from three-point bending tests demonstrate the mechanical behavior of French fries under varying conditions [99]. The force exhibited an increasing trend until the fries broke. Initially, the uncovered French fries displayed the highest force and steepest initial slope among all conditions, attributed to their optimal crispiness (Figure 4. 12a) [2, 87, 88]. In contrast, when the fries were coated with films, both the initial slope and the force at breakage (as indicated by the arrows) decreased over time. Notably, the deflection at breakage increased with time. This occurs because the films trap moisture, causing the fries to absorb water over time, resulting in increased softness and greater pliability [100]. Specifically, for fries covered with PE, the force at breakage decreased from approximately 3.1 N to about 2.5 N after 30 seconds of coverage. At 2 minutes, a plateau was observed, indicating that the fries became completely pliable. The maximum forces at breakage for fries covered by CMF films for 5, 13 and 21 min were approximately 2.5 N, 1.5 N, and 1.0 N, respectively. The fries covered with SCMF1 and SCMF2 maintained a relatively higher force at breakage compared to those coated with CMF films during the 21 min. This difference is likely due to the greater breathability of SCMF1 and SCMF2, which facilitate faster permeation of water vapor, thereby preserving the fries' crispiness. Among the films, the deflection at breakage was lowest for fries covered with SCMF1 after 5 minutes, indicating that these fries maintained superior crispiness. Moreover, the deflection at breakage for fries covered by SCMF1 and SCMF2 is less than that observed for fries covered by CMF films. This enhanced performance can be attributed to the higher breathability of SCMF1 compared to the other coatings.

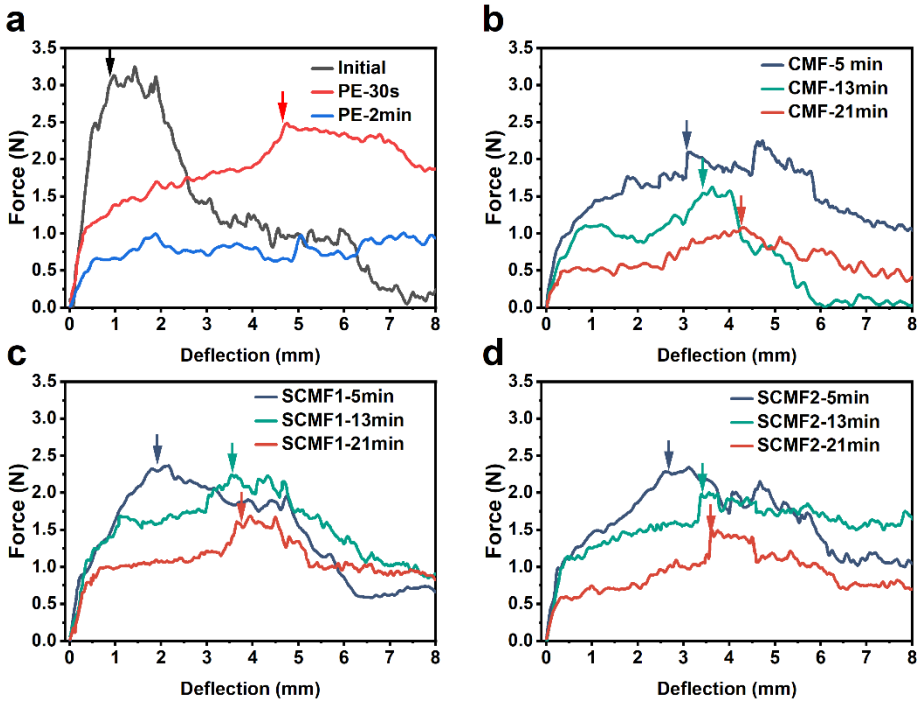

Figure 4. 12 Force vs deflection curves of three point bending test for French fried potatoes at (a) initial condition and covered by PE; (b) covered by CMF; (c) covered by SCMF1; (d) covered by SCMF2. (Arrows indicate the maximum force and deflection at the point of breakage)

An increased flexural modulus signifies a material with greater stiffness, demonstrating enhanced resistance to bending [102]. The flexural modulus of elasticity, depicted in Figure 4. 13, reveals that uncovered French fries exhibited the highest values. In contrast, fries coated with PE for 2 minutes showed a significant reduction to approximately 1.8 MPa. This decrease can be explained by the moisture retention caused by the PE coverage, which contributes to the softening of the fries. For fries covered with alternative films over a period of 5 minutes, the flexural modulus remained relatively consistent. However, after 21 minutes, fries coated with SCMF1 and SCMF2

displayed slightly higher flexural modulus values than those covered by CMF film. This finding suggests that the SCMF1 and SCMF2 coatings allowed for less moisture absorption compared to the CMF, thereby contributing to the mechanical integrity of the fries.

The results are consistent with the findings of Gleason [101], who reported that the elastic modulus of fries increases with prolonged frying times. This effect is attributed to the reduction in moisture content, which subsequently enhances the stiffness of the fries.

This improved property of SCMF films is attributed to the heightened porosity and hydrophobicity resulting from silanization, which effectively delayed the loss of crispiness in the French fries.

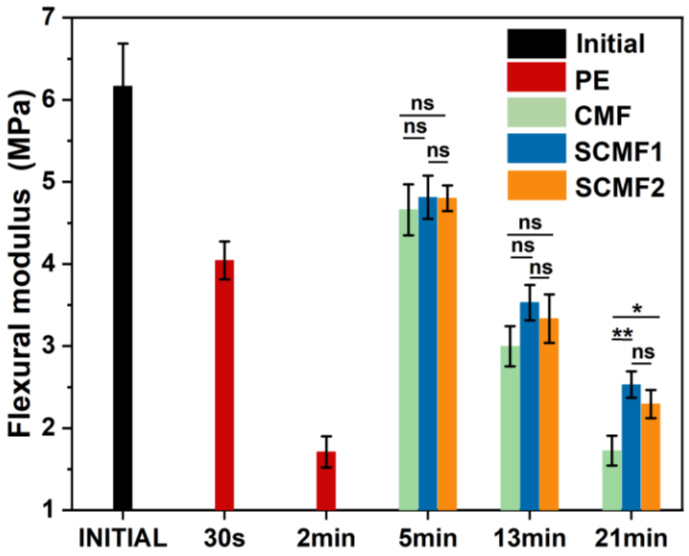

Figure 4. 13 Flexural modulus of elasticity of French fried potatoes at initial conditions, covered by PE for 30 s and 2 min, covered by CMF, SCMF1 and SCMF2 for 5, 13 and 21 min. "ns" stands for no significant difference ($p \geq 0.05$), *: $p < 0.05$, **: $p < 0.01$

4. 5 Conclusions

Silanized cellulose films were prepared from kraft pulp through a sequential process involving carboxylation and silanization. We successfully tailored the surface properties of the CMF films to exhibit enhanced water resistance and reduced hydrophilicity. Water contact angle measurements confirmed the hydrophobicity of SCMF 1 with its water contact angle increasing from 55° to 131° due to augmented surface roughness and hydrophobization. These modifications conferred improved anti-condensation properties, thereby extending the freshness of moisture-sensitive food products. SCMF1 and SCMF2 films exhibited superior breathability, preventing moisture accumulation and preserving the freshness of French fried potatoes for longer periods compared to PE and CMF films. This unique attribute makes films ideal for packaging perishable food by creating films that effectively inhibit condensation. This is achieved through the manipulation of film thickness, the porosity and the introduction of various quantities of carboxyl and siloxanes groups.

4. 6 References

[1] C. Chen, W. Sun, L. Wang, M. Tajvidi, J. Wang, D. J. Gardner, Transparent multifunctional cellulose nanocrystal films prepared using trivalent metal ion exchange for food packaging, ACS Sustainable Chemistry & Engineering 10(29) (2022) 9419-9430. https://doi.org/10.1021/acssuschemeng.2c01805

[2] M. L. Miranda, J. M. Aguilera, Structure and texture properties of fried potato products, Food Reviews International 22(2) (2006) 173-201. https://doi.org/10.1080/87559120600574584

[3] S. Finn, O. Condell, P. McClure, A. Amézquita, S. Fanning, Mechanisms of survival, responses and sources of Salmonella in low-moisture environments, Frontiers in microbiology 4 (2013) 331. https://doi.org/10.3389/fmicb.2013.00331

[4] Y. Liu, H. Fu, W. Zhang, H. Liu, Effect of crystalline structure on the catalytic hydrolysis of cellulose in subcritical water, ACS Sustainable Chemistry & Engineering 10(18) (2022) 5859-5866. https://doi.org/10.1021/acssuschemeng.1c08703

[5] M. Taherimehr, H. YousefniaPasha, R. Tabatabaeekoloor, E. Pesaranhajiabbas, Trends and challenges of biopolymer-based nanocomposites in food packaging, Comprehensive Reviews in Food Science and Food Safety 20(6) (2021) 5321-5344. https://doi.org/10.1111/1541-4337.12832

[6] A. Sobhan, K. Muthukumarappan, L. Wei, Biosensors and biopolymer-based nanocomposites for smart food packaging: Challenges and opportunities, Food Packaging and Shelf Life 30 (2021) 100745.

https://doi.org/10.1016/j.fpsl.2021.100745

[7] A. Jayakumar, K. Heera, T. Sumi, M. Joseph, S. Mathew, G. Praveen, I.C. Nair, E. Radhakrishnan, Starch-PVA composite films with zinc-oxide nanoparticles and phytochemicals as intelligent pH sensing wraps for food packaging application, International Journal of Biological Macromolecules 136 (2019) 395-403.

https://doi.org/10.1016/j.ijbiomac.2019.06.018

[8] G. Ariturk, C. Girisken, K. Bilge, C. Y. Kovanci, Y. Z. Menceloglu, S. A. Seven, Hybrid green composites of PLA incorporated with upcycled waste cellulose and vermiculite, European Polymer Journal 203 (2024) 112667.

https://doi.org/10.1016/j.eurpolymj.2023.112667

[9] A.H. Bedane, M. Eić, M. Farmahini-Farahani, H. Xiao, Water vapor transport properties of regenerated cellulose and nanofibrillated cellulose films, Journal of Membrane Science 493 (2015) 46-57.

https://doi.org/10.1016/j.memsci.2015.06.009

[10] N. L. Mai, Y.-M. Koo, Computer-aided design of ionic liquids for high cellulose dissolution, ACS Sustainable Chemistry & Engineering 4(2) (2016) 541-547.

https://doi.org/10.1021/acssuschemeng.5b00958

[11] G. Cabrera-Barjas, L. Becheran, O. Valdés, A. Giordano, R. Segura-del Río, G. Bravo-Arrepol, E.F. Durán-Lara, J. Cea, A. Berg, J. Castaño, Effect of cellulose nanofibrils on vancomycin drug release from chitosan nanocomposite films, European Polymer Journal 197 (2023) 112371.

https://doi.org/10.1016/j.eurpolymj.2023.112371

[12] A. Okugawa, Y. Yuguchi, D. Hayakawa, F. Ueno, K. Hatai, C. Yamane, Oxygen permeability of regenerated cellulose films with different water regains, Carbohydrate Polymers (2023) 120849.
https://doi.org/10.1016/j.carbpol.2023.120849

[13] Y. Zhang, F. Jiang, W. Zhao, L. Fu, C. Xu, B. Lin, One-pot synthesis of degradable and renewable cellulose-based packaging films, ACS Sustainable Chemistry & Engineering 10(50) (2022) 16871-16881.
https://doi.org/10.1021/acssuschemeng.2c05440

[14] J. Wang, D. J. Gardner, N. M. Stark, D. W. Bousfield, M. Tajvidi, Z. Cai, Moisture and oxygen barrier properties of cellulose nanomaterial-based films, ACS Sustainable Chemistry & Engineering 6(1) (2018) 49-70.
https://doi.org/10.1021/acssuschemeng.7b03523

[15] T. Erceg, N. Vukić, O. Šovljanski, A. Stupar, V. Šergelj, M. Aćimović, S. Baloš, J. Ugarković, D. Šuput, S. Popović, Characterization of films based on cellulose acetate/poly (caprolactone diol) intended for active packaging prepared by green chemistry principles, ACS Sustainable Chemistry & Engineering 10(28) (2022) 9141-9154. https://doi.org/10.1021/acssuschemeng.2c02009

[16] A. I. Quilez-Molina, U. Chandra Paul, D. Merino, A. Athanassiou, Composites of Thermoplastic Starch and Lignin-Rich Agricultural Waste for the Packaging of Fatty Foods, ACS Sustainable Chemistry & Engineering 10(47) (2022) 15402-15413. https://doi.org/10.1021/acssuschemeng.2c04326

[17] Z. Zhou, J. Yang, M. Wu, P. Lu, X. Song, CO2 Escaping In Situ Endowed the Antimicrobial Nanocellulose Packaging Film with a Microporous Structure, ACS Sustainable Chemistry & Engineering (2023).
https://doi.org/10.1021/acssuschemeng.3c00310

[18] L. Amoroso, K. J. De France, C. I. Milz, G. Siqueira, T. Zimmermann, G. Nystrom, Sustainable cellulose nanofiber films from carrot pomace as sprayable coatings for food packaging applications, ACS Sustainable Chemistry & Engineering 10(1) (2021) 342-352.
https://doi.org/10.1021/acssuschemeng.1c06345

[19] R. L. Gardas, J. A. Coutinho, A group contribution method for viscosity estimation of ionic liquids, Fluid Phase Equilibria 266(1-2) (2008) 195-201.
https://doi.org/10.1016/j.fluid.2008.01.021

[20] Y. Meng, Z. Pang, C. Dong, Enhancing cellulose dissolution in ionic liquid by solid acid addition, Carbohydrate Polymers 163 (2017) 317-323.
https://doi.org/10.1016/j.carbpol.2017.01.085

[21] S. Acharya, S. Liyanage, P. Parajuli, S. S. Rumi, J. L. Shamshina, N. Abidi, Utilization of cellulose to its full potential: a review on cellulose dissolution, regeneration, and applications, Polymers 13(24) (2021) 4344.
https://doi.org/10.3390/polym13244344

[22] D. Kasprzak, E. Krystkowiak, I. Stępniak, M. Galiński, Dissolution of cellulose in novel carboxylate-based ionic liquids and dimethyl sulfoxide mixed solvents, European Polymer Journal 113 (2019) 89-97.
https://doi.org/10.1016/j.eurpolymj.2019.01.053

[23] T. Erdmenger, C. Haensch, R. Hoogenboom, U.S. Schubert, Homogeneous tritylation of cellulose in 1-butyl-3-methylimidazolium chloride, Macromolecular bioscience 7(4) (2007) 440-445. https://doi.org/10.1002/mabi.200600253

[24] A. Harlin, Cellulose carbamate: production and applications, (2019). 10.32040/2019.978-951-38-8707-0

[25] S.C. Gondhalekar, P.J. Pawar, S.S. Dhumal, S.S. Thakre, Mechanism of xanthation reaction in viscose process, Cellulose 26 (2019) 1595-1604. https://doi.org/10.1007/s10570-018-2213-5

[26] M. Weißl, M.A. Hobisch, L.S. Johansson, K. Hettrich, E. Kontturi, B. Volkert, S. Spirk, Cellulose carbamate derived cellulose thin films: preparation, characterization and blending with cellulose xanthate, Cellulose 26 (2019) 7399-7410. https://doi.org/10.1007/s10570-019-02600-z

[27] S. Paunonen, Strength and barrier enhancements of cellophane and cellulose derivative films: a review, BioResources 8(2) (2013) 3098-3121. https://hdl.handle.net/11250/2657359

[28] V. D. Alves, N. Costa, I. M. Coelhoso, Barrier properties of biodegradable composite films based on kappa-carrageenan/pectin blends and mica flakes, Carbohydrate Polymers 79(2) (2010) 269-276. https://doi.org/10.1016/j.carbpol.2009.08.002

[29] D. A. Iryani, N. M. Risthy, D. A. Resagian, S. D. Yuwono, U. Hasanudin, Preparation and evaluation adsorption capacity of cellulose xanthate of sugarcane bagasse for removal heavy metal ion from aqueous solutions, IOP Conference Series: Earth and Environmental Science, IOP Publishing, 2017, p. 012039. 10.1088/1755-1315/65/1/012039

[30] M. Moradian, Md S. Islam, T. G. M. van de Ven, Insoluble regenerated cellulose films made from mildly carboxylated dissolving and kraft pulps, Industrial & Engineering Chemistry Research 60(15) (2021) 5385-5393.
https://doi.org/10.1021/acs.iecr.1c00485

[31] M. Moradian, N. Alam, T. G. M. van de Ven, Influence of carboxyl charge density on properties of extruded cellulose films, Industrial & Engineering Chemistry Research 60(38) (2021) 13756-13763.
https://doi.org/10.1021/acs.iecr.1c01716

[32] M. Moradian, H. Wiebe, T. G. M. van de Ven, Ultrathin ultrastrong transparent films made from regenerated cellulose and epichlorohydrin, Carbohydrate Polymers (2023) 121131. https://doi.org/10.1016/j.carbpol.2023.121131

[33] C. Aulin, M. Gällstedt, T. Lindström, Oxygen and oil barrier properties of microfibrillated cellulose films and coatings, Cellulose 17(3) (2010) 559-574.
https://doi.org/10.1007/s10570-009-9393-y

[34] Y. Liang, Y. Yao, Y. Liu, Y. Li, C. Xu, L. Fu, B. Lin, Curcumin-loaded HKUST-1@ carboxymethyl starch-based composites with moisture-responsive release properties and synergistic antibacterial effect for perishable fruits, International journal of biological macromolecules 214 (2022) 181-191.
https://doi.org/10.1016/j.ijbiomac.2022.06.022

[35] X. Y. Tang, Z. Liu, R. Xie, X. J. Ju, W. Wang, L. Y. Chu, Humidity-Responsive Actuators Based on Firm Heterojunction of Glycerol-Cross-linked Polyvinyl Alcohol and Porous Polyvinylidene Fluoride as Smart Gates for Anti-condensation, Industrial & Engineering Chemistry Research 61(23) (2022) 8101-8111.

https://doi.org/10.1021/acs.iecr.2c01289

[36] K. Huang, R. Sun, J. Wang, X. Shi, H. Lei, Anti-Condensation Performance of a New Superhydrophobic Coating for Pavements, Materials 16(17) (2023) 5793.

https://doi.org/10.3390/ma16175793

[37] X. Wu, F. Yang, G. Lu, X. Zhao, Z. Chen, S. Qian, A breathable and environmentally friendly superhydrophobic coating for anti-condensation applications, Chemical Engineering Journal 412 (2021) 128725.

https://doi.org/10.1016/j.cej.2021.128725

[38] X. Wu, K. Wang, J. Zhang, X. Jie, Z. Chen, Y. Lai, A polyester-silica anti-condensation surface with anti-fouling property, Chemical Engineering Journal 440 (2022) 135934. https://doi.org/10.1016/j.cej.2022.135934

[39] Y. Pan, F. Wang, T. Wei, C. Zhang, H. Xiao, Hydrophobic modification of bagasse cellulose fibers with cationic latex: Adsorption kinetics and mechanism, Chemical Engineering Journal 302 (2016) 33-43.

https://doi.org/10.1016/j.cej.2016.05.022

[40] M. Z. Yao, Y. Liu, C. N. Qin, X. J. Meng, B. X. Cheng, H. Zhao, S. F. Wang, Z. Q. Huang, Facile fabrication of hydrophobic cellulose-based organic/inorganic nanomaterial modified with POSS by plasma treatment, Carbohydrate Polymers 253 (2021) 117193. https://doi.org/10.1016/j.carbpol.2020.117193

[41] M. Jing, L. Zhang, Z. Fan, X. Liu, Y. Wang, C. Liu, C. Shen, Markedly improved hydrophobicity of cellulose film via a simple one-step aminosilane-assisted ball milling, Carbohydrate Polymers 275 (2022) 118701.

https://doi.org/10.1016/j.carbpol.2021.118701

[42] C. Zhang, P. Zhang, L. Cheng, J. Li, R. Jian, M. Ji, F. Li, A strong, hydrophobic, transparent and biodegradable nano-lignocellulosic membrane from wheat straw by novel strategy, Journal of Cleaner Production 356 (2022) 131879.
https://doi.org/10.1016/j.jclepro.2022.131879

[43] J.A. Sirviö, M. Visanko, O. Laitinen, A. Ämmälä, H. Liimatainen, Amino-modified cellulose nanocrystals with adjustable hydrophobicity from combined regioselective oxidation and reductive amination, Carbohydrate polymers 136 (2016) 581-587. https://doi.org/10.1016/j.carbpol.2015.09.089

[44] C. Qiu, H. Liu, K. Shen, M. Yuan, H. Qi, Rational design of stable fluorescent and hydrophobic cellulose-based film for full-band UV-blocking, Cellulose 29(18) (2022) 9719-9729. https://doi.org/10.1007/s10570-022-04853-7

[45] K. Huang, A. Maltais, Y. Wang, Enhancing water resistance of regenerated cellulose films with organosilanes and cellulose nanocrystals for food packaging, Carbohydrate Polymer Technologies and Applications 6 (2023) 100391.
https://doi.org/10.1016/j.carpta.2023.100391

[46] Q. Chen, D. Ying, Y. Chen, H. Xie, H. Zhang, C. Chang, Highly transparent, hydrophobic, and durable anisotropic cellulose films as electronic screen protectors, Carbohydrate Polymers 311 (2023) 120735.
https://doi.org/10.1016/j.carbpol.2023.120735

[47] T. Yun, J. Du, X. Ji, Y. Tao, Y. Cheng, Y. Lv, J. Lu, H. Wang, Waterproof and ultrasensitive paper-based wearable strain/pressure sensor from carbon black/multilayer graphene/carboxymethyl cellulose composite, Carbohydrate Polymers (2023). https://doi.org/10.1016/j.carbpol.2023.120898

[48] X. Tian, M. Wu, Z. Wang, J. Zhang, P. Lu, A high-stable soybean-oil-based epoxy acrylate emulsion stabilized by silanized nanocrystalline cellulose as a sustainable paper coating for enhanced water vapor barrier, Journal of Colloid and Interface Science 610 (2022) 1043-1056. https://doi.org/10.1016/j.jcis.2021.11.149

[49] G.-H. Kim, D.-H. Kang, B.-N. Jung, J.-K. Shim, Fabrication and characterization of hydrophobic cellulose nanofibrils/silica nanocomposites with hexadecyltrimethoxysilane, Polymers 14(4) (2022) 833.
https://doi.org/10.3390/polym14040833

[50] L. Yu, Z. Zhang, H. Tang, J. Zhou, Fabrication of hydrophobic cellulosic materials via gas–solid silylation reaction for oil/water separation, Cellulose 26 (2019) 4021-4037. https://doi.org/10.1007/s10570-019-02355-7

[51] T. G. M. van de Ven, M. N. Alam, J. P. Lumb, M. S. Islam, M. Moradian, Cellulose-based filaments, films and 3D objects and methods of manufacture thereof, PCT/CA2022/050599, WO 2022/221945 A1, Oct. 27, 2022.

[52] Z. Tang, H. Li, D. W. Hess, V. Breedveld, Effect of chain length on the wetting properties of alkyltrichlorosilane coated cellulose-based paper, Cellulose 23 (2016) 1401-1413. https://doi.org/10.1007/s10570-016-0877-2

[53] A. Ashori, S. Sheykhnazari, T. Tabarsa, A. Shakeri, M. Golalipour, Bacterial cellulose/silica nanocomposites: Preparation and characterization, Carbohydrate Polymers 90(1) (2012) 413-418. https://doi.org/10.1016/j.carbpol.2012.05.060

[54] H. Yang, A. Tejado, N. Alam, M. Antal, T.G.M. van de Ven, Films prepared from electrosterically stabilized nanocrystalline cellulose, Langmuir 28(20) (2012) 7834-7842. https://doi.org/10.1021/la2049663

[55] M. Yadav, Y. K. Liu, F. C. Chiu, Fabrication of cellulose nanocrystal/silver/alginate bionanocomposite films with enhanced mechanical and barrier properties for food packaging application, Nanomaterials 9(11) (2019) 1523. https://doi.org/10.3390/nano9111523

[56] M. Yadav, F. C. Chiu, Cellulose nanocrystals reinforced κ-carrageenan based UV resistant transparent bionanocomposite films for sustainable packaging applications, Carbohydrate polymers 211 (2019) 181-194.
https://doi.org/10.1016/j.carbpol.2019.01.114

[57] H. Sehaqui, Q. Zhou, O. Ikkala, L.A. Berglund, Strong and tough cellulose nanopaper with high specific surface area and porosity, Biomacromolecules 12(10) (2011) 3638-3644. https://doi.org/10.1021/bm2008907

[58] ASTM D790-17; Standard Test Methods for Flexural Properties of Unreinforced and Reinforced Plastics and Electrical Insulating Materials. American Society for Testing and Materials: Philadelphia, PA, USA, 2017.

[59] A. Zandinejad, O. Das, A. B. Barmak, M. Kuttolamadom, M. Revilla-León, The flexural strength and flexural modulus of stereolithography additively manufactured zirconia with different porosities, Journal of Prosthodontics 31(5) (2022) 434-440. https://doi.org/10.1111/jopr.13430

[60] C. K. Choi, Comparison between SiOC Thin Film by plasma enhance chemical vapor deposition and SiO2 Thin Film by Fourier Transform Infrared Spectroscopy, Journal of the Korean Physical Society 56(4) (2010) 1150-1155.
https://doi.org/10.3938/jkps.56.1150

[61] P. J. Launer, B. Arkles, Infrared analysis of organosilicon compounds: spectra-structure correlations, Silicone compounds register and review 100 (1987).

[62] J. Jo, H. Kim, S. Y. Jeong, C. Park, H. S. Hwang, B. Koo, Changes in mechanical properties of polyhydroxyalkanoate with double silanized cellulose nanocrystals using different organosiloxanes, Nanomaterials 11(6) (2021) 1542.
https://doi.org/10.3390/nano11061542

[63] L. Dashairya, D. D. Barik, P. Saha, Methyltrichlorosilane functionalized silica nanoparticles-treated superhydrophobic cotton for oil–water separation, Journal of Coatings Technology and Research 16(4) (2019) 1021-1032.
https://doi.org/10.1007/s11998-018-00177-z

[64] R. Yang, Y. Liang, S. Hong, S. Zuo, Y. Wu, J. Shi, L. Cai, J. Li, H. Mao, S. Ge, Novel low-temperature chemical vapor deposition of hydrothermal delignified wood for hydrophobic property, Polymers 12(8) (2020) 1757.
https://doi.org/10.3390/polym12081757

[65] R. H. Glaser, G. L. Wilkes, C.E. Bronnimann, Solid-state 29Si NMR of TEOS-based multifunctional sol-gel materials, Journal of non-crystalline solids 113(1) (1989) 73-87. https://doi.org/10.1016/0022-3093(89)90320-7

[66] R. Motta Neves, H. L. Ornaghi Jr, B. Duchemin, A. J. Zattera, S. Campos Amico, Grafting amount and structural characteristics of microcrystalline cellulose functionalized with different aminosilane contents, Cellulose 29(6) (2022) 3209-3224. https://doi.org/10.1007/s10570-022-04484-y

[67] J. Banaś, U. Lelek-Borkowska, M. Starowicz, Electrochemical behaviour of p-Si in methanol solutions of chlorides, Journal of Solid State Electrochemistry 8 (2004) 422-429. https://doi.org/10.1007/s10008-003-0475-8

[68] Y. Zhang, L. Zhu, L. Chen, L. Liu, G. Ye, Influence of magnesia on demoulding strength of colloidal silica-bonded castables, Reviews on Advanced Materials Science 58(1) (2019) 32-37. https://doi.org/10.1515/rams-2019-0008

[69] B. P. Frank, D. P. Durkin, E. R. Caudill, L. Zhu, D. H. White, M. L. Curry, J. A. Pedersen, D. H. Fairbrother, Impact of silanization on the structure, dispersion properties, and biodegradability of nanocellulose as a nanocomposite filler, ACS Applied Nano Materials 1(12) (2018) 7025-7038.
https://doi.org/10.1021/acsanm.8b01819

[70] S. Zhao, Z. Chen, Y. Dong, W. Lu, D. Zhu, The Preparation and Properties of Composite Hydrogels Based on Gelatin and (3-Aminopropyl) Trimethoxysilane Grafted Cellulose Nanocrystals Covalently Linked with Microbial Transglutaminase, Gels 8(3) (2022) 146. https://doi.org/10.3390/gels8030146

[71] P. Post, L. Wurlitzer, W. Maus-Friedrichs, A. P. Weber, Characterization and applications of nanoparticles modified in-flight with silica or silica-organic coatings, Nanomaterials 8(7) (2018) 530. https://doi.org/10.3390/nano8070530

[72] L. Zhang, Q. Zhang, J. Yu, J. Ma, Z. Wang, Y. Fan, S. Kuga, Strengthened cellulosic gels by the chemical gelation of cellulose via crosslinking with TEOS, Cellulose 26(18) (2019) 9819-9829. https://doi.org/10.1007/s10570-019-02765-7

[73] G. R. J. Artus, S. Jung, J. Zimmermann, H. P. Gautschi, K. Marquardt, S. Seeger, Silicone nanofilaments and their application as superhydrophobic coatings, Advanced Materials 18(20) (2006) 2758-2762.
https://doi.org/10.1002/adma.200502030

[74] W. Jiang, C. Sun, Y. Zhang, Z. Xie, J. Zhou, J. Kang, Y. Cao, M. Xiang, Preparation of well-dispersed graphene oxide-silica nanohybrids/poly (lactic acid) composites by melt mixing, Polymer Testing 118 (2023) 107912.
https://doi.org/10.1016/j.polymertesting.2022.107912

[75] E. G. Atici, E. Kasapgil, I. Anac, H. Y. Erbil, Methyltrichlorosilane polysiloxane filament growth on glass using low cost solvents and comparison with gas phase reactions, Thin Solid Films 616 (2016) 101-110.
https://doi.org/10.1016/j.tsf.2016.07.041

[76] B. Xie, L. Choate, A. Muscat, Repair and capping of porous MSQ films using chlorosilanes and supercritical CO2, Microelectronic Engineering 80 (2005) 349-352. https://doi.org/10.1016/j.mee.2005.04.090

[77] F. Xu, W. Zeng, D. Li, Recent advance in alkoxysilane-based consolidants for stone, Progress in organic coatings 127 (2019) 45-54.
https://doi.org/10.1016/j.porgcoat.2018.11.003

[78] M. Gorbounov, P. Halloran, S. M. Soltani, Hydrophobic and hydrophilic functional groups and their impact on physical adsorption of CO2 in presence of H2O: A critical review, Journal of CO_2 Utilization 86 (2024) 102908.
https://doi.org/10.1016/j.jcou.2024.102908

[79] X. Wang, S. Xu, Y. Tan, J. Du, J. Wang, Synthesis and characterization of a porous and hydrophobic cellulose-based composite for efficient and fast oil–water separation, Carbohydrate polymers 140 (2016) 188-194.
https://doi.org/10.1016/j.carbpol.2015.12.028

[80] B. Niu, P. Shao, H. Chen, P. Sun, Structural and physiochemical characterization of novel hydrophobic packaging films based on pullulan derivatives for fruits preservation, Carbohydrate Polymers 208 (2019) 276-284.

[81] P. Cazón, G. Velázquez, M. Vázquez, Bacterial cellulose films: Evaluation of the water interaction, Food Packaging and Shelf Life 25 (2020) 100526.

[82] N. Tamimi, A. Mohammadi Nafchi, H. Hashemi-Moghaddam, H. Baghaie, The effects of nano-zinc oxide morphology on functional and antibacterial properties of tapioca starch bionanocomposite, Food Science & Nutrition 9(8) (2021) 4497-4508.

[83] M. A. Bertuzzi, E. C. Vidaurre, M. Armada, J. Gottifredi, Water vapor permeability of edible starch based films, Journal of food engineering 80(3) (2007) 972-978.

[84] I. G. Donhowe, O. Fennema, The effects of plasticizers on crystallinity, permeability, and mechanical properties of methylcellulose films, Journal of Food Processing and preservation 17(4) (1993) 247-257.

[85] S. Y. Sung, L. T. Sin, T. T. Tee, S. T. Bee, A. Rahmat, W. Rahman, A.-C. Tan, M. Vikhraman, Antimicrobial agents for food packaging applications, Trends in Food Science & Technology 33(2) (2013) 110-123.

[86] N. T. Nemet, V. M. Šošo, V. L. Lazić, Effect of glycerol content and pH value of film-forming solution on the functional properties of protein-based edible films, Acta Periodica Technologica (41) (2010) 57-67.

[87] E. P. Díaz-Galindo, A. Nesic, G. Cabrera-Barjas, O. Dublan-García, R. I. Ventura-Aguilar, F. J. Vázquez-Armenta, S. Aguilar-Montes de Oca, C. Mardones, J.F. Ayala-Zavala, Physico-chemical and antiadhesive properties of poly (lactic acid)/grapevine cane extract films against food pathogenic microorganisms, Polymers 12(12) (2020) 2967.

[88] R. Parthasarathi, G. Bellesia, S. P. S. Chundawat, B. E. Dale, P. Langan, S. Gnanakaran, Insights into hydrogen bonding and stacking interactions in cellulose, The Journal of Physical Chemistry A 115(49) (2011) 14191-14202.
https://doi.org/10.1021/jp203620x

[89] L. Bastarrachea, S. Dhawan, S. S. Sablani, Engineering properties of polymeric-based antimicrobial films for food packaging: a review, Food Engineering Reviews 3(2) (2011) 79-93.
https://doi.org/10.1007/s12393-011-9034-8

[90] A. El-Hadi, R. Schnabel , E. Straube, G. Müller, S. Henning. Correlation between degree of crystallinity, morphology, glass temperature, mechanical properties and biodegradation of poly (3-hydroxyalkanoate) PHAs and their blends. Polymer testing, 21(6) (2002) 665-674. DOI: https://doi.org/10.1016/S0142-9418(01)00142-8

[91] S. Kashyap, S. K. Pratihar, & S. K. Behera, Strong and ductile graphene oxide reinforced PVA nanocomposites. Journal of Alloys and Compounds, 684 (2016). 254–260.
10.1016/j.jallcom.2016.05.162

[92] S. Vadukumpully, J. Paul, N. Mahanta, & S. Valiyaveettil, (2011). Flexible conductive graphene/poly (vinyl chloride) composite thin films with high mechanical strength and thermal stability. Carbon, 49(1), 198-205. DOI: https://doi.org/10.1016/j.carbon.2010.09.004

[93] M. Farhoodi, S. M. A. Mousavi, R. Sotudeh-Gharebagh, Z. Emam-Djomeh, & A. Oromiehie. Effect of spherical and platelet-like nanoparticles on physical and mechanical properties of polyethylene terephthalate. Journal of Thermoplastic Composite Materials, 27(8) (2014) 1127-1138.
https://doi.org/10.1177/08927057124750

[94] A. M. Clarinval & J. Halleux, Classification of biodegradable polymers. In Biodegradable polymers for industrial applications (2005) 3-31. Woodhead Publishing.

[95] J. Guo, I. Filpponen, L.S. Johansson, S. Heiβler, L. Li, P. Levkin, O. J. Rojas, Micro-patterns on nanocellulose films and paper by photo-induced thiol–yne click coupling: a facile method toward wetting with spatial resolution, Cellulose 25 (2018) 367-375. https://doi.org/10.1007/s10570-017-1593-2

[96] G. Stiubianu, C. Racles, M. Cazacu, B. C. Simionescu, Silicone-modified cellulose. Crosslinking of cellulose acetate with poly [dimethyl (methyl-H) siloxane] by Pt-catalyzed dehydrogenative coupling, Journal of materials science 45 (2010) 4141-4150. https://doi.org/10.1007/s10853-010-4503-7

[97] L. K. Lazzari, V. B. Zampieri, M. Zanini, A. J. Zattera, C. Baldasso, Sorption capacity of hydrophobic cellulose cryogels silanized by two different methods, Cellulose 24 (2017) 3421-3431. https://doi.org/10.1007/s10570-017-1349-z

[98] Z. Zhang, G. Sèbe, D. Rentsch, T. Zimmermann, P. Tingaut, Ultralightweight and flexible silylated nanocellulose sponges for the selective removal of oil from water, Chemistry of materials 26(8) (2014) 2659-2668.

https://doi.org/10.1021/cm5004164

[99] K. Cinar, Evaluation of sandwich panels with composite tube-reinforced foam core under bending and flatwise compression, Journal of Sandwich Structures & Materials 22(2) (2020) 480-493.DOI: https://doi.org/10.1177/109963621879816

[100] X. Quan, M. Zhang, Z. Fang, H. Liu, Q. Shen, Z. Gao, Low oil French fries produced by combined pre-frying and pulsed-spouted microwave vacuum drying method, Food and Bioproducts Processing 99 (2016) 109-115.

[101] Mechanical properties of french fries. https://www.daniellegleason.com/fry-research. (accessed on 28 Oct).

[102] Z. N. Al-Dwairi, K. Y. Tahboub, N. Z. Baba, C. J. Goodacre, A comparison of the flexural and impact strengths and flexural modulus of CAD/CAM and conventional heat-cured polymethyl methacrylate (PMMA), Journal of Prosthodontics 29(4) (2020) 341-349. https://doi.org/10.1111/jopr.12926

4. 7 Supporting Information

Hydrophobization and anti-condensation of cellulose-based films by silanization

Table S4. 1 Water Vapor Barrier Classification [1-3]

Barrier classification	**WVTR (ASTM F1249)**	**Film**	**Application**
low	> 100 g/m^2 day	polyurethane > 492 This work: CMF film ~170 SCMF 1 & 2 film ~ 200	fruits, vegetables
medium	6-100 g/m^2 day	polylactic acid ~ 30 polyethylene terephthalate ~ 32	Baked goods, beverage products
high	1-5 g/m^2 day	polyethylene ~ 5	Drinks

4. 8 References

[1] D. Turan, Water vapor transport properties of polyurethane films for packaging of respiring foods, Food Engineering Reviews 13(1) (2021) 54-65.

[2] V. Holm, G. Mortensen, J. Risbo, Quality changes in semi-hard cheese packaged in a poly (lactic acid) material, Food chemistry 97(3) (2006) 401-410.

[3] N. K. Pramanik, I. Katamgari, A. Dey, Y. K. Bhardwaj, T. Alam, S. K. Chattopadhyay, N. C. Saha, Electron beam irradiation on monolayer plastic packaging films: Studies on physico-mechanical and thermal properties, Packaging Technology and Science 34(8) (2021) 475-483.

Chapter 5

Conclusions and suggestions for future work

5. 1 Conclusions

This thesis has significantly contributed to the science and application of cellulose microfibril films as a sustainable material, particularly for food packaging. It discusses the development of continuous methods of CMF film preparation, the improvement of their material properties, and the overcoming of intrinsic limitations due to their high hydrophilicity. The results of this study complement the scientific state of cellulose-based films with practical solutions that could broadly impact the packaging industry in reducing its reliance on petroleum-based plastics. This is one of the most important global challenges concerning growing problems related to environmental impacts.

Given that cellulose is the most abundant biopolymer on Earth, it provides a fantastic opportunity to substitute traditional materials for synthetic polymers used in packaging with a renewable, biodegradable, and environmentally friendly material. This research demonstrates the possibilities of using CMF films in various packaging application areas, particularly in food packaging, where sustainability and safety are strong determinants. Therefore, the present work underpins a possible larger-scale use of these films in real-life applications by demonstrating how CMF films can be produced with high mechanical strength, good optical properties, and excellent environmental performance.

The other aspect of this study focuses on the exploration of acoustic properties in CMF films, notably regarding how salts and other ions contained in the dope interact with sound speed. Acoustic spectroscopy, which has only recently been applied in this field, provided new insights into the interactions between ions, cellulose, and other constituents of the solution, enabling a deeper characterization of CMF solutions. Traditional methods of characterizing the structure of cellulose X-ray diffraction, scanning electron microscopy, and Fourier-transform infrared spectroscopy have been applied; however, the use of acoustic spectroscopy in the present work yields a special view on the dynamic interactions and molecular properties that are often difficult to grasp from other techniques. Such studies on the acoustic properties are about to tell new stories of structure-property relations of CMF films, particularly concerning the effect of ions in the dope on the behavior of the materials.

Acoustic analysis indicated that cations contribute positively to sound speed, while anions contribute negatively. This effect is related to the hydration layer around the cations, which increases the overall sound speed. We assume that the hydration layer contributes positively to sound speed, as it can be described as ice-like. Given that the sound speed in ice exceeds that in water, it is expected that the hydration layers enhance sound speed in water, thereby positively influencing sound propagation in the solution. In contrast to the behavior of cations, the effects of anions are less pronounced: their interaction with water molecules is less effective due to a thinner hydration layer, resulting in only a modest reduction in sound speed. These findings are crucial for understanding ionic interactions in cellulose solutions and offer new insights into the influence of different ions on the acoustic properties of the material.

This aspect of the research is relevant not only from a scientific perspective but also pragmatically for the industry. An equation correlating sound speed with volume fraction was developed, allowing for the prediction of properties in unknown cellulose solutions. Acoustic spectroscopy will thus become an important tool for further investigating the structure-property relationships in cellulose systems. This work, therefore, lays the foundation for the continued assessment of the physical properties of CMF films, particularly in relation to monitoring their acoustic features. However, calculating the contributions from various cellulose constituents remains complex due to the high charge density in cellulose fibers, which is strongly associated with ions. This issue provides the motivation for developing a new equation that incorporates the effects of charge density and other potential interactions.

In chapter 3 cellulose-based materials, particularly carboxymethylated cellulose fibers (CMF), were explored as sustainable alternatives to traditional petroleum-based plastics. A continuous flow-casting method was developed for the production of cellulose films, offering a flexible and scalable approach for large-scale manufacturing. The film was characterized through various characterization techniques, including X-ray diffraction (XRD), which revealed the anisotropic nature of the films, with crystalline planes aligning preferentially along the direction of the conveyor belt. The mechanical properties of the films, including tensile stress, increased with higher conveyor belt speeds, attributed to better orientation of cellulose crystals and polymer chains in the belt direction. Importantly, the environmental impact of this production method was significantly lower than that of conventional film production processes, as the acid bath could be reused and solvents like isopropyl alcohol and ethanol remained recyclable. This eco-friendly

process presents a viable, renewable alternative to more harmful manufacturing methods such as those used in cellophane production.

However, the inherent hydrophilicity of the CMF films posed significant challenges. Their moisture absorption limits their use in applications where moisture control is essential, particularly in food packaging, where films must act as barriers to water vapor and prevent condensation. To address this, CMF films have been modified through silanization, which enhances their hydrophobicity and anti-condensation properties. However, this chemical modification led to a considerable increase in water vapor permeability, and SEM analysis revealed that the rough surface structure was associated with this change. These structural modifications were aimed at improving the films' suitability for anti-condensation packaging.

To assess their effectiveness, the anti-condensation properties of the films were tested on French fries, and a three-point bending test was conducted. The results showed lower deflection at break and higher force at break, indicating that the films better preserved the crispiness and stiffness of the French fries, suggesting improved breathability and moisture control. Overall, SCMF films demonstrated excellent anti-condensation behavior and could serve as an alternative to conventional plastic films in food packaging for fresh produce due to their ability to handle perishability.

The results also demonstrated that surface properties could be tailored to suit specific applications while retaining essential characteristic. These findings suggest that modified CMF films are expected to meet the requirements of various industries seeking sustainable, high-performance alternatives to synthetic polymers.

5. 2 suggestions for future work

Though these results represent a significant step forward in developing CMF films for food packaging, additional studies are needed to improve the material properties and expand the potential applications of cellulose-based films. Following this, several key areas requiring further research into process optimization, material enhancement, and innovative applications will be highlighted as directions for the future.

5. 2. 1 Acoustic Characterization and Advanced Sensor Integration

The exploration of acoustic properties in CMF films, especially in relation to the speed of sound in the dope, offers a new perspective for characterizing cellulose-based systems. Future research should focus on:

- **Acoustic Characterization and Influence of Other Parameters:** To improve the performance of the cellulose-based material, it is important to better understand how acoustic properties such as particle distribution and elongational viscosity are influenced by the interaction between cellulose fibers, salts, and other additives. Specifically, the distribution of the particles within the film is of fundamental importance to sound propagation. The size, charge density and spatial arrangement of the particles influence acoustic behavior as sound waves propagating through the material may experience reflecting paths determined by such properties. A more charged or structured configuration of the particles within the medium yields different acoustic characteristics, such as increased sound speed and zeta potential.

On the other hand, elongational viscosity—the resistance to deformation under elongation-is another significant acoustic parameter for CMF films. This property relates to how a material would react to applied stress and strain and thus influence sound speed. In a more viscous elongational material, the acoustic wave propagation will be affected differently from the other materials; hence, it can be tailored for specific applications. Knowledge on such influences will therefore impart the ability of scholars to develop CMF films with desired acoustic characteristics, especially for purposes like packaging, sensing, etc.

- **Incorporating Acoustic Sensing into Packaging Applications**: Of course, one of the most attractive directions involves 'smart packaging' development, where CMF films with embedded acoustic sensors can repeatedly measure the internal condition in real-time. Such information about the state of freshness, ripening, or even contamination development in food products could be precious for informing supply chains and product quality management.
- **Modeling Acoustic Properties of Complex Systems**: Based on the acoustic characterization of CMF films, more detailed theoretical modeling of the cellulose-salt-additive complex acoustical properties—related to volume fraction and sound speed—should be developed for further study, taking other effects into consideration. This approach would be particularly useful for characterizing polydisperse systems, allowing for the prediction of film behavior under varying environmental and processing conditions. For example, by analyzing the components in cellulose dope, the mechanical properties of the film generated from the dope can be roughly predicted.
- 5. 2. 2 Optimization of Continuous Production Techniques

While the continuous production method has proven its potential for scalability in the production of cellulose films, it needs optimization for consistency and high-quality output at larger scales. This can be further worked out concerning

- **Enhancing Process Control**: Understanding how the variation of processing parameters such as temperature, air pressure, acid bath concentration, type of acid, humidity, and speed of the conveyor affect the properties of the final film will be critical in facilitating further development of in-process monitoring and automation technologies toward guaranteeing the consistency in quality of films and effectiveness of processes continuously.
- **Uniformity of Feedstock**: Film properties could change with variations in the source of cellulose used as feedstock. Preliminary studies on the influence of different sources, including dissolving and craft pulps, and variations in chemical composition and physical properties on the standardization of the production process can be promising.
- **Scaling Up the Production Process**: Further studies on the potential for scaling up the continuous production method are required. It will be essential to determine the parameters—such as production rate, film thickness, film porosity, and drying times—at which process optimization occurs when scaled up to an industrial level. This knowledge is crucial for the commercialization of CMF films.

5. 2. 3 Improvement of Film Properties through Surface and Chemical Modifications

The most challenging obstacles for replacing traditional packaging with cellulose-based films are related to moisture sensitivity, scale-up cost and relatively weak mechanical properties. The industries and customers would prefer cellulose-based films over petrol-

based films if the above problems can be effectively addressed. Although the silanization treatment reported in this study greatly enhanced the hydrophobicity and moisture resistance of CMF films, this study proved that their barrier properties and mechanical strength could further be optimized by searching for additional surface modification techniques:

- **Exploration of Surface Treatments**: Silanization of CMF films produced with a higher conveyor belt speed could be a potential way to optimize the tensile strength of the film, as the films show better strength when regenerated under a faster conveyor belt speed. Other surface modification methods, such as coating with hydrophobic polymers or nanoparticles, could further enhance the moisture barrier properties. In fact, adding other green biopolymer materials like polylactic acid could improve moisture resistance due to their excellent moisture-resistant properties.
- **Nanoparticle Incorporation**: CMF films could also be studied through the incorporation of graphene oxide, or zinc oxide to enhance their mechanical strength, barrier properties, and hydrophobicity. Special care must be taken regarding the interactions of such nanoparticles with the cellulose matrix to ensure optimum performance without sacrificing the films' transparency or flexibility.
- **Green Chemistry Approaches**: To further enhance the sustainability of cellulose-based films, it is crucial to prioritize research into environmentally friendly surface modification methods. While the solvent currently used, isopropyl alcohol (IPA), is not fully environmentally friendly, we need to actively explore alternative, more sustainable solvents. Performing the carboxymethylation reaction during grinding through

mechanochemistry, without the use of solvents, offers an alternative approach for green production.

5. 2. 3 Investigating the Impact of Film Composition on Functionality

The composition of CMF films is one of the key factors determining their performance. Further research should investigate how different additives, such as plasticizers, crosslinkers, stabilizers, and salts, impact the properties of the films:

- **Role of Plasticizers in Flexibility and Strength**: Plasticizers are known to enhance the flexibility of films, making them more suitable for packaging applications where film stretching or flexibility is required. Understanding how different plasticizers influence the mechanical properties and film stability will help in tailoring the strength of CMF films for specific uses.
- **Crosslinkers and stabilizers:** The crosslinkers form covalent bonds between the cellulose chains, thus increasing the CMF film's strength and resistance due to a more developed network structure. This enhances mechanical and thermal properties. Common crosslinkers like glutaraldehyde or epichlorohydrin can also improve barrier properties by reducing gas and moisture permeation. Stabilizers help maintain the integrity of the films under varying environmental conditions. For instance, UV stabilizers protect the films from sunlight-induced degradation, while moisture stabilizers, such as glycerol, make the films less absorbent and swell resistant. These additives stabilize the films to make their performance more consistent over time, hence improving their suitability for more varied applications.

- **Salt and Additive Interactions**: Salts within the CMF dope influence not only the film's mechanical and moisture properties but also its acoustic properties. Further work needs to be done on the influence of the types and concentration of salts on the structural integrity of the films, the sound speed, elongational viscosity, sizing, attenuation, and general properties under varying environmental conditions.

5. 2. 4 Applications in Packaging and Beyond

CMF films have excellent potential in the food packaging industry, but their applications could extend well beyond food packaging. Future work will focus on the broad application possibilities of CMF films:

- **Longer Shelf-Life for Diverse Products**: Although CMF films have been suggested for packaging fresh produce, they can also be explored for other food types, such as dairy, meat, or baked products. The assessment of the subsequent shelf life and quality of diverse products packed in CMF films stands to be a significant step in investigations.
- **Sustainability in the Packaging Sector**: With much of the world striving to find sustainable packaging alternatives, CMF films present a potential solution to reduce plastic waste. There is an urgent need for a life cycle assessment (LCA) of these films and compare the results with LCA's of standard plastic films to identify and quantify any benefits related to sustainability and eco-friendliness. Extending the life cycle and maintaining the properties during storage should be a primary focus. For instance, combining cellulose with other materials could help extend shelf life while preserving its performance.